Design of radio-frequency cavities and Tera-Hertz electron injectors for advanced applications

Dissertation zur Erlangung des Doktorgrades
an der Fakultät für Mathematik, Informatik und
Naturwissenschaften
Fachbereich Physik
der Universität Hamburg

Vorgelegt von

Seyedmoein Seyedfakhari

aus Rasht, Iran

Hamburg
2016

Tag der Disputation: 22.03.2016
Folgende Gutachter empfehlen die Annahme der Dissertation:
Prof. Dr. J. Roßbach
Prof. Dr. F. X. Kärtner

to my Love,

Faeze

and

my World,

Elena

Abstract

Design of three accelerator components including a buncher cavity for REGAE, a normal conducting cavity for arrival time stabilization at FLASH and ultra-fast guns for the AXSIS project is presented in this thesis. Using RF cavities caused a revolution in accelerators and made it possible to generate high energy particle beams. In advanced accelerators, cavities are not only used to increase the particle energy but they are also widely used to improve the beam quality and additionally for beam diagnostic purposes. In the present dissertation, such applications are discussed. First, design of a buncher cavity which compresses the bunch at the REGAE facility is presented. The design pursues improving the mode separation of the cavity. The simulation result illustrates that the difference between the operating mode and its adjacent mode has been increased from 2 MHz for the existing cavity to 9.5 MHz for the new design. In the second part, a normal conducting cavity is discussed, which will be used to regulate the arrival time of the bunches at FLASH and at the European XFEL. The designed cavity is able to correct the arrival time jitter of ± 150 fs in order to provide femtosecond precision synchronization between the electron beam and the external laser pulses. Thermal, wakefield and multipacting simulations have also been performed for the designed cavity in order to evaluate its operation efficiency. In advanced accelerators however RF cavities should be replaced by novel structures to accelerate the particles in shorter distances using higher operating frequency. To this end, ultra-fast guns are designed which will be discussed in the last part of this work. The designed guns accelerate the electrons from their rest mass up to 2 MeV using a single cycle THz signal with a total energy of 2 mJ.

hi

Zusammenfassung

In dieser Arbeit werden drei Beschleunigerkomponenten untersucht.Zum einen eine Buncher Kavität bei REGAE, des Weiteren eine normalleitende Kavität zur Ankunftszeitstabilisierung bei FLASH, sowie ultra-schnelle Beschleunigungsstrukturen beim AXSIS Projekt. Die Nutzung von HF Kavitäten revolutionierte Beschleuniger und machte die Generierung hochenergetischer Teilchenstrahlung möglich. Modernen Beschleunigerkavitäten werden sowohl zur Erhöhung der Strahlenergie als auch zur Verbesserung der Strahlqualität und der Strahldiagnostik genutzt. Diese Anwendungen werden im weiteren Teil der Dissertation diskutiert. Das Design der Buncher Kavität welche den Elektronenstrahl bei REGAE komprimiert wir im ersten Teil beschrieben. Die Differenz der Betriebsfrequenz und des ersten zusätzlichen Resonanzfrequenz der Kavität, 2 MHz im vorliegenden Design, wurde auf 9 MHz wesentlich verbessert. Im zweiten Teil dieser Arbeit wird eine normalleitende Kavität zur Regelung der Ankunftszeit bei FLASH als auch beim Europäischen XFEL entworfen. Diese kann Ankunftszeitschwankungen im Bereich von ±150 fs ausgleichen um eine femto-sekunden genaue Stabilität zwischen den FEL Pulsen und des externen Lasers bei Pump-Probe Experimenten zu gewährleisten. Um den optimalen Betrieb im Beschleuniger zu gewährleisten werden Simulationen hinsichtlich der thermischen Eigenschaften, Wakefeldern sowie des so genannten Multipacting untersucht. Um Teilchen in kleineren Entfernungen mittels höherer Frequenzen zu beschleunigen sollten in modernen Beschleunigern Kavitäten durch neuere Strukturen ersetzt werden. Dies wird im letzten Teil dieser Arbeit anhand von ultra-schnellen Beschleunigungsstrukturen diskutiert. Die entwickelte Struktur kann Elektronen von dessen Ruheenergie auf bis zu 2 MeV mittels eines einzelnen THz Zykluses mit einer Gesamtenergie von 2 mJ beschleunigen.

hi

Acknowledgements

I wish to express my thanks to those who have contributed to this thesis and supported me in one way or the other during this amazing journey. First, my special thanks to my advisors Prof. Jörg Roßbach and Dr. Holger Schlarb. I would like to thank you for encouraging my research and for allowing me to grow as a research scientist.

profound gratitude goes to Dr. Klaus Flöttmann, who has been a truly dedicated mentor. I am particularly indebted to Klaus for his guidance and all the useful discussions and brainstorming sessions. His deep insights helped me at various stages of my research. I would like to thank specially Dr. Sven Pfeiffer for his valuable guidance, scholarly inputs and consistent encouragement I received throughout the research work. I also thank Dr. Hossein Delsim-Hashemi, Dr. Arya Fallahi, Dr. Dirk Lipka, Dr. Martin Dohlus, Dr. Markus Hüning and Dr. Alireza Yahaghi for their helps and useful discussions. I would like to thank my dissertation referee Prof. Franz Kärtner and the disputation committee members Prof. Henry Chapman and Prof. Daniela Pfannkuche.

Last but not least, my sincere appreciation to my wife Faeze, whose presence, love and supports enabled me to overcome the difficulties during my PhD in a foreign country. I really owe her and our little angle Elena.

Contents

List of Figures

List of Tables

Chapter 1

Introduction

Accelerators are devices to accelerate particles from their rest mass to relativistic velocities. These devices are the main structures forming particle beams based on the interaction of the charged particles and electromagnetic fields. There are several types and generations of accelerators which were developed during the last 80 years. The accelerator types include cyclotrons, synchrotrons, betatrons, storage rings and linear accelerators. Each of them has its own characteristics and range of application [1, 2].

Huge accelerators are widely used in high energy physics to explore the inside of matter in order to study the constituents of atoms [3]. As an example, colliders are mostly used where high energy particles scatter off a target or off another high energy beam [4]. Well-known colliders, which are still in operation, are the Large Hadron Collider (LHC) at CERN and the Relativistic Heavy Ion Collider (RHIC) at Brookhaven National Laboratory [5, 6]. HERA, PETRA and DORIS are examples of accelerators at DESY that have worked as collider in the past, but are no more in operation as a collider [7, 8, 9]. Accelerators can also be used to inject particles into emission section of advanced light sources such as synchrotron radiation sources and Free Electron Lasers (FEL) [10]. The first worldwide soft X-ray FEL based on the self-amplified spontaneous emission (SASE) process named FLASH (Free-electron LASer at Hamburg) started lasing in the year 2000 at DESY [11, 12]. Since then it has been upgraded several times and is now able to provide ultra-short femtosecond laser pulses in a wide wavelength range from the EUV to soft-X ray. The European XFEL presently under construction in Hamburg will provide laser pulses with even better quality and shorter wavelength in the close future [13]. In addition to the large accelerators, the smaller ones which provide particle beams with lower energy are being used for several applications such as particle therapy for the treatment of cancer, ion implantation or industrial uses [14, 15].

The first accelerators were built in the 1930s in which the particles gained energy from a high static electric field [2]. Of course, it was not possible for the particles to reach very high energies just from the static fields. Using the RF cavities made a revolution in accelerators and afterwards it was possible to produce very high energy particles [16]. During the past decades, extensive efforts were devoted to optimize the design of different parts of the accelerators [17, 18, 19]. For instance, superconducting cavities to accelerate particles were optimized to achieve the highest quality factor and the highest shunt impedance. In this domain, scientists are looking for the material and also the structures that can increase the quality factor of the cavities [20].

In advanced accelerators, RF cavities are not only responsible for increasing the particle energy, but they are also widely used to improve the beam quality and additionally for beam diagnostics [21, 22]. It is possible to compress the electron bunches using a buncher cavity based on the zero crossing effect. The electrons in the head of the bunch gain less energy than the electrons in the tail of the bunch which causes the bunch length to decrease as the particles travel through the beam pipe [23]. Such application is described in the second chapter where we discuss the design of a new buncher cavity for REGAE (the Relativistic Electron Gun for Atomic Exploration). In the existing buncher in the REGAE facility, the operating mode is too close to its adjacent mode and the input signal excites the non operating mode partially which causes unwanted effects and decreases the machine efficiency. Therefore, the designed cavity has to have a required mode separation in order to improve the operation of REGAE. In such cavities, the quality factor might not have as much importance as for those cavities which are used to accelerate particles.

In some cases, we deliberately decrease the quality factor of the cavities. In the third chapter we discuss one of these cases, which is designing of a normal conducting cavity to stabilize the arrival time of the bunches in FLASH and also in the European XFEL. The idea is to measure the arrival time of one bunch and apply a correction accelerating or decelerating voltage to the next bunches. Since a fast actuator should provide the correction voltage it was required to design a cavity with a high bandwidth which means a cavity with lower quality factor. In this chapter, the design of the cavity itself as well as its input coupler are discussed. Based on the existing limitations, the optimum coupling from side using a loop has been designed. RF cavities are actually electromagnetic resonators which can be modeled by electric circuits. The electric circuit model provides a proper approach to assess cavities. We developed circuit models for the designed cavities, which ease the finding of the best situation for the cavity operation. One of the important issues in using the cavities is tuning them after installation in the main beam pipe. Using the proposed circuit model, one can find a guideline that is useful during the tuning of the cavities.

To achieve higher energies of the particles in accelerators, one should increase the length of the accelerating part which rises the building and maintenance costs. Another possible solution is to decrease the wavelength of the electromagnetic field by increasing the operating frequency because this may lead to stronger accelerating fields [24]. However, the electrical breakdown of metals puts an upper limit to the accelerating gradient which can be provided by metal cavities [25]. It is therefore of high importance to engage novel accelerating methods and structures that need less size and expenses which can accelerate the particles in higher frequency fields. In the fourth chapter a novel structure to transfer the energy from a THz signal to the electrons is introduced. This structure is going to be used as an ultra-fast gun in the AXSIS project(Attosecond X-ray Science: Imaging and Spectroscopy).

Chapter 2

Design of a new buncher cavity for REGAE

REGAE (the **R**elativistic **E**lectron **G**un for **A**tomic **E**xploration) is a small electron accelerator built and operated within the framework of the Center for Free-Electron Laser Science CFEL at the DESY in order to provide high quality electron bunches for time resolved diffraction experiments [26].
The RF system of REGAE contains different parts such as low level RF, preamplifier, modulator, phase shifter, and cavities. A photo cathode RF gun operating at 3 GHz (S-Band) is used for the production of electrons. The $1\frac{1}{2}$ cell gun cavity accelerates the electrons to energies of up to 5 MeV. A buncher cavity is used to compress the electron bunches by passing the electrons at the zero crossing of the field and so introducing a correlated energy spread. In the following drift section the bunch length decreases due to the different velocities and reaches a minimum about 4 m downstream of the bunching cavity where the target chamber is located [26, 27].
The present chapter concerns the design of a new buncher cavity for REGAE. In the first section the motivations for replacing the existing buncher cavity with a new one and the main problems of the existing cavity are described. The next section is devoted to the procedure of designing the buncher. In this section several simulations are performed in order to find out the effects of the buncher parameters and to find the optimum values for these parameters. To get a better understanding about the role of different parts of the buncher a circuit model is developed in the third section. Finally in the last section of this chapter some beam dynamics simulations are performed in order to investigate the effects of the fundamental modes of the buncher on the beam and its characteristics such as bunch length and the beam emittance in both the existing buncher and for the new design.

2.1 Motivations for new design

An isometric view of the REGAE buncher cavity is displayed in Figure 2.1 while Figure 2.2 shows the cross sectional view of this cavity [27]. This cavity is a standing wave structure which means it has to be connected to an input coupler which will be explained in more details in section 2.2.4 (see figure 2.17). As it can be seen in these figures, the REGAE buncher is formed from four coupled pillbox cavities and so it has four fundamental transverse magnetic TM_{010} normal modes [1] which are named as 0-mode, $\frac{\pi}{3}$-mode, $2\pi/3$-mode, and π-mode. These names are based on the phase shifts between adjacent cells [28].

The measurement [29] and simulation results for the frequencies of these four

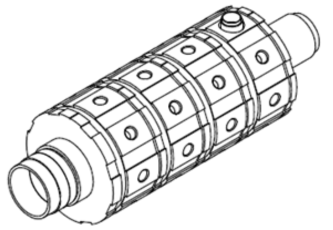

Figure 2.1: Isometric view of the REGAE buncher cavity

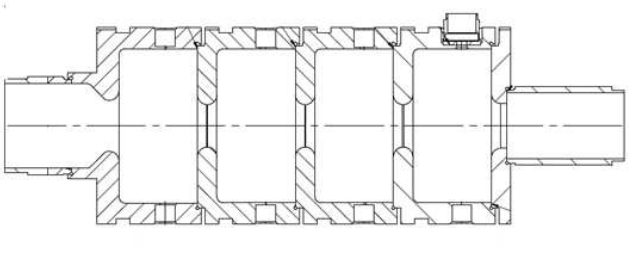

Figure 2.2: Cross sectional view of the REGAE buncher cavity

TM_{010} normal modes are shown in Table 2.1. The simulations are performed using two software programs, CST Microwave Studio which is a 3D electromagnetic simulation software [30], and SUPERFISH that can simulate electromagnetic components with axial symmetry since it is a 2D program [31].

According to this table the difference between the π-mode which is the operating mode and its adjacent mode, $2\pi/3$-mode, is very small and only 2 MHz. This very close mode might lead to some functional problems during operation of REGAE.

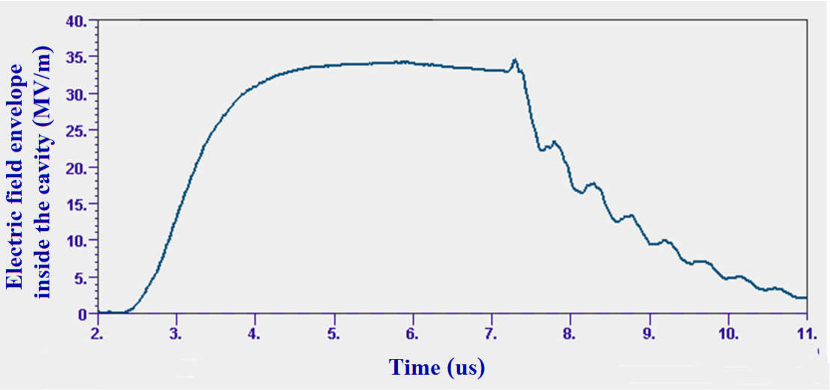

Figure 2.3: The RF power amplitude in the REGAE buncher

Table 2.1: Measured and simulated frequencies of the buncher modes

	0-Mode Frequency (MHz)	$\frac{\pi}{3}$-mode Frequency (MHz)	$\frac{2\pi}{3}$-mode Frequency (MHz)	π-mode Frequency (MHz)
Microwave Studio	2983	2988	2993	2995
SUPERFISH	2984.2	2989.4	2994.6	2996.8
Measurement	2985	2991	2996	2998

For example Figure 2.3 shows the amplitude of the RF power in the buncher in which some fluctuations are added to the main signal [27]. The frequency of these fluctuations is exactly equal to the difference between π-mode and $2\pi/3$-mode and the origin of this parasitic signal is the poor mode separation in the buncher [29]. In fact the input power excites the other normal modes of the buncher in addition to the π-mode. Such fluctuations might cause unwanted effects on the beam which is going to be bunched. As mentioned, bunching is fulfilled by introducing a stronger electric field to the electrons which are located in the tail of the bunch. So the bunching process efficiency is strongly dependent on the phase of the operating mode of the buncher and in fact one should find the phase difference between gun and buncher for maximum bunching. But excitation of the other normal modes of the buncher can cause small changes in the bunching phase which may lead to deviations of the minimum achievable bunch length on the target position since the electric field inside the cavity in this case is a superposition of the π-mode and its adjacent mode. So the main goal in designing the new buncher is to improve the mode separation in order to remove or at least reduce the effects of other modes on the buncher operation as much as possible.

2.2 Design process and simulation results

In order to improve the mode separation in the buncher one should increase the coupling between adjacent cells [1]. Cell to cell coupling is strongly dependent on the geometry of the cavities such as radius and thickness of the disk between them. It is therefore possible to achieve a better mode separation by changing the physical parameters of the buncher. The parameters that have been changed in order to increase the difference between the fundamental modes of the buncher are depicted in Figure 2.4. In this figure rA, rB, and rC are representing the radius of the cross sectional curve between adjacent cells. This curve is a 180 degree semi circle and so theses parameters determine the distance between neighboring cells and in fact the thicknesses of the disks between the cells while yA, yB, and yC represent the radii of these disks openings. Furthermore yD, rD and yE, rE determine the corresponding parameters related to the input and output cells respectively. These parameters in the existing buncher are as follows:

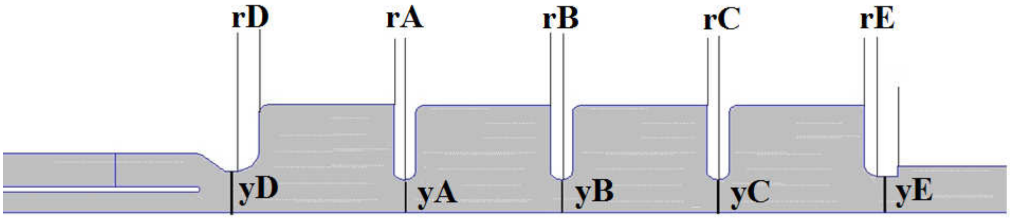

Figure 2.4: The physical parameters of the buncher

rA= rB= rC= 4.75 mm
yA= yB= yC= 10.8 mm

rD= 4.75 mm
yD= 13 mm

rE= 4.75 mm
yE= 11.4 mm

2.2.1 Investigation of the effects of physical parameters on the mode seperation

To find the effects of each parameter, it is varied between reasonable end values while the other parameters are kept constant. After simulation and finding the frequencies of the buncher normal modes, the dependency curves of these frequencies on the buncher parameters are drawn. Such curves are displayed in Figure 2.5 to Figure 2.12. In these figures the effects of the parameters shown in Figure 2.4 on the difference of the operating mode and the other normal modes, (delF1, delF2, and delF3) and also their influence on the absolute value of the π-mode

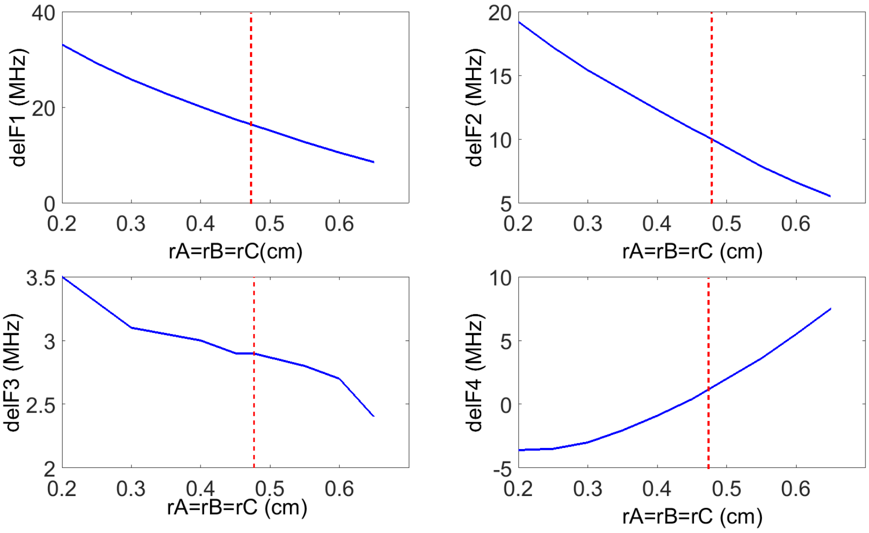

Figure 2.5: SUPERFISH simulation results: delFs versus rA,rB,rC

(delF4) are investigated.

$$\begin{aligned}
\text{delF1} = \pi\text{-mode} \quad &- \quad 0\text{-mode},\\
\text{delF2} = \pi\text{-mode} \quad &- \quad \tfrac{\pi}{3}\text{-mode},\\
\text{delF3} = \pi\text{-mode} \quad &- \quad \tfrac{2\pi}{3}\text{-mode},\\
\text{delF4} = \pi\text{-mode} \quad &- \quad 2998\text{MHz} \quad .
\end{aligned}$$

The working point of the existing buncher is shown with the red dashed line in these curves. Note that in Figure 2.5, rA, rB, and rC are equal for all the cases, in fact the thicknesses of the disks are kept equal in these curves while in Figure 2.11 and Figure 2.12 only the effect of one disk thickness is investigated.

2.2.2 First optimization

As a summary of these curves one can conclude that in order to improve the mode separation the radii of the disks between cavities should be increased and despite of their radii the thickness of the disks should be decreased. These results was of course expected as we know that increasing the radius of a disk opening or decreasing its thickness will fortify the coupling between the cells which are located at the sides of the disk. So considering the mentioned results the amounts for the parameters were chosen as the first attempt which are listed in Table 2.2.

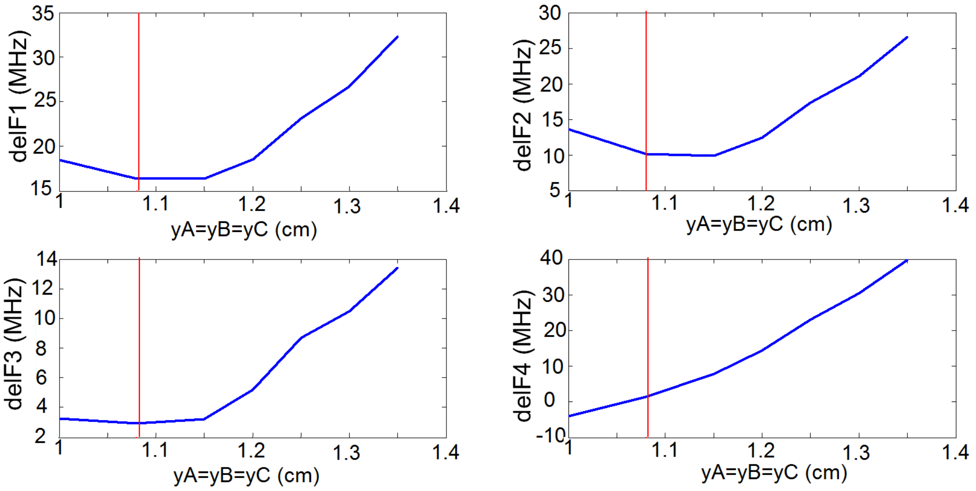

Figure 2.6: SUPERFISH simulation results: delFs versus yA,yB,yC

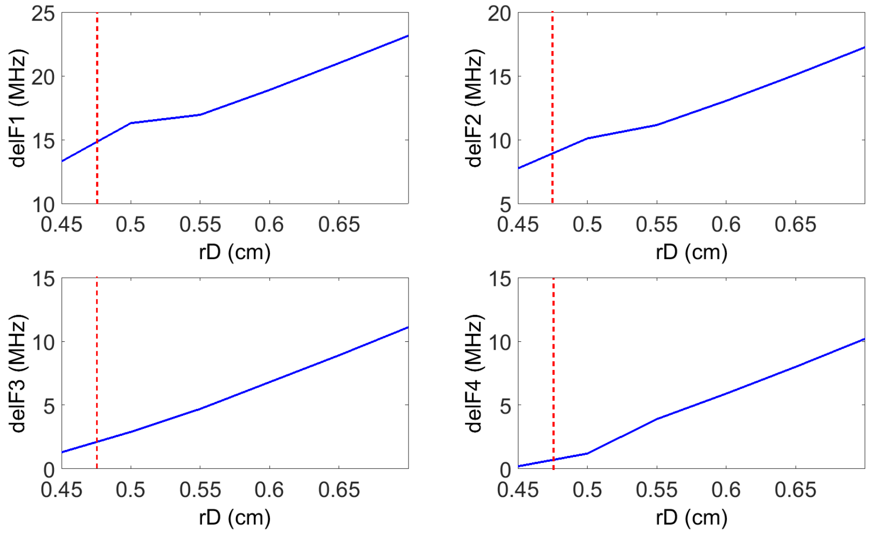

Figure 2.7: SUPERFISH simulation results: delFs versus rD

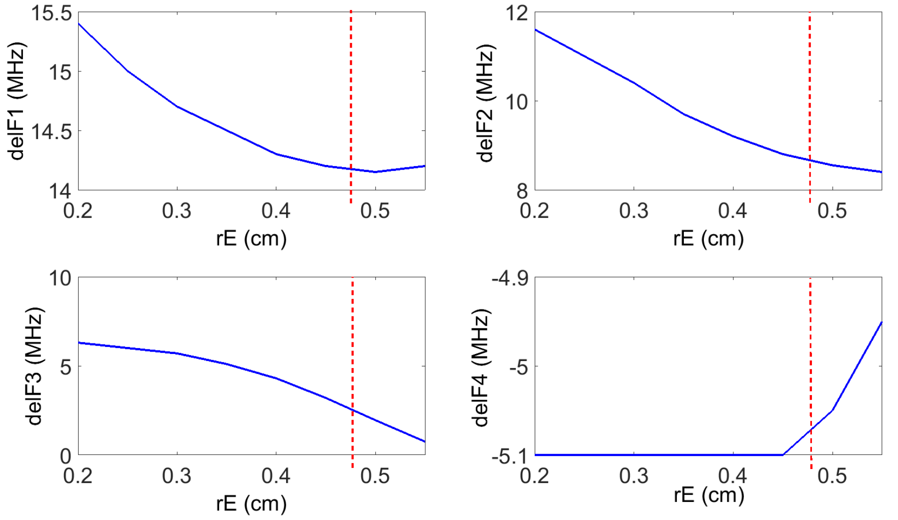

Figure 2.8: SUPERFISH simulation results: delFs versus rE

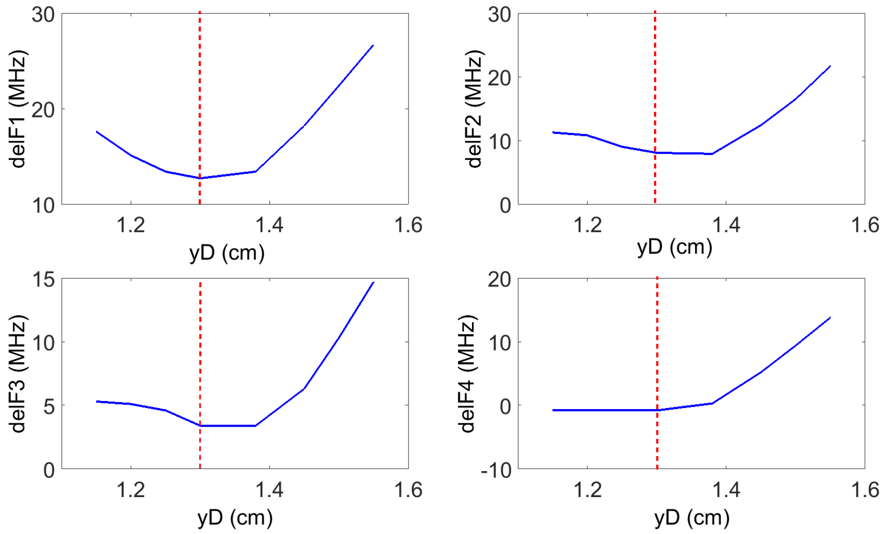

Figure 2.9: SUPERFISH simulation results: delFs versus yD

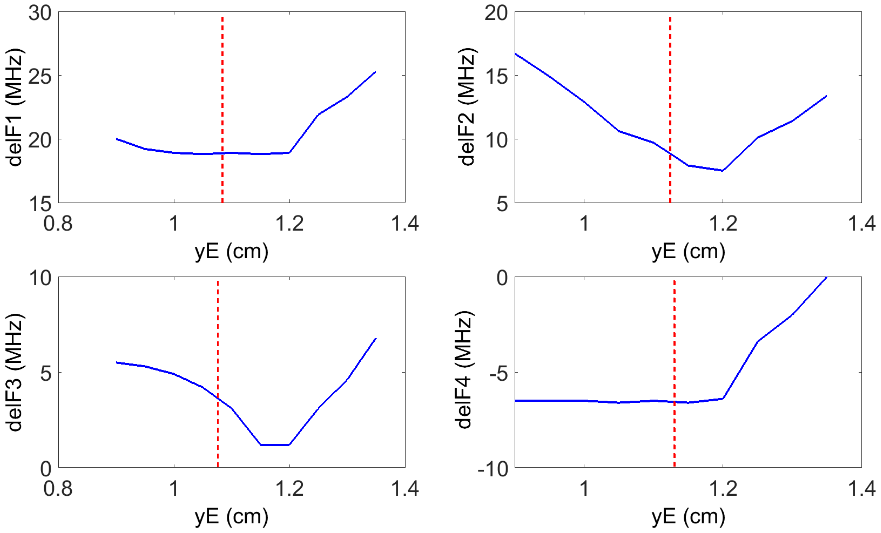

Figure 2.10: SUPERFISH simulation results: delFs versus yE

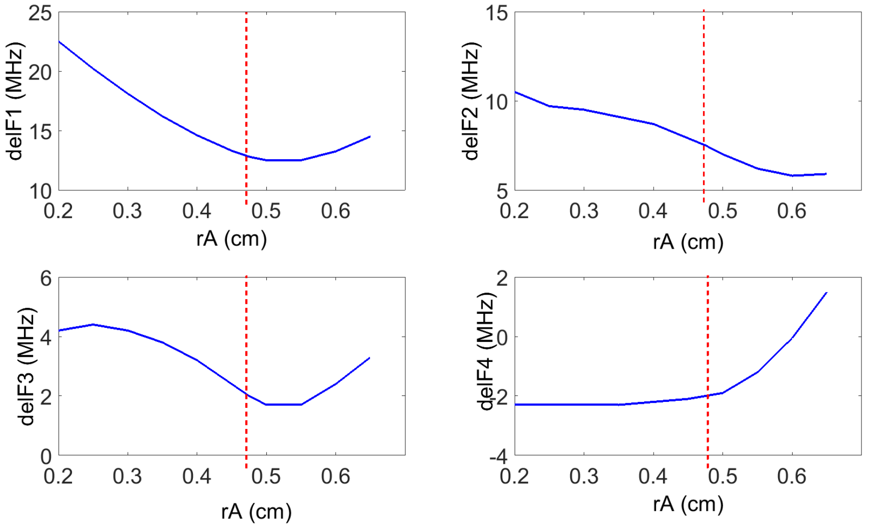

Figure 2.11: SUPERFISH simulation results: delFs versus rA

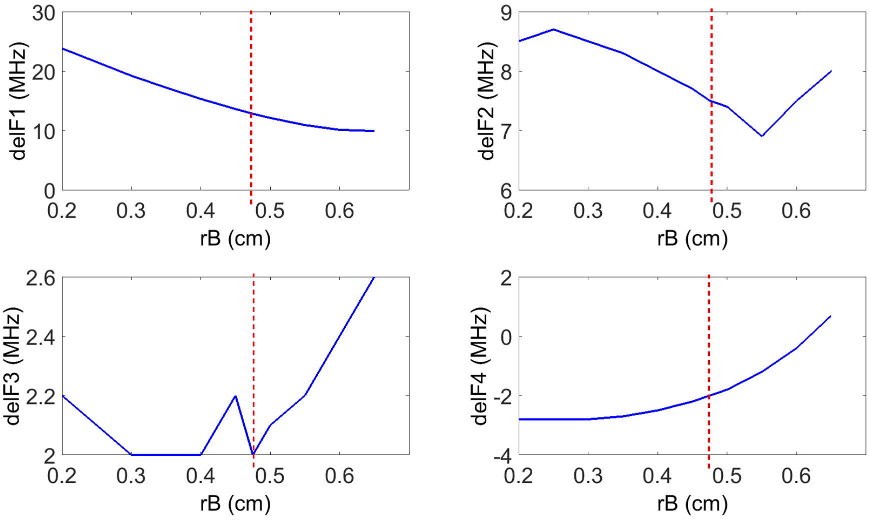

Figure 2.12: SUPERFISH simulation results: delFs versus rB

Table 2.2: The first chosen values for the cavity parameters

Parameter	**Value (mm)**		**Parameter**	**Value (mm)**
rA	2		rB	2
rC	2		rD	7
rE	2		yA	14
yB	14		yC	14
yD	15.5		yE	9

Based on these values the frequencies of the buncher normal modes were calculated as Table 2.3.

From the above table the differences between the adjacent modes have been increased in comparison with their amounts in the existing cavity:

$$\begin{aligned}
\text{delF1} = \pi\text{-mode} &\quad - \quad 0\text{-mode} &&= 76\text{MHz},\\
\text{delF2} = \pi\text{-mode} &\quad - \quad \tfrac{\pi}{3}\text{-mode} &&= 55\text{MHz},\\
\text{delF3} = \pi\text{-mode} &\quad - \quad \tfrac{2\pi}{3}\text{-mode} &&= 19\text{MHz} \quad .
\end{aligned}$$

At the first look it seems promising that the difference between the operating mode and its adjacent mode is increased up to 21 MHz, however some other limitations must be considered. First, according to the whole system design the absolute value of the operating frequency should be 2998 MHz, while by the above values it is 3048 MHz and so it is necessary to shift it back to its operating point.

Table 2.3: SUPERFISH results for the buncher frequencies with the new dimensions

	0-Mode Frequency (MHz)	**$\frac{\pi}{3}$-mode Frequency (MHz)**	**$\frac{2\pi}{3}$-mode Frequency (MHz)**	**π-mode Frequency (MHz)**
new design	**2972**	**2991**	**3027**	**3048**
old design	**2984**	**2989**	**2995**	**2997**

The other limitation is about the maximum amount of the electric field inside the cells. In Figure 2.13 the amplitude of the electric field on the axis of the buncher in steady state is shown (ρ=0 in cylindrical coordinates). The amplitudes of the electric field for the TM_{010} modes has its maximum value on the axis and by increasing the radius it will decrease [32]. It should be noted that this electric field distribution is for the buncher with parameters that are shown in Table 2.2 and it is also assumed that the total stored energy inside the cavity is 1 Joule (which is the default setting of SUPERFISH).

As it is displayed in this figure the amount of the peak of the electric field decreases from the first to the last cell which is not desirable. The more reliable situation is that there exists a flat profile of the electric field peaks. In other words the maximum of the electric field inside the cells should be equal in order to achieve the best efficiency of the buncher. There are several reasons that we are more interested in a flat top electric field inside the cavities. If the cavity is going to be used to increase the energy of the particle the energy gain can be increased by increasing the accelerating gradient. Even in our case which is a buncher cavity by increasing the electric field inside the cavity, the minimum bunch length occurs in shorter distance, thus the overall length of the machine is decreased. The electrical breakdown of metals puts a threshold on the accelerating field that can be provided by the cavities. Therefore many cavities are set to operate with the fields near their breakdown limit. Lets consider again the electric field pattern that is shown in Figure 2.13. Here the electric field in the first cell is more than the other cells. This means the breakdown will occur in this cell first, as one increases the input power while the other cells are still below the limit. Because of the first cell's breakdown limit, the maximum efficiency of the other cells cannot be provided. By making a flat-top on-axis peak electric field, it would be possible for all cells to operate close to their breakdown limit. On the other hand the temperature change will be homogeneous in the case of a flat-top on-axis peak electric field. Since the dissipated power in the cavity walls is proportional to the square of the electric field on the walls one expects a higher shunt impedence when the electric field inside the cells has a smooth distribution.

Hence, it is required to find a way to solve the two mentioned problems at once.

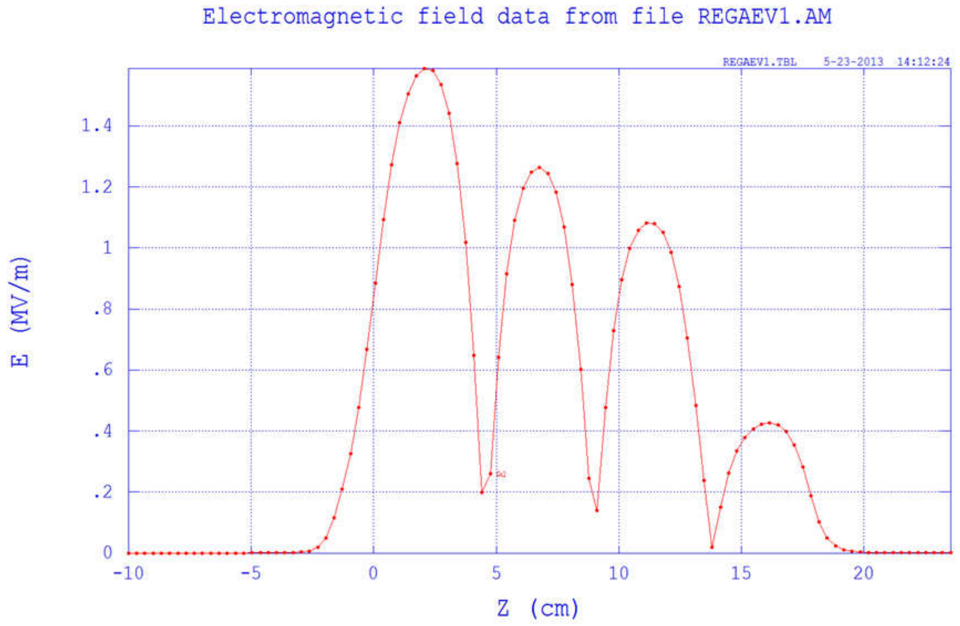

Figure 2.13: The electric field on the axis of the buncher for the π-mode assuming 1 J total stored energy

It is known that the resonant frequency and also the amplitude of the electric field inside a cavity are dependent on its volume [32]. It is therefore possible to shift the π-mode frequency back to its operating point and simultaneously make the peak of the electric field profile flat by adjusting the cell's volume. Parameters that have been changed in order to achieve this goal are the radii of the cavities which are shown in Figure 2.14. These parameters are named as hA, hB, hC, and hD and in the existing cavity are as follow:

hA=39.38 mm hB=39.24 mm hC=39.24 mm hD=39.24 mm

Decreasing one cell diameter results in two phenomena. First, an increase of the π-mode frequency and second, an increase of the electric field of the corresponding cell. Considering these changes a guideline could be extracted to find the appropriate amounts for the radii of the cells. For example according to Table 2.3 in order to shift the π-mode frequency to its operating value the cells diameter should be increased, however Figure 2.13 says that the diameter change in the first cell should be more than the others. Finally the following amounts are obtained for the cells radii:

hA=40.01 mm hB=39.88 mm hC=39.86 mm hD=39.31 mm

And the simulation results based on these values are shown in Table 2.4.

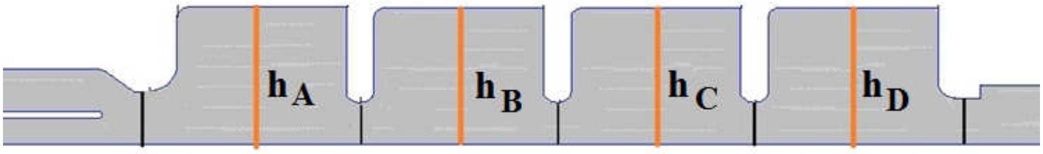

Figure 2.14: The cell's radii are considered as an effective parameter in the RF design

Table 2.4: SUPERFISH results for the buncher frequencies considering the new cell radii

0-Mode Frequency (MHz)	$\frac{\pi}{3}$**-mode Frequency (MHz)**	$\frac{2\pi}{3}$**-mode Frequency (MHz)**	π**-mode Frequency (MHz)**
2926.3	**2954.8**	**2984.3**	**2998**

For this table the differences between the operating mode and the other modes are as below:

$$\begin{aligned} \text{delF1} &= \pi\text{-mode} &-& \quad 0\text{-mode} &= 71.7\text{ MHz},\\ \text{delF2} &= \pi\text{-mode} &-& \quad \tfrac{\pi}{3}\text{-mode} &= 43.2\text{ MHz},\\ \text{delF3} &= \pi\text{-mode} &-& \quad \tfrac{2\pi}{3}\text{-mode} &= 13.7\text{ MHz}. \end{aligned}$$

Manufacturing tolerance is another issue that should be considered during the design process. The manufacturing tolerances of different parts of the cavity are shown for example in Figure 2.15.

According to these tolerances it is necessary to consider some errors in designing the buncher. For instance for the cell diameter it is tolerable to have a maximum of 10 μm error. These tolerances are selected based on the maximum value of the frequency deviation that can be compensated by tuning. This value for a normal conducting cavity working in the frequency range in which the REGAE buncher operates would be about 2 MHz [33]. As discussed before the maximum value of the electric field in the cavities is strongly dependent on the cavity diameter. Hence notwithstanding the designed values for a flat electric field pattern, it is inevitable to have a difference between the maximums of the electric field inside the cavities in the real world. The worst situation would be the situation that the manufacturing errors are equal to their maximum allowed value and in the opposite direction for different cells. In this situation the electric field of two cells increases while it decrease in the other cells leads to the maximum deviation from

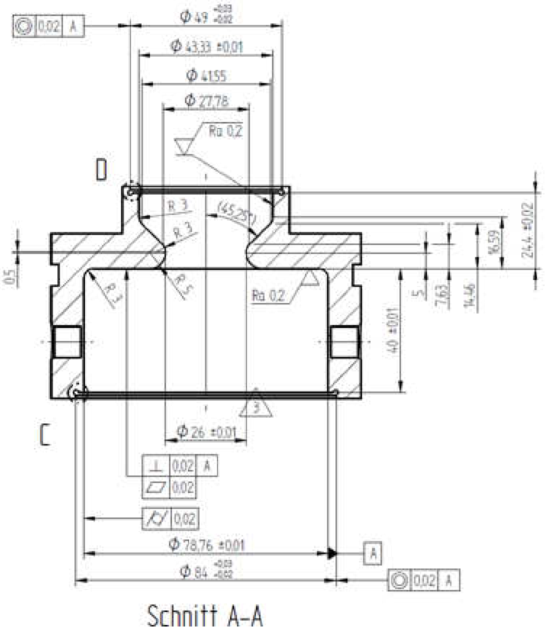

Figure 2.15: The tolerances of manufacturing a cavity cell

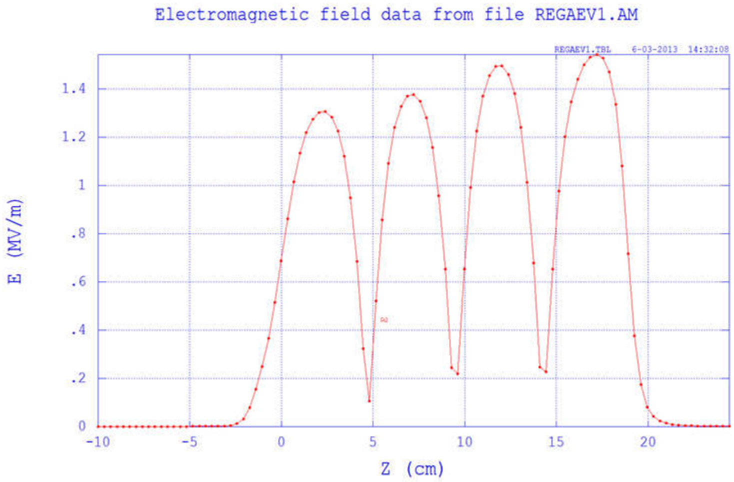

Figure 2.16: Electric fields of the cavities in the worst situation of manufacturing errors

the desired flat pattern. Such situation is shown in Figure 2.16.

2.2.3 Final optimization

An idea has been proposed in order to remove the undesired effects of the adjacent modes of the buncher and the gun simultaneously. Based on this idea the effects of the nearest modes to the operating modes of the buncher and the gun (0-mode of the gun and $2\pi/3$-mode of the buncher) can be compensated using a feed forward and a feedback loop . To exploit such idea the designed buncher should satisfy some conditions. First, because only one control system is going to be used to compensate the effects of adjacent modes of the gun and the buncher, the difference between π-mode, the operating mode and its nearest mode, $2\pi/3$-mode should be equal to the difference between two fundamental modes of the REGAE gun . This value for the gun is 9.5 MHz. Second, the difference between 0-mode and π-mode in the buncher should be more than half of the sampling frequency of the control system which is 125 MHz or as close to this value as possible. So in the designed cavity the difference between two farthest normal modes should be more than 62.5 MHz or as near to this amount as possible. In other words the two desired conditions could be summarized as:

1) delF3 $=$ 9.5MHz,
2) delF1 $\approx$ 62.5MHz .

Comparing the above condition with the results that are depicted in Table 2.4, the difference between modes should be decreased. According to the table for this design delF3 is 13.7 MHz and delF1 is 71.7 MHz. So it is required that delF3 decreases by $\sim$ 4 MHz while delF1 decreases by $\sim$ 9MHz which means that the difference between $2\pi/3$-mode and 0-mode should decrease by $\sim$ 5MHz. It seems to be difficult to achieve these values since the relative variation of delF3 is much more than the variations of the difference between the other normal modes (30% vs. 8%). Hence, parameters need to be found that change the difference between two normal modes while the differences between the other modes are not changed significantly. According to the simulation results the best solution to this problem is to remove the symmetry of the buncher by making the disks thicknesses different. The obtained values for the parameters of the buncher which can satisfy the above conditions are summarized in Table 2.5. The selected values are not the unique solution that satisfy the required conditions. Since there are a lot of parameters that can be played with to achieve the required conditions one can expect that there should be more than one solution. However the selected solution includes reasonable values that can be easily manufactured by the conventional methods [34, 35].

It can be seen that the thickness of the disk between the first two cells (rA) is less than the thicknesses of the other disks. The simulation results for the fundamental modes of the buncher based on these parameters are shown in Table 2.6.

Table 2.5: Design values of the cavity parameters

Parameter	**Design Value (mm)**		**Parameter**	**Design Value (mm)**
rA	2		rB	3
rC	3		rD	5
rE	5		yA	14
yB	14		yC	14
yD	15		yE	15
hA	39.91		hB	39.93
hC	39.92		hD	39.89

Table 2.6: SUPERFISH results for the buncher frequencies with parameters of 2.5

0-Mode Frequency (MHz)	**$\frac{\pi}{3}$-mode Frequency (MHz)**	**$\frac{2\pi}{3}$-mode Frequency (MHz)**	**π-mode Frequency (MHz)**
2939.5	**2963.2**	**2988.6**	**2998.1**

And the differences between the operating mode and the other modes are:

$$\begin{aligned}
\text{delF1} &= \pi\text{-mode} &-&\quad 0\text{-mode} &= 58.6\text{MHz},\\
\text{delF2} &= \pi\text{-mode} &-&\quad \tfrac{\pi}{3}\text{-mode} &= 34.9\text{MHz},\\
\text{delF3} &= \pi\text{-mode} &-&\quad \tfrac{2\pi}{3}\text{-mode} &= 9.5\text{MHz} \quad .
\end{aligned}$$

According to these results the first condition is achieved, while delF1 is only 58.6 MHz. Thus this difference is less than the expected 62.5 MHz with a relative difference of 6 %, with this value more than 90 % of the effects of the 0-mode will be compensated. One can also calculate the uncompensated effect of the 0-mode using the resonant curve. According to the simulation results the loaded quality factor of the designed cavity is about 8000. Based on [36]

$$f_{1/2} = \frac{f}{2Q_L} \quad , \tag{2.1}$$

the half bandwidth of this cavity ($f_{1/2}$) would be about 187.5 kHz. The difference between the 0-mode and the π-mode is therefore 300 times larger than the bandwidth which means this mode has almost no effect on the operating mode.

2.2.4 Simulation of the input coupler

The last step in designing the buncher cavity is to consider the input RF coupler and the impedance matching between the coupler and the buncher. Figure 2.17 shows an isometric and a cross sectional view of the REGAE buncher cavity with its coaxial input coupler [27].

It is obvious that the buncher and the coupler cannot be simulated together with SUPERFISH because it is a 2D simulation program and there is no axial symmetry when the coupler is added to the buncher cavity. But the effect of the coupler which concerns the part of the power that reflects from the cavity, can be modeled by a lossy material within the SUPERFISH code. The properties of this material can be found from the dimension of the coupler[32]. This lossy material is specified in Figure 2.18.

Since the REGAE coupler is not going to be replaced with a new one it is still possible to use this model to simulate the coupler and it is not necessary to simulate with a 3D program which is slower and less accurate. In order to match the coupler to the cavity it is required that the external and unloaded quality factors be equal [36]. In other words half of the RF power should be lost in the buncher walls that means the power loss in the lossy material should be equal to the power loss in the cavity walls. This condition could be easily achieved by adjusting the position of the coupler. In fact in the SUPERFISH model one should change the position of the inner tube of the coupler which is similar to an antenna inside the

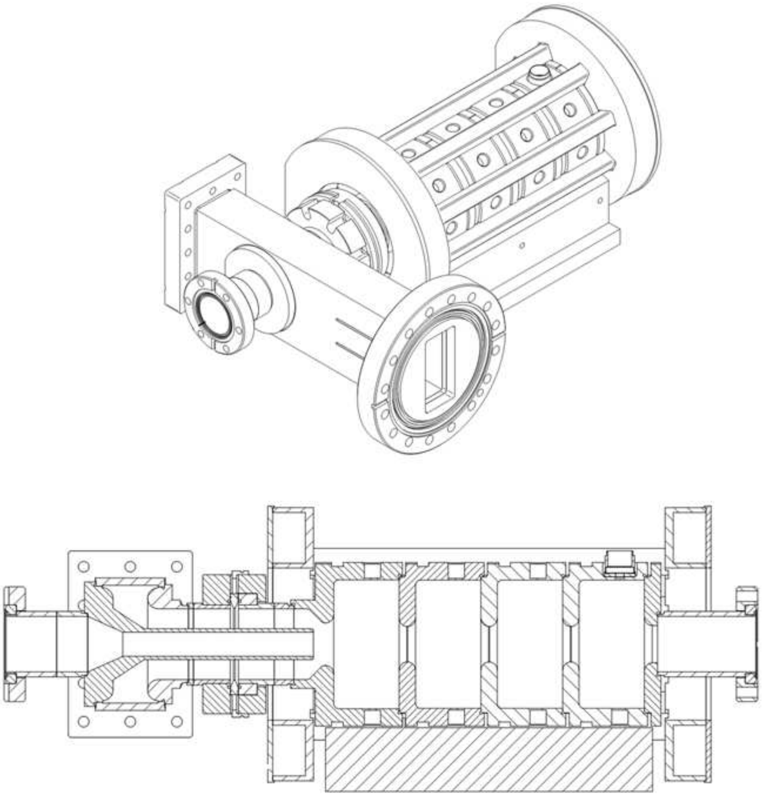

Figure 2.17: Isometric and cross sectional view of the REGAE buncher cavity with its coaxial input coupler

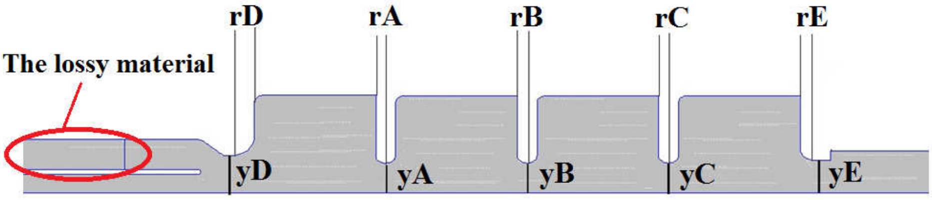

Figure 2.18: The lossy material in the SUPERFISH model

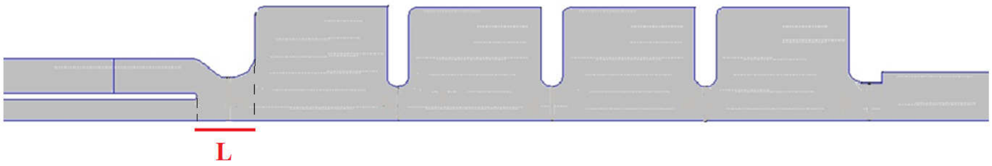

Figure 2.19: The key parameter for adjusting the coupler position (inner tube of the coupler)

buncher. This parameter, L, which plays a key role in adjusting the coupler position is displayed in Figure 2.19. The value of L is already 14.85 mm in the existing cavity and in new design it has to be 18.5 mm.

2.3 Developing a circuit model for the buncher

In the following a circuit model of the buncher cavity is developed in order to gain a deep understanding into the effects of different parts of the buncher on determining the normal mode frequencies. By employing the circuit method one can write and solve the circuit equations instead of the Maxwell equations which is easier and more time efficient. The circuit model is also useful for the tuning process in order to have a guideline during the tuning. But the key point is to consider a precise model which covers relevant properties of the buncher. In general the REGAE buncher includes four pillbox cavities that could be modeled by LC resonance circuits and the interaction of the adjacent cells can be represented by the mutual inductances of the LC circuits [1].

2.3.1 Symmetric model

The first model that is considered for the REGAE buncher is shown in Figure 2.20. In this circuit four similar resonators are coupled to each other with different coupling constants. As mentioned the resonators are similar and have equal resonant frequencies. It can be seen that the circuit model of the coupler is also considered. The coupler is modeled with a transmission line with characteristic impedance of Z_0 and an inductor which is coupled to the first cell and the RF input is modeled with a voltage source. Since for REGAE the buncher is designed to be critically coupled to the feedline (coupling coefficient = 1) half of the input power will be transmitted to the buncher and one can replace the voltage source of V, and the transmission line with a voltage sorce of $\frac{V}{2}$. On the other hand the end

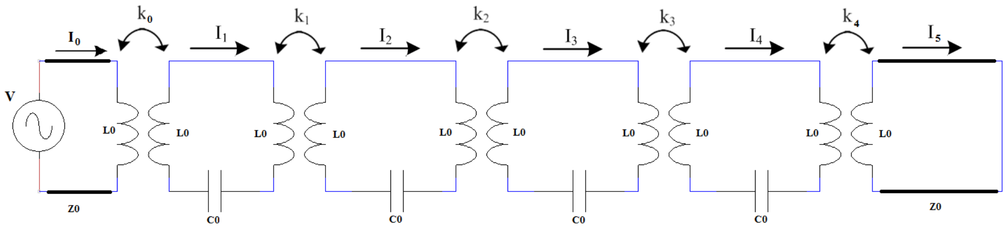

Figure 2.20: The first considered circuit for REGAE buncher. The cavity cells are modeled by the LC circuits and the coupling between them by the mutual inductance between the resonators K_i. The first and end tubes are also modeled by transmision lines with the characteristic impedance of Z_0

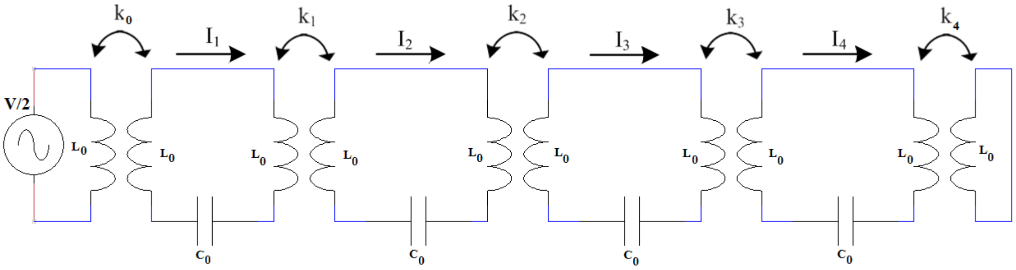

Figure 2.21: The simplified circuit model for the REGAE buncher, see the text for explanation.

tube has to be modeled. Since the power loss at the end of this tube is negligible it can be considered as a short circuit, however, a transmission line is considered before the short circuit since the length of the tube is comparable with the wavelength. One can calculate the input impedance of the end tube using the following equation[36]:

$$Z_{in} = jZ_0 tan\beta l \quad , \tag{2.2}$$

where β is the propagation constant and l is the length of the tube. The resonant frequency of the buncher is about 3 GHz and so its wavelength is about 10 cm. Since the length of the end tube is 5 cm which is half of the wavelength, according to equation (2.2), Z_{in} is equal to zero and one can neglect the transmission line for the end tube in the circuit model. The simplified model of the REGAE buncher is shown in Figure 2.21.

In order to solve this circuit one can write Kirchhoff's Voltage Law (KVL) in six loops. Since the independent sources in a circuit have no effect on the natural frequencies of the circuit it is more simple to turn the sources off in order to calculate the normal modes frequencies of the circuit:

$$\begin{aligned}
&x_0 j\Omega L_0 + x_1 j\Omega k_0 L_0 = 0,\\
&x_1\left(1-\frac{\omega_0^2}{\Omega^2}\right) + x_2\frac{k_1}{2} + x_0\frac{k_0}{2} = 0,\\
&x_2\left(1-\frac{\omega_0^2}{\Omega^2}\right) + x_1\frac{k_1}{2} + x_3\frac{k_2}{2} = 0,\\
&x_3\left(1-\frac{\omega_0^2}{\Omega^2}\right) + x_2\frac{k_2}{2} + x_4\frac{k_3}{2} = 0,\\
&x_4\left(1-\frac{\omega_0^2}{\Omega^2}\right) + x_3\frac{k_3}{2} + x_5\frac{k_4}{2} = 0,\\
&x_5 j\Omega L_0 + x_4 j\Omega k_4 L0 = 0,
\end{aligned} \tag{2.3}$$

Where ω_0 is the resonant frequency of the individual resonators if they were uncoupled which is equal to $\frac{1}{\sqrt{2L_0C_0}}$, Ω is the assumed frequency of a steady-state oscillation (normal mode), $k_n = \frac{M_n}{L_0}$ are the coupling constants (M_n are the mutual inductance between the adjacent inductors), and x_n are normalized currents, defined in terms of the real current i_n by $x_n = \frac{i_n}{\sqrt{2L_0}}$. The first and the last equations in the equation set 2.3 result in:

$$\begin{aligned}
&x_0 = -k_0 x_1,\\
&x_5 = -k_4 x_4,
\end{aligned} \tag{2.4}$$

substituting equation 2.4 in equation 2.3:

$$\begin{aligned}
&x_1\left(1-\frac{\omega_0^2}{\Omega^2}-\frac{k_0^2}{2}\right) + x_2\frac{k_1}{2} = 0,\\
&x_2\left(1-\frac{\omega_0^2}{\Omega^2}\right) + x_1\frac{k_1}{2} + x_3\frac{k_2}{2} = 0,\\
&x_3\left(1-\frac{\omega_0^2}{\Omega^2}\right) + x_2\frac{k_2}{2} + x_4\frac{k_3}{2} = 0,\\
&x_4\left(1-\frac{\omega_0^2}{\Omega^2}-\frac{k_4^2}{2}\right) + x_3\frac{k_3}{2} = 0,
\end{aligned} \tag{2.5}$$

In these equations we can neglect k_0^2 and k_4^2 in comparison with the other terms. So the simplified equation for the circuit can be written as follows:

$$\begin{aligned}
&x_1\left(1-\frac{\omega_0^2}{\Omega^2}\right) + x_2\frac{k_1}{2} = 0,\\
&x_2\left(1-\frac{\omega_0^2}{\Omega^2}\right) + x_1\frac{k_1}{2} + x_3\frac{k_2}{2} = 0,\\
&x_3\left(1-\frac{\omega_0^2}{\Omega^2}\right) + x_2\frac{k_2}{2} + x_4\frac{k_3}{2} = 0,\\
&x_4\left(1-\frac{\omega_0^2}{\Omega^2}\right) + x_3\frac{k_3}{2} = 0,
\end{aligned} \tag{2.6}$$

Equation (2.6) can be written in matrix form as:

$$LX = \frac{\omega_0^2}{\Omega^2}X \qquad , \tag{2.7}$$

where

$$L=\begin{bmatrix} 1 & \frac{k_1}{2} & 0 & 0 \\ \frac{k_1}{2} & 1 & \frac{k_2}{2} & 0 \\ 0 & \frac{k_2}{2} & 1 & \frac{k_3}{2} \\ 0 & 0 & \frac{k_3}{2} & 1 \end{bmatrix}, X=\begin{bmatrix} x_1 \\ x_2 \\ x_3 \\ x_4 \end{bmatrix} \quad . \tag{2.8}$$

According to equation (2.7) which is an eigenvalue equation, $\frac{\omega_0^2}{\Omega^2}$ is the eigenvalue of matrix L . So by calculating the four eigenvalues of the matrix L one can find the four normal mode frequencies of the buncher. Solving the following equation:

$$det\begin{bmatrix} 1-\lambda & \frac{k_1}{2} & 0 & 0 \\ \frac{k_1}{2} & 1-\lambda & \frac{k_2}{2} & 0 \\ 0 & \frac{k_2}{2} & 1-\lambda & \frac{k_3}{2} \\ 0 & 0 & \frac{k_3}{2} & 1-\lambda \end{bmatrix}=0 \quad , \tag{2.9}$$

where λ are the eigenvalues and consequently the normal mode frequencies would be: $\Omega=\frac{\omega_0}{\sqrt{\lambda}}$. The four solutions to this equation are:

$$\Omega=\frac{\omega_0}{\sqrt{1\pm\frac{1}{2}\sqrt{\frac{1}{2}\left[\left(k_1^2+k_2^2+k_3^2\right)\pm\sqrt{k_1^4+k_2^4+k_3^4+k_1^2k_2^2-k_1^2k_3^2+k_2^2k_3^2}\right]}}} \quad . \tag{2.10}$$

According to the above equation one can draw the absolute value of the frequencies and also their differences as a function of the coupling constants. Such curves are displayed in Figure 2.22 and Figure 2.23.

One can see from these figures that for all coupling constants a symmetry exists for the normal modes frequencies. In other words the difference between the first two frequencies is always equal to the difference between two others. This is more obvious in Figurte 2.23 while according to the Table 2.1 in the existing cavity this situation doesn't exist. So the considered model is not precise and should be developed further.

2.3.2 Asymmetric model

A more comprehensive model is shown in Figure 2.24. In this model different resonant frequencies are considered for the four cells and also it is assumed that the coupling constants are not equal.
Such as the previous model one can write the KVL equations for the above circuit.

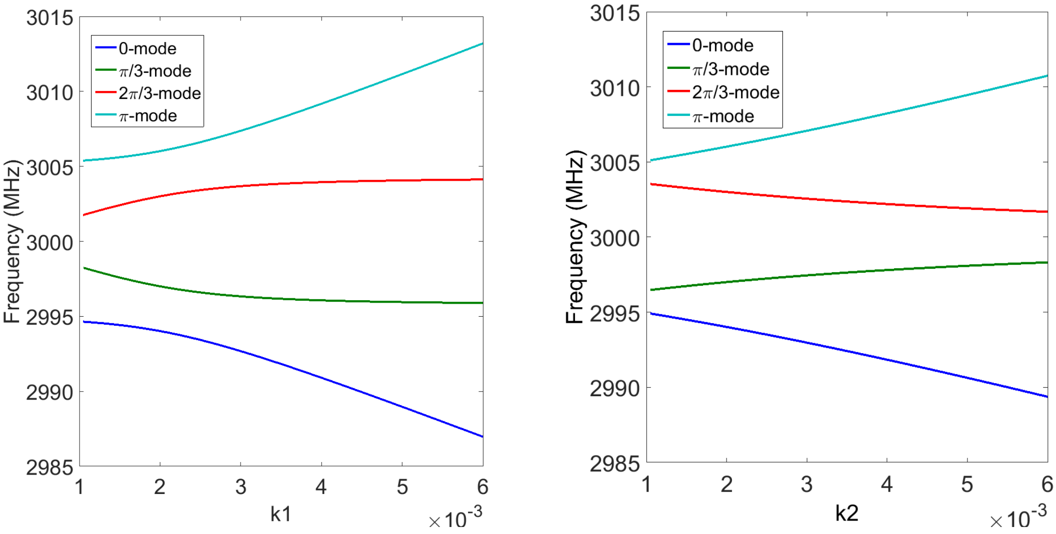

Figure 2.22: The absolute value of the frequencies for the normal modes of the circuit displayed in Figure 2.21 vs. coupling constants

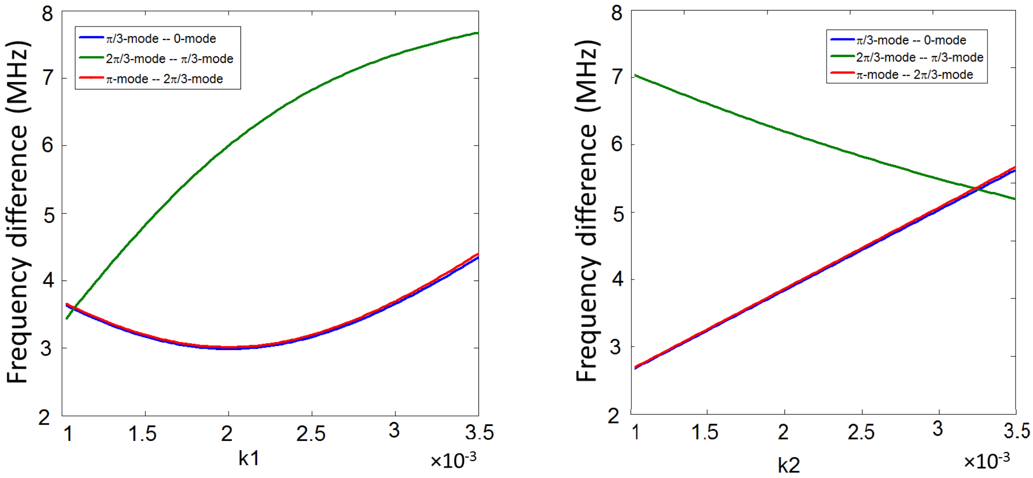

Figure 2.23: Difference between adjacent modes of the circuit displayed in Figure 2.21 vs. coupling constants

These equation after simplifications that are explained for the first circuit, are as

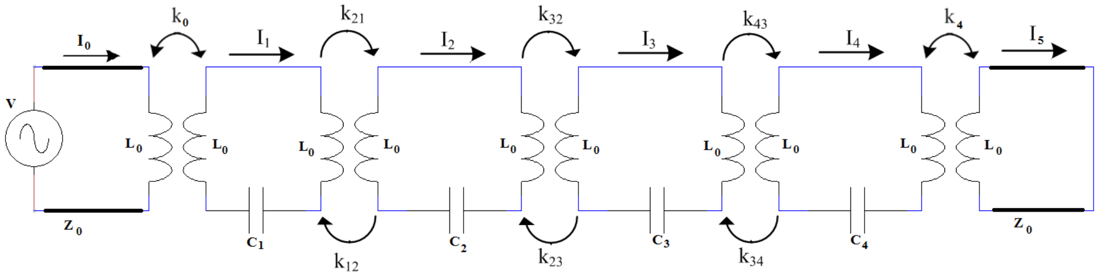

Figure 2.24: The more comprehensive circuit model for the REGAE buncher. In this model the resonant frequency of the cells as well as the coupling between them are assumed to be different.

follows:

$$
\begin{aligned}
&x_1\left(1-\tfrac{\omega_{01}^2}{\Omega^2}\right)+x_2\tfrac{k_{12}}{2}=0,\\
&x_2\left(1-\tfrac{\omega_{02}^2}{\Omega^2}\right)+x_1\tfrac{k_{21}}{2}+x_3\tfrac{k_{22}}{2}=0,\\
&x_3\left(1-\tfrac{\omega_{03}^2}{\Omega^2}\right)+x_2\tfrac{k_{32}}{2}+x_4\tfrac{k_{34}}{2}=0,\\
&x_4\left(1-\tfrac{\omega_{04}^2}{\Omega^2}\right)+x_3\tfrac{k_{43}}{2}=0,
\end{aligned}
\tag{2.11}
$$

Where ω_{0n} are the resonant frequencies of the individual resonators if they were uncoupled which are again equal to $\frac{1}{\sqrt{2L_0C_n}}$. The equations for this model are more complicated than the first model as a result of considering different resonators. However they still can be written as an eigenvalue equation:

$$
LX=\frac{1}{\Omega^2}X \quad , \tag{2.12}
$$

where

$$
L=\begin{bmatrix}
\frac{1}{\omega_{01}^2} & \frac{k_{12}}{2\omega_{01}^2} & 0 & 0\\
\frac{k_{21}}{2\omega_{02}^2} & \frac{1}{\omega_{02}^2} & \frac{k_{23}}{2\omega_{02}^2} & 0\\
0 & \frac{k_{32}}{2\omega_{03}^2} & \frac{1}{\omega_{03}^2} & \frac{k_{34}}{2\omega_{03}^2}\\
0 & 0 & \frac{k_{43}}{2\omega_{04}^2} & \frac{1}{\omega_{04}^2}
\end{bmatrix} \quad , \tag{2.13}
$$

and

$$
X=\begin{bmatrix} x_1\\ x_2\\ x_3\\ x_4 \end{bmatrix} \quad ,
$$

is the vector of normalized currents. In order to find the eigenvalues and consequently the resonant frequencies the following equation has to be solved:

$$det \begin{bmatrix} \frac{1}{\omega_{01}^2}-\lambda & \frac{k_{12}}{2\omega_{01}^2} & 0 & 0 \\ \frac{k_{21}}{2\omega_{02}^2} & \frac{1}{\omega_{02}^2}-\lambda & \frac{k_{23}}{2\omega_{02}^2} & 0 \\ 0 & \frac{k_{32}}{2\omega_{03}^2} & \frac{1}{\omega_{03}^2}-\lambda & \frac{k_{34}}{2\omega_{03}^2} \\ 0 & 0 & \frac{k_{43}}{2\omega_{04}^2} & \frac{1}{\omega_{04}^2}-\lambda \end{bmatrix} = 0 \quad , \tag{2.14}$$

with the resonant frequencies as: $\Omega = \frac{1}{\sqrt{\lambda}}$. Equation (2.14)) can be solved numerically by MATLAB [37]. Some results of solving this equation in order to find out the impact of changing the circuit elements on the fundamental frequencies of the buncher are shown in Figure 2.25. One of the most important parameters of the buncher, which to be considered for the application of buncher and also during its tuning, is the electric field pattern inside the cells. It is possible to calculate the ratio of the maxima of the electric field inside the cells based on the circuit model. In fact the electric field in the cavities can be translated into the currents of the LC loops in the circuit model, and according to the equation (2.12) these currents can be easily found by calculating the eigenvectors of matrix L. By defining the ratio of the maxima of the electric fields in the cells as:

$$r_{21} = \frac{max|E_2|}{max|E_1|} \quad r_{31} = \frac{max|E_3|}{max|E_1|} \quad r_{41} = \frac{max|E_4|}{max|E_1|} \quad .$$

One solves following equations to find the above parameters:

$$\begin{bmatrix} \left(\frac{1}{\omega_{01}^2}-\frac{1}{\Omega^2}\right) & \frac{k_{12}}{2\omega_{01}^2} & 0 & 0 \\ \frac{k_{21}}{2\omega_{02}^2} & \left(\frac{1}{\omega_{02}^2}-\frac{1}{\Omega^2}\right) & \frac{k_{23}}{2\omega_{02}^2} & 0 \\ 0 & \frac{k_{32}}{2\omega_{03}^2} & \left(\frac{1}{\omega_{03}^2}-\frac{1}{\Omega^2}\right) & \frac{k_{34}}{2\omega_{03}^2} \\ 0 & 0 & \frac{k_{43}}{2\omega_{04}^2} & \left(\frac{1}{\omega_{04}^2}-\frac{1}{\Omega^2}\right) \end{bmatrix} \begin{bmatrix} 1 \\ r_{21} \\ r_{31} \\ r_{41} \end{bmatrix} = 0 \quad . \tag{2.15}$$

The result to this matrix equation is as follows:

$$\begin{aligned} r_{21} &= \frac{2\left(\frac{\omega_{01}^2}{\Omega^2}-1\right)}{k_{12}}, \\ r_{31} &= \frac{4\omega_{01}^2\omega_{02}^2\left(\frac{1}{\omega_{01}^2}-\frac{1}{\Omega^2}\right)\left(\frac{1}{\omega_{02}^2}-\frac{1}{\Omega^2}\right)}{k_{12}k_{23}}, \\ r_{41} &= \frac{k_{43}\omega_{01}^2\omega_{02}^2\left(\frac{1}{\omega_{01}^2}-\frac{1}{\Omega^2}\right)\left(\frac{1}{\omega_{02}^2}-\frac{1}{\Omega^2}\right)}{k_{12}k_{23}\left(\frac{1}{\Omega^2}-\frac{1}{\omega_{04}^2}\right)} - \frac{k_{43}k_{21}}{2k_{23}\left(\frac{\omega_{04}^2}{\Omega^2}-1\right)}. \end{aligned} \tag{2.16}$$

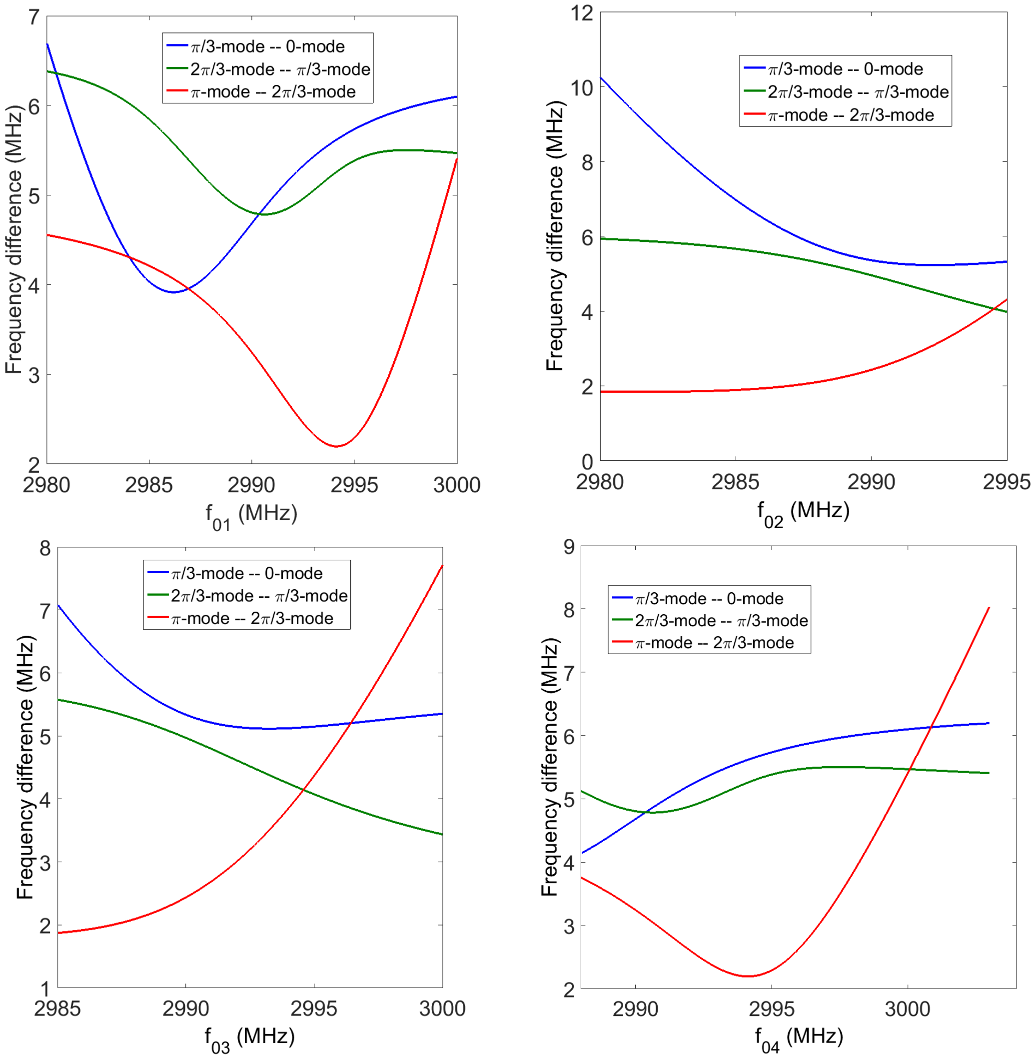

Figure 2.25: The calculation results for delFs vs. individual resonant frequencies of the cells based on the circuit model displayed in Figure 2.24

Equation (2.16) declares that by changing the resonant frequency of one cell the ratio of the electric fields in all cells will vary. Such variations are shown in Figure 2.26.

2.3.3 Validation of the proposed circuit model

As declared in the beginning of this section it is critical to have a precise model in order to exploit the benefits of the circuit model. To find out how exact the proposed model is one can make some comparisons between simulation results

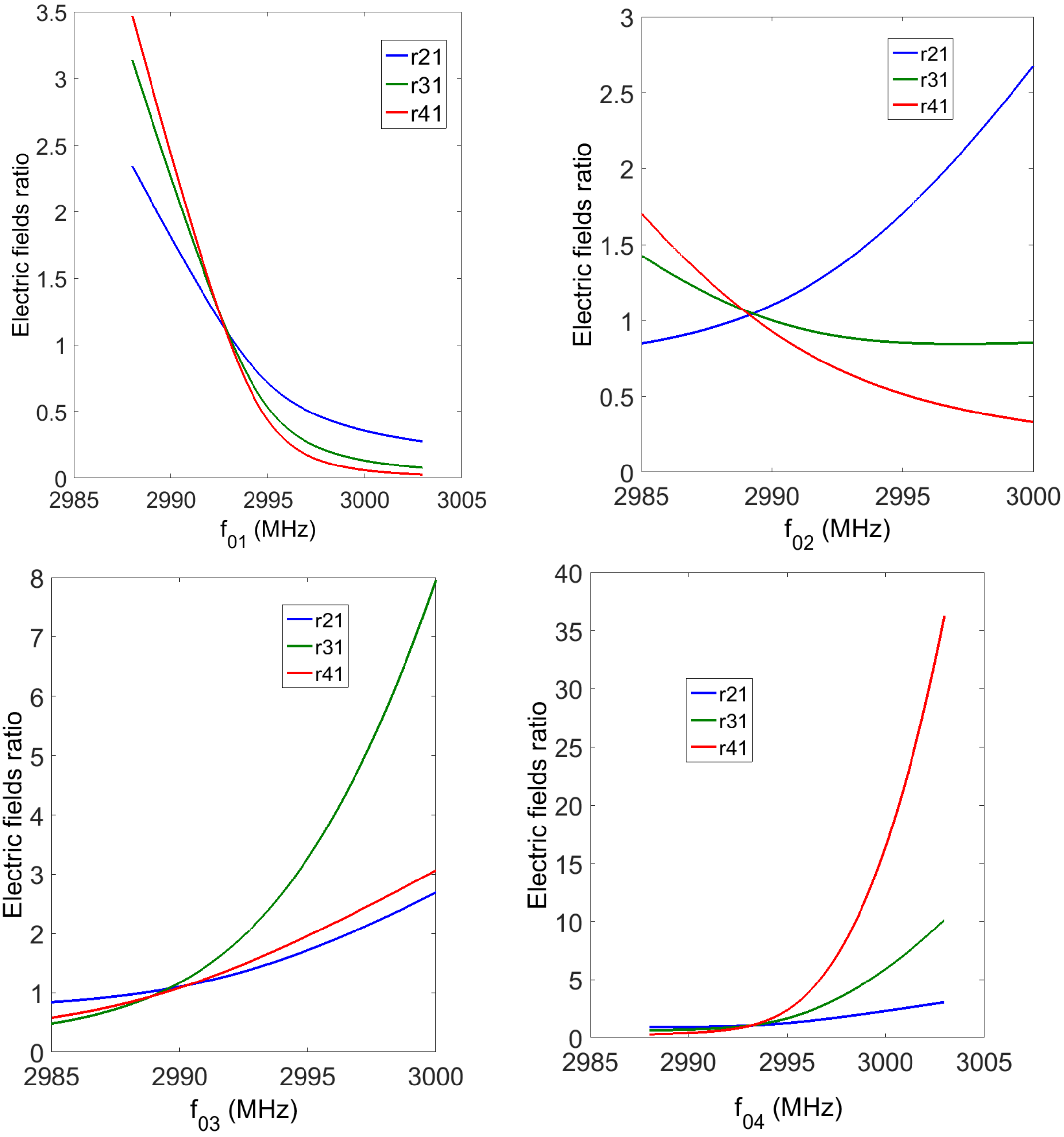

Figure 2.26: Electric field ratios vs. individual resonant frequencies of the resonators based on the circuit model displayed in Figure 2.24

and the results obtained from the circuit model. Figure 2.27 shows such comparisons. In this figure the two upper curves are the model results which display the difference between adjacent normal modes as a function of individual resonant frequencies of the first and the second cell while the lower curves are the SUPERFISH results that display the difference between adjacent modes versus cell diameters. A decrease in one cell diameter and consequently decrease in its volume leads to an increase in the resonant frequency of the respective cell. Hence in order to have a better comparison the horizontal axis of the SUPERFISH results are set to show the values in reverse order. So in each series of the curves, from left to right the individual resonant frequency of the specified cell is increasing. As it can be seen the characteristics of changes are similar to each other. The coupling constant effects can also be compared. In order to perform such comparison the thickness of the disks between cavities is considered as the key parameter in determining the coupling constant between the adjacent cells. In Figure 2.28 the

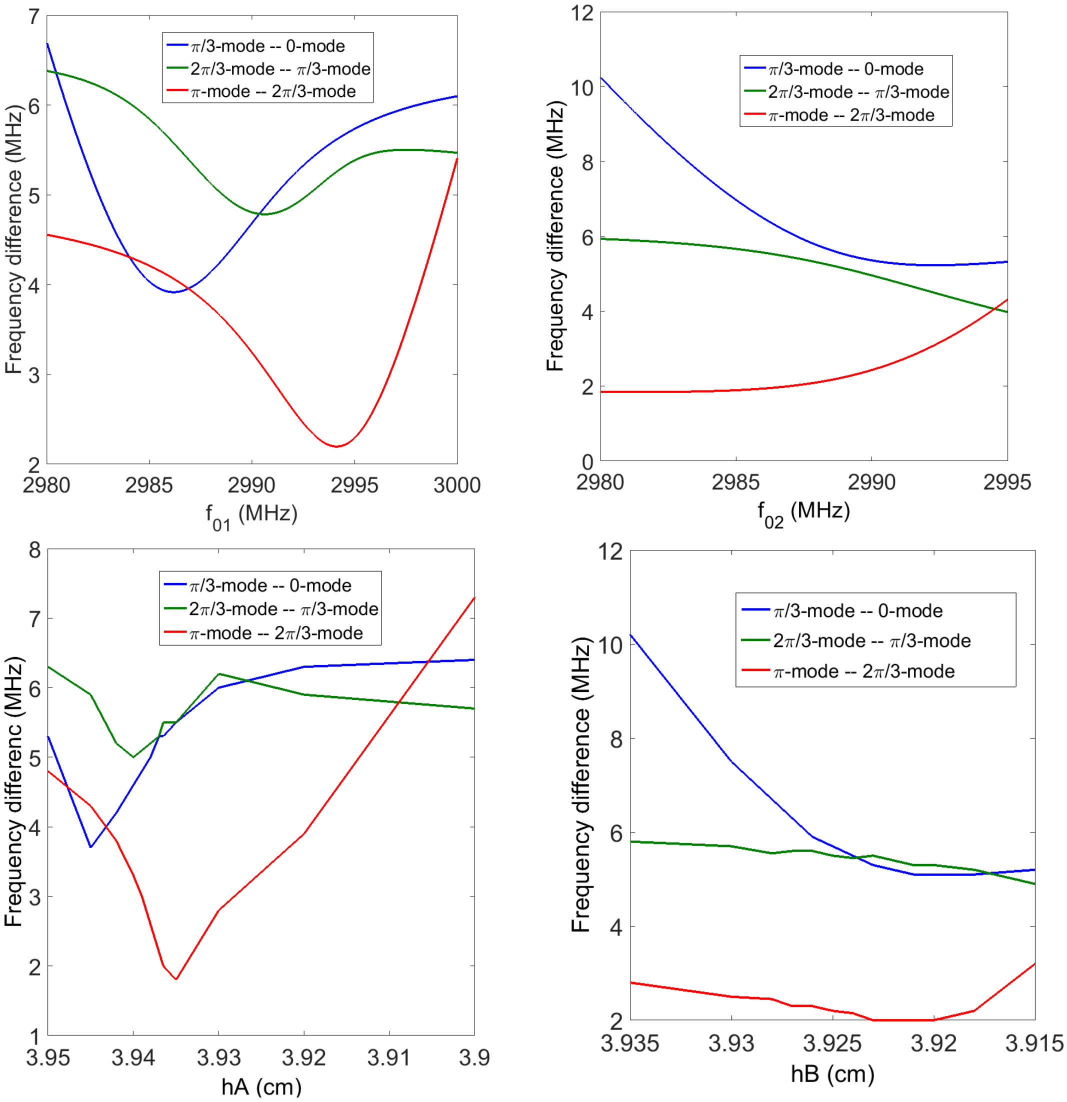

Figure 2.27: Comparison between the circuit model results (top) and SUPERFISH simulation results (bottom)

effects of changing this parameter is compared to the results of the circuit model when the coupling constant is varied in a reasonable range. It should be noted that for all these comparisons the values of the horizontal axis which indicate the parameters that change the fundamental modes are not scaled. In comparison with Figure 2.27, less agreement between SUPERFISH results and the circuit model results can be observed in Figure 2.28. The reason can be explained by bearing in mind that changing the thickness of the iris disks between cavities has two effects. The first and the most dominant effect is varying the coupling constants but it also makes a little change in the individual resonant frequency of the cells. As it can be seen in Figure 2.4 the connection parts between adjacent cells in the cross sectional view are 180 degree curves and changing the thickness of the disks in the simulation is fulfilled by varying the radii of these curves which obviously leads to a little change in the volume of the cavities in addition to the coupling constants.
one cannot expect strong agreement between the calculations based on the circuit model and the simulation results. Since there are parameters that cannot be modeled by the circuit (or at least make the model too complicated), such as bent edges of the cells and the iris openings or poor couplings between nonadjacent modes. But as we will see in the next chapter, the main reason of introducing this model is to use it in the tuning process. In section 3.6.3 it will be argued that for tuning the cavity using the circuit model we need to know about the quality of changes, in fact only the slopes in the displayed figures. One can therefore conclude that the proposed model is accurate enough to satisfy our requirements.

2.4 Beam dynamic simulations

As mentioned in the first section, the input RF power excites the non-operating normal modes of the buncher in addition to the π-mode and so some contribution of these modes exist in the total electric field inside the cells which can cause a small change in the phase advance between the buncher cells. This change influences the transverse and longitudinal beam parameters such as bunch length and beam emittance. So it seems to be necessary to perform some beam dynamic simulations in order to find the effects of different modes on the electron beam. For the beam dynamic simulations the tracking program ASTRA (A Space Charge Tracking Algorithm) has been used [38]. The simulation conditions and results are explained in the following. It should be noted that the main goal of this part is to investigate the effects of the $2\pi/3$-mode on the beam properties in both the existing and in the newly designed cavity.

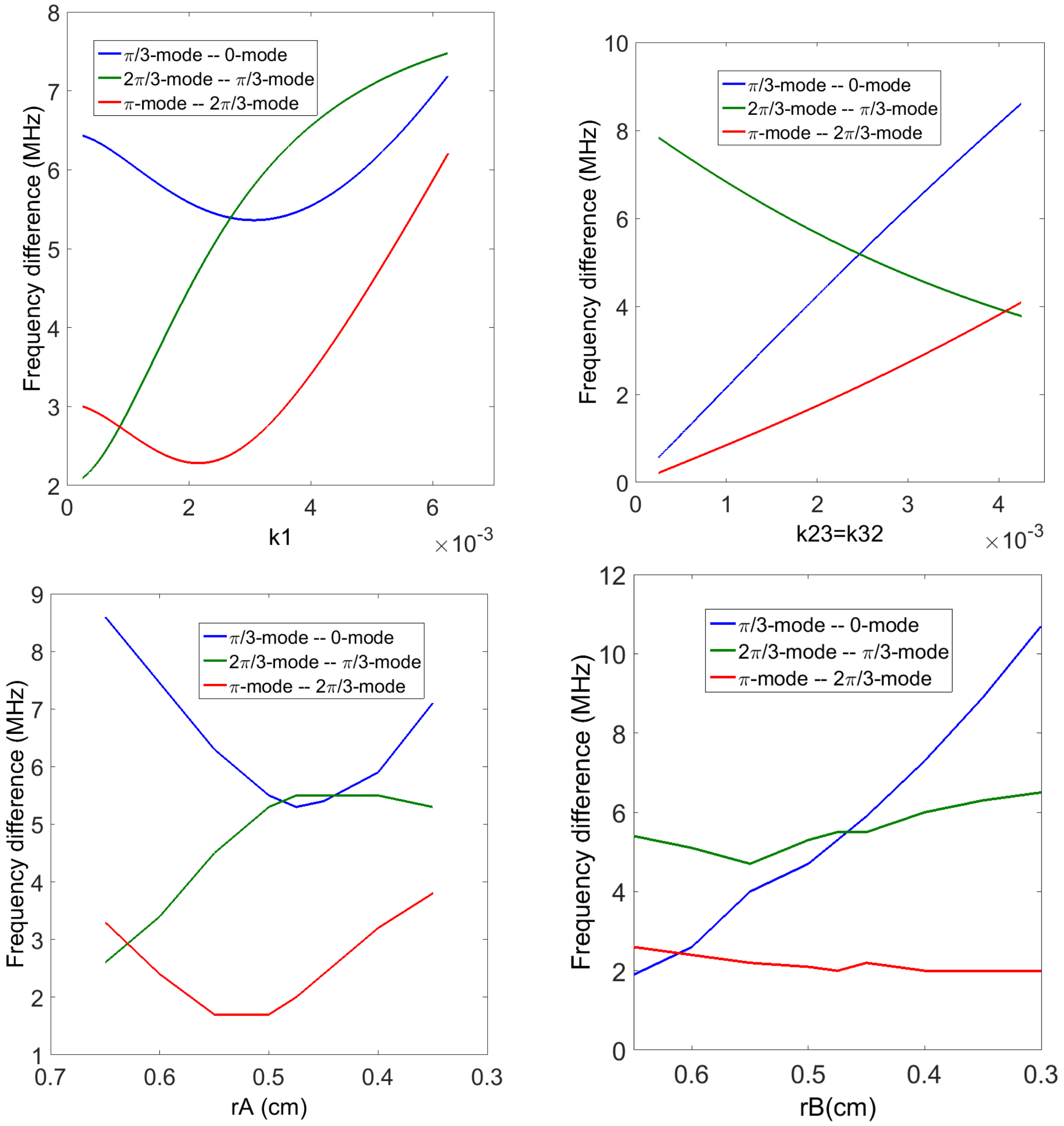

Figure 2.28: Comparison between the circuit model (top) results and SUPERFISH simulation results (bottom)

2.4.1 Bunch length

The bunch length variations in a drift behind the buncher cavity is simulated using ASTRA. The longitudinal distribution of the bunch is Gaussian with an rms width of 0.5 mm and a cut at 2 sigma. The transverse particle distribution in both vertical and horizontal directions is also Gaussian with an rms width of 0.5 mm. And the kinetic energy of the bunch is set to 5 MeV. The distribution of the transverse

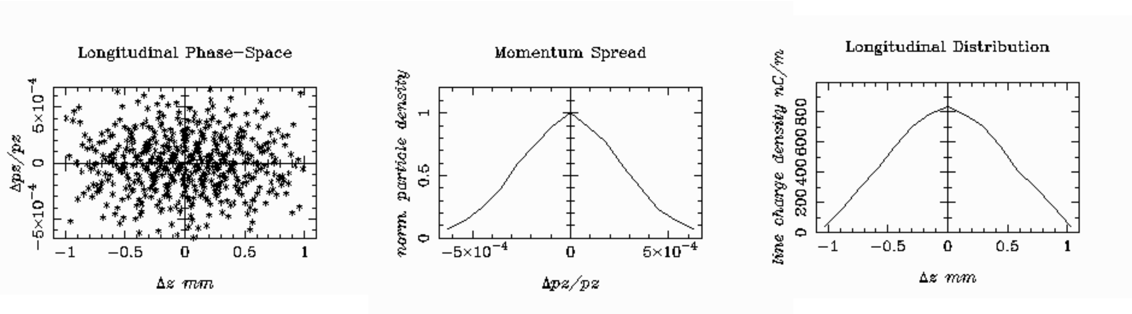

Figure 2.29: The initial properties of the simulated bunch. *left:* longitudinal phase space *middle:* momentum spread *right:* longitudinal distribution

momenta is also Gaussian in x and y direction and the rms value of the energy spread is set to be 1.5 keV. The total charge of the bunch is 1 pC. The initial properties of the simulated bunch is shown in Figure 2.29.

The ASTRA result of the bunch length for the existing buncher without $2\pi/3$-mode is shown in Figure 2.30. As it can be seen a 10 meter drift path is assumed behind the buncher. The simulation is performed for different phases of the π-mode and its results indicate that by changing this phase the minimum achievable bunch length will vary, and also the distance in which this minimum occurs can be moved by changing the phase of the π-mode. In order to have the best efficiency of the operation the target should be located in the point at which the minimum bunch length occurs. Regardless of the location of the target, the minimum achievable bunch length varies by changing the π-mode phase. Figure 2.31 illustrates this. The dependance of the minimum achievable bunch length on the phase of the π-mode is because of the cosine-like non-linearity of the electric filed applied to the bunch when going off the zero crossing. According to this curve by increasing the phase from -100° to -30° the minimum achievable bunch length increases. It should be noted that one can change the minimum achievable bunch length by changing the other parameters of the buncher such as its field gradient. Here the effect of the bunching phase is only investigated.

The simulations are performed both for the existing buncher and the new design. Furthermore two scenarios are considered. First, the $2\pi/3$-mode is neglected and the only effective mode is the π-mode. But in the second scenario the electric field component due to the $2\pi/3$-mode is included. In all the simulations the coherent space charge effect is not considered. Considering the low current beam in the cavity and the fact that the aim of these simulations is to investigate the effect of the buncher cavities alone, especially the effect of the $2\pi/3$-mode, one can neglect the space charge effects. In the second scenario we have to note that although the

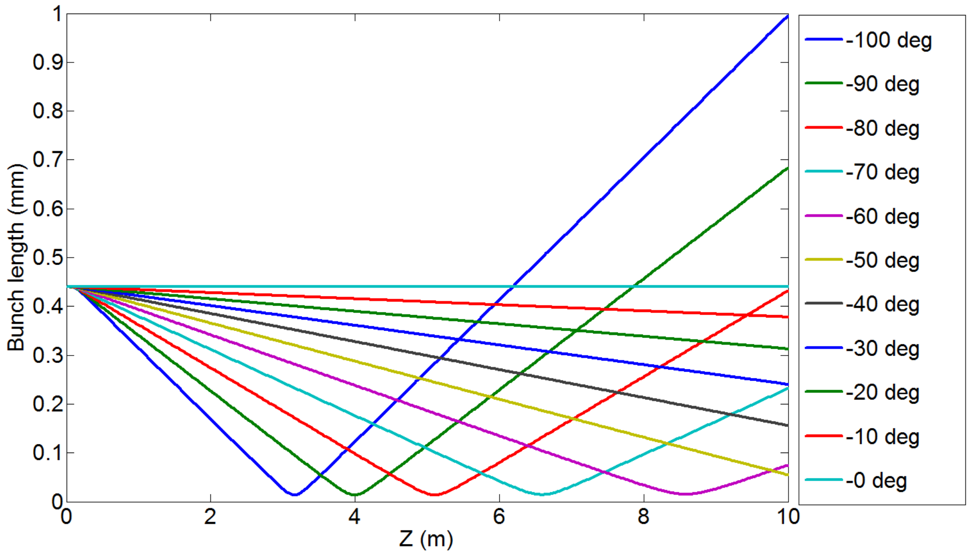

Figure 2.30: The simulation results for the bunch length along the z-axis for the existing buncher

fundamental frequency of the $2\pi/3$-mode differs from the π-mode frequency, in the beam dynamics simulation it is necessary to consider the same frequency as for the π-mode for $2\pi/3$-mode electric field. This is because the buncher is exited with the π-mode frequency and the other modes will oscillate with this frequency. However the contribution of the other modes is much less than the π-mode. The contribution which needs to be translated into the amplitude of the electric fields in the ASTRA input is inversely proportional to the difference between the π-mode frequency and the other normal modes' frequencies and can be calculated from the resonance curve. Using this curve and the SUPERFISH results for the quality factor, the contribution of the $2\pi/3$-mode is about 10% for the existing cavity and about 2% for the new design.

Simulation results for the new designed buncher are also shown in Figure 2.32. In these curves the $2\pi/3$-mode is also neglected and a 10 meter drift path is considered behind the buncher. It can be seen that the results for the new cavity is similar to the existing one. This result was expected, because the input power and the operating frequency in both cases are equal. Noting that the electric field distributions of the π-mode for the existing and the newly designed cavity are nearly identical, similar results have to be achieved when the $2\pi/3$-mode is neglected.

The difference between the new designed buncher and the old one will be clarified when the $2\pi/3$-mode is included. In order to quantity the effect of the $2\pi/3$-mode

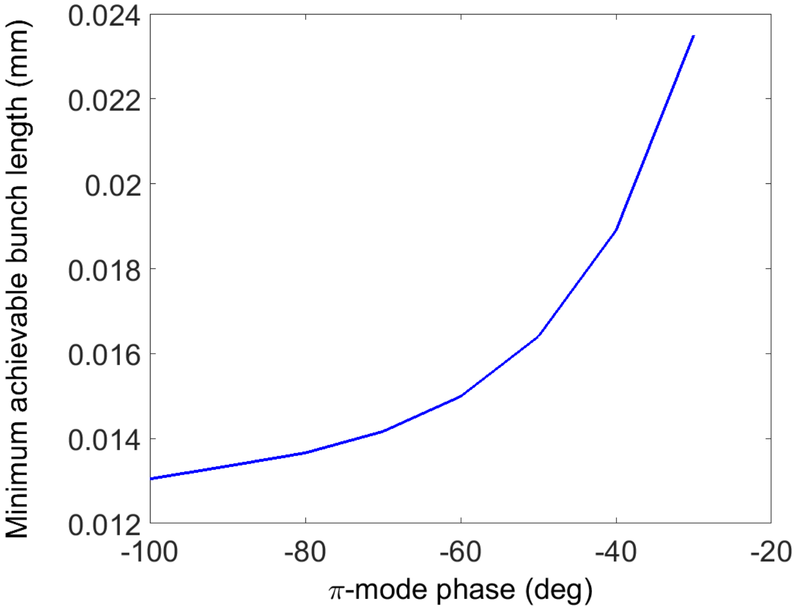

Figure 2.31: Minimum achievable bunch length versus π-mode phase

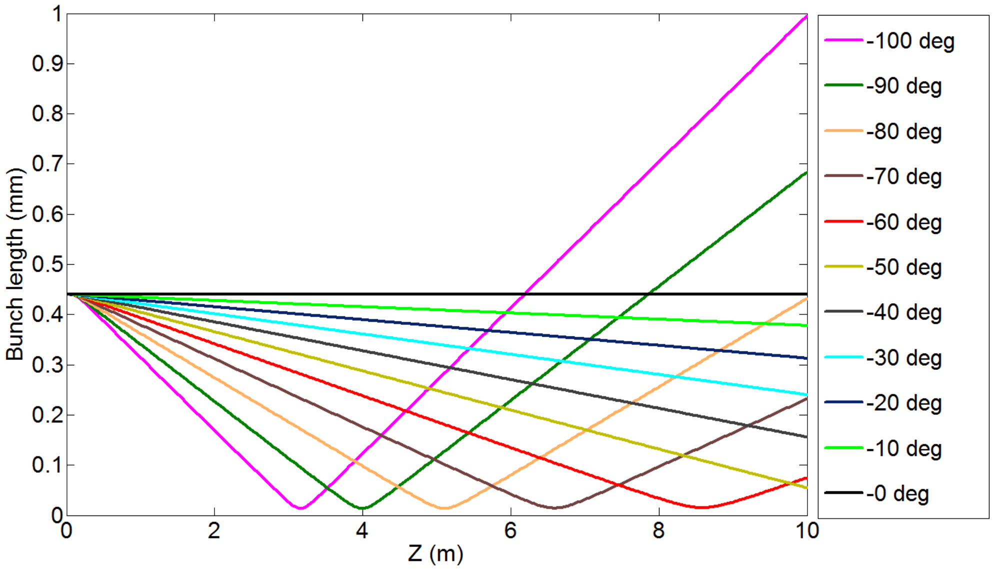

Figure 2.32: The simulation results for the bunch length along the z-axis for the new designed buncher

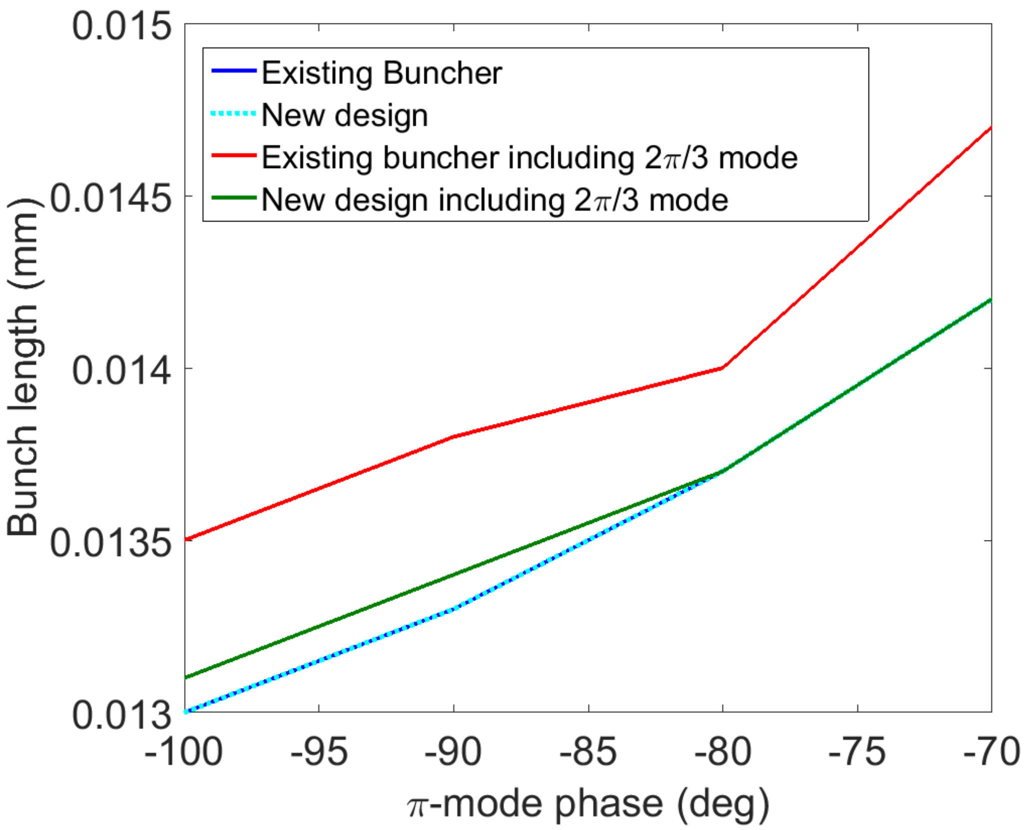

Figure 2.33: Comparison of the effect of $2\pi/3$-mode for the existing cavity and the new design.

the minimal bunch length is investigated for all possible phase differences between π-mode and $2\pi/3$-mode. Since the phase of the $2\pi/3$-mode is unknown the maximum value of the bunch length has to be considered. According to this explanation the minimum achievable bunch length for the existing and the new designed buncher in absence and presence of the $2\pi/3$-mode are compared in Figure 2.33. In this figure the results for the new designed buncher and the existing one in the absence of $2\pi/3$-mode are identical as was mentioned before. But in presence of the $2\pi/3$-mode, the situation is better with the newly designed buncher. The main reason is the large difference between these two fundamental modes in the new design which will decrease the contribution of $2\pi/3$-mode from 10% in the existing cavity down to 2% in the new designed buncher. However, the change of the minimum achievable bunch length using the newly designed cavity is just about 4% that seems not to be considerable. One can conclude from this figure that the $2\pi/3$-mode has a weak contribution in determining the bunch length in both cavities.

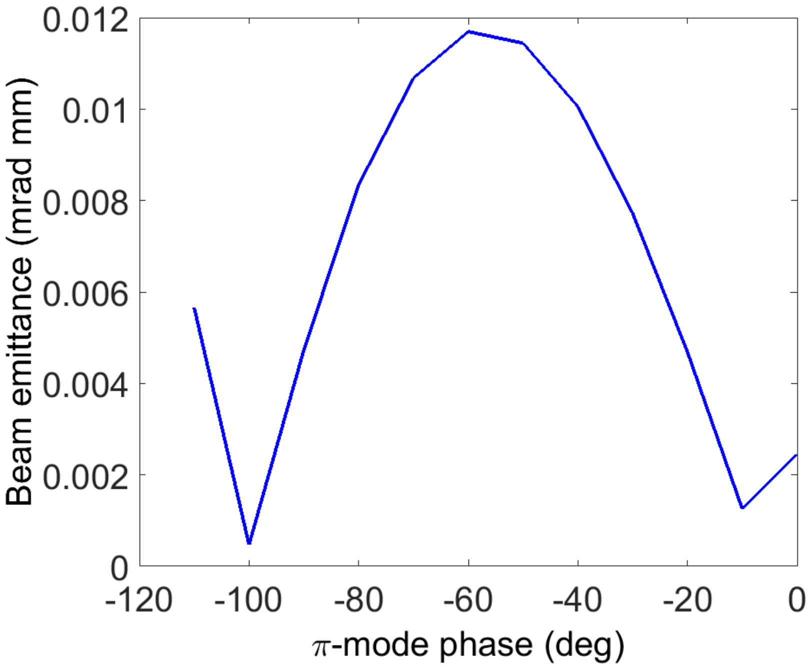

Figure 2.34: The beam emittance for the existing buncher

2.4.2 Beam emittance

The other parameter investigated with ASTRA is the transverse beam emittance. First the beam emittance at the end of the buncher is simulated for both, the existing cavity and the new buncher in the absence of the $2\pi/3$-mode. The result is shown in Figure 2.34 and Figure 2.35. It can be seen that the results for the beam emittance are similar for two cases again. The minimum emittance can be achieved on the phase of $-100°$ for the π-mode. Again the difference between the existing buncher and new design is clarified when the $2\pi/3$-mode is added. Similar to the previous simulation, the relative strength of the $2\pi/3$-mode is deducted from the resonant curve. To calculate the effect of the $2\pi/3$-mode the emittance result in absence of the $2\pi/3$-mode is subtracted from the emittance result with the $2\pi/3$-mode. As for the bunch length case all possible phases for the $2\pi/3$-mode have been simulated and the maximum value of the emittance has been considered as the total emittance in the presence of the $2\pi/3$-mode. Figure 2.36 displays the contribution of the $2\pi/3$-mode to the beam emittance for the new designed buncher and for the old one. Here we should note that the contribution of the $2\pi/3$-mode is not strongly dependent on the π-mode phase, however, it decreases by increasing the π-mode phase. Thus the $2\pi/3$-mode contribution to the total emittance is always on the order of some 10^{-4} mrad mm. As for the bunch

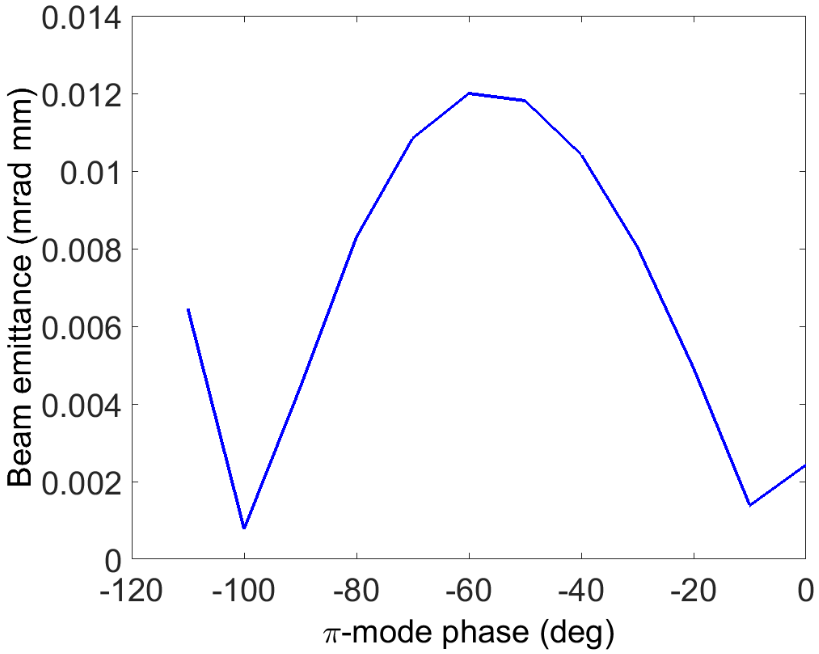

Figure 2.35: The beam emittance for the new designed buncher

length the effects of the $2\pi/3$-mode on the emittance is lower for the new design than for the existing cavity which is a result of the better mode separation.

2.5 Summary and conclusion

A new buncher cavity has been designed for REGAE. In the existing buncher cavity at REGAE the difference between the π-mode which is the operating mode and other TM_{010} normal modes (specially $2\pi/3$-mode) is small in terms of resonant frequency which causes some unwanted effects on the machine operation. Physical parameters of the cavity such as thickness of the disks between the cavity cells, iris radii and diameter of the cells have been adjusted to improve the mode separation. In the newly designed cavity the differences between the π-mode and the $2\pi/3$-mode, π-mode and 0-mode have been increased from 2, 7 and 12 MHz in the existing cavity to 9.5, 35 and 59 MHz. Beam dynamics simulations show that the unwanted effects of the other modes on the bunch length and transverse beam emittance are not considerable both for the existing cavity and the newly designed one. However, such effects will decrease using the new cavity. A circuit model for the designed cavity has been proposed that clarifies the operation

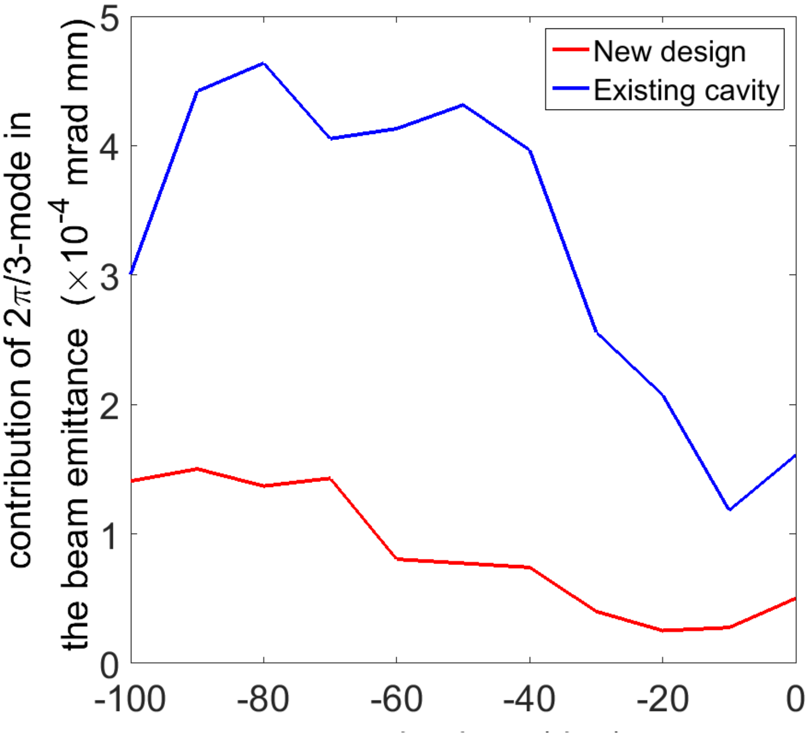

Figure 2.36: The contribution of $2\pi/3$-mode in the beam emittance

of the cells and their coupling mechanism. Validity of the introduced model has also been verified using the simulation results. As a novel method we can use the proposed model to optimize the tuning process of the cavity. Such algorithm is explained in details in the next section.

Chapter 3

Design of a normal conductive cavity for arrival time stabilization at FLASH

3.1 Introduction

The European XFEL will provide short laser pulses to study the dynamics of molecular and chemical reactions on an atomic level. To generate the Angstrom wavelength laser pulses, a high-quality electron beam is accelerated in superconducting cavities to an energy of 17.5 GeV and then sent through long magnetic undulators [39]. The Angstrom laser light is used e.g. to study the temporal dynamics of matter typically carried out in a pump-probe arrangement, where atoms or molecules are excited by an external ultra-short pulse optical laser while their reactions are visualized using the FEL light [40]. To achieve the required femtosecond resolution a precise regulation of bunch arrival time within a train of electron bunches is needed. For FEL users, it is therefore essential that the arrival time of the individual radiation pulses has a stability with precision of only a few femtoseconds [41].

The Free Electron Laser FLASH at Hamburg, which is a smaller scale version of the European XFEL, provides a unique possibility to test and develop hardware and software which are comparable to those required by the XFEL. It has been shown, that beam-based feedback loops stabilize the bunch arrival time in the femtoseconds range [42]. Further minimizing the bunch arrival time jitter requires faster actuators, e.g. a normal conducting cavity with higher bandwidth compared to narrow-band superconducting cavities. A normal conducting cavity is therefore designed for this purpose. This cavity is going to be installed at the FLASH main line as shown in Figure 3.1. Concerning the space limitation in FLASH a side coupling to this cavity is required. Since the input power of the cavity is about 1 kW it seems to be most efficient if the input power could be coupled to the cavity via a loop antenna instead of a waveguide coupler. In addition to space limits, it is more convenient to adjust the coupling constant by engaging the loop couplers. Besides, since the power supply is a solid sate amplifier whit a coaxial cable as output it would be easier to connect its output directly to a feedthrough instead of using a coaxial-to-waveguide converter.

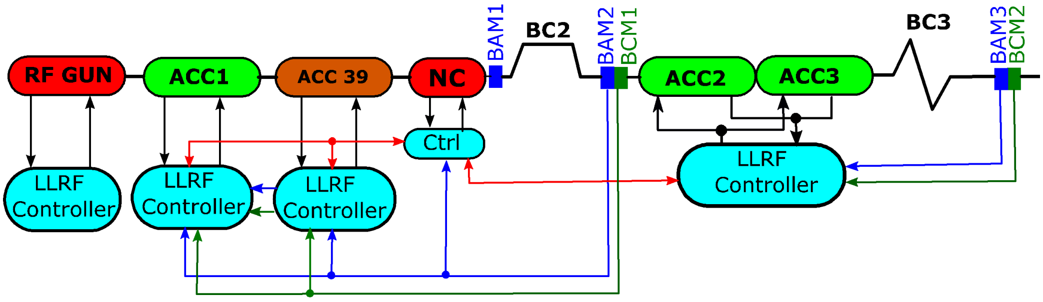

Figure 3.1: Place of installation the normal conducting cavity (NC) at FLASH. The low level RF (LLRF) controler systems are shown with blue boxes, ACC1, ACC2 and ACC3 are the accelerating components each of them are made from 8 TESLA cavity modules. BAM and BCM stand for bunch arrival time and bunch charge monitors, respectively. The magnetic bunch compressors (BC2 and BC3) are also shown.

3.2 Design process of the cavity

3.2.1 Cavity cells design

To design the fast feedback cavity, the arrival time deviation $\Delta t_A \approx \pm 150$ fs (peak-peak) needs to be corrected. This requires an energy correction of:

$$\Delta E = \frac{\Delta t_A \cdot c}{-R_{56}} \cdot E \approx \pm 37.5 \text{ keV}, \tag{3.1}$$

where c is the speed of light in free space, R_{56} is the bunch compressor parameter which is -0.18 m at bunch compressor BC2 of FLASH, and electron energy E of about 150 MeV. To achieve the required energy correction an accelerating voltage of $V_{acc} = \Delta E/e \approx 37.5$ kV is needed. Simulations show that a half band width of 400 - 500 kHz is sufficient for the arrival time regulation in the fs range. Also, to reduce the unwanted effects of the adjacent modes a system using the feedback and feed forward loops has been designed in the same way as the system that is discussed in section 2.2. According to the sampling rate of the designed system a difference of at least 9 MHz between the fundamental mode and its adjacent mode for the cavity is required. The difference between the fundamental mode and the other modes is better to be 27 MHz and 45 MHz, respectively. The required parameters for the four-cell normal conducting cavity are summarized in Table 3.1. In addition to these requirements the maximum of the electric field inside the cells should be equal. In addition to the reasons that are explained in section 2.2.2, there is another reason for this cavity to have flat-top on-axis peak electric field. Considering the maxima of the amplitude of the electric field inside the cells called E_1, E_2, E_3 and E_4, the dissipated power inside the cavity walls, P_{cav}, would be proportional to $E_1^2+E_2^2+E_3^2+E_4^2$, while the accelerating voltage of the cavity, V_{acc}, is proportional to $E_1+E_2+E_3+E_4$. It is easy to show that for a given dissipated power, the accelerating voltage would be maximum if $E_1=E_2=E_3=E_4$. Since our input power is limited, to achieve the maximum available accelerating voltage, we need to have equal electric field inside the cells. To have a quantitative view of this effect, we consider a simple case of two cells with non-equal electric fields of E_1 and E_2. If the average value of E_1 and E_2 is E, one can write:

$$E_1=E(1-\varepsilon), E_2=E(1+\varepsilon), \tag{3.2}$$

now one can find the relation for the dissipated power, P'_{cav}:

$$P'_{cav} \propto E_1^2+E_2^2=E\left\{(1-\varepsilon)^2+(1+\varepsilon)^2\right\}=2E\left(1+\varepsilon^2\right) \quad , \tag{3.3}$$

when the electric field of the cells are equal, the dissipated power would be proportional to $2E^2$. In the case of non-equal electric fields therefore, to have the same accelerating voltage we need to increase our input power by factor of $\left(1+\varepsilon^2\right)$. We know that the accelerating voltage is proportional to $\sqrt{P_{cav}}$ (see equation (3.6)). For a constant input power therefore the ratio of the accelerating voltages in two cases would be:

$$\frac{V_{acc'}}{V_{acc}} \approx 1+\frac{\varepsilon^2}{2} \quad , \tag{3.4}$$

here we used $\sqrt{1+\varepsilon^2} \approx 1+\varepsilon^2/2$ approximation since ε^2 is a small variable. If we want to correct 150 fs arrival time jitter that means operating with the maximum power, the above change in the accelerating voltage leads to an arrival time error of (based on equation (3.1)):

$$\Delta t = 150 \cdot \frac{\varepsilon^2}{2} \quad . \tag{3.5}$$

Based on the above discussion, if we wand to have a maximum of 1 fs arrival time jitter, the maximum tolerable difference between the electric field peaks inside the cells would be 15%.

Table 3.1: Required parameters of the cavity

V_{acc}	$f_{1/2}$	$f_\pi - f_{2\pi/3}$	$f_\pi - f_{\pi/3}$	$f_\pi - f_0$
37.5 kV	500 kHz	9 MHz	27 MHz	45 MHz

The designed cavity is formed from four coupled pillbox cavities and it has therefore four fundamental TM_{010} normal modes which are named as 0-mode, $\frac{\pi}{3}$-mode, $2\pi/3$-mode, and π-mode [1, 43]. These names are based on the phase shifts between adjacent cells. The operating mode is the π-mode because of its higher phase velocity. An isometric view of the designed cavity is displayed in Figure 3.2 while Figure 3.3 shows the cross sectional view of this cavity. The cooling part and the tuning knobs are also shown in this figures. In these figures and all other figures of the cavity the electrons' flight direction is from left to right.

The same design process as for the REGAE buncher discussed in section 2.2 applied to achieve the required mode separation. One can change the coupling between the cells by varying the physical parameters of the cavity, especially the thickness of the disks between the cells as well as the iris radii. Then, to make the electric field pattern smooth and adjust the resonant frequency of the operating mode, we changed the diameters of the cells.

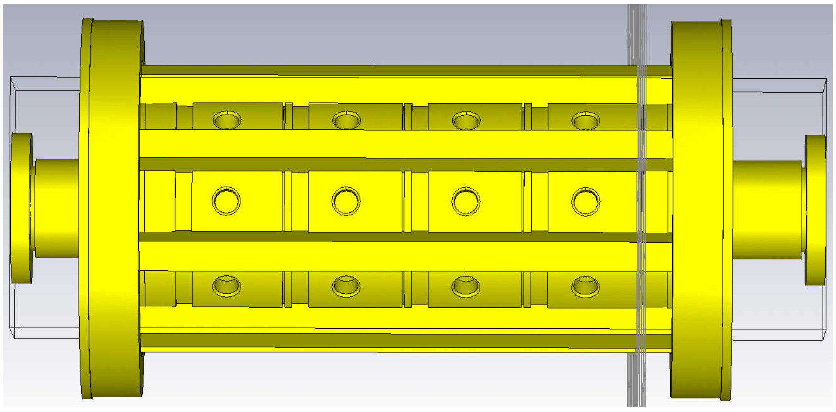

Figure 3.2: Isometric view of the designed cavity

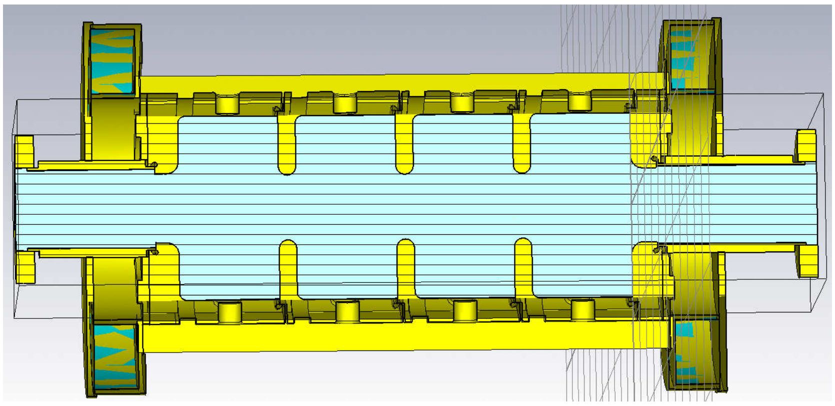

Figure 3.3: Cross sectional view of the designed cavity

3.2.2 Input coupler design

After designing the cells of the cavity, the most important part is to design its input coupler. As mentioned, it is required to increase the bandwidth of the cavity [43]. Simulations show that for a normal conducting pillbox cavity made from copper and operating at 3 GHz frequency, the unloaded quality factor Q_0 is about 16000 while 500 kHz half bandwidth requires a loaded quality factor of 3000. Therefore the best way is to decrease the external quality factor. By changing the coupling constant between the cavity and its coupler one can change the external quality factor and subsequently the band with of the cavity. However, by changing the coupling constant the accelerating voltage also varies. For a cavity with the effective shunt impedance of r, input power of P_{in}, and the coupling constant of β the accelerating voltage can be written as [1]:

$$V_{acc} = \sqrt{P_{in} r}\frac{2\beta^{1/2}}{1+\beta} \quad . \tag{3.6}$$

On the other hand the half bandwidth of a cavity can be written as a function of the resonant frequency, the quality factor, and the coupling constant [43]:

$$f_{1/2} = \frac{f_0}{2Q_L} = (1+\beta)\frac{f_0}{2Q_0} \quad , \tag{3.7}$$

where f_0 is the resonant frequency, Q_L is the loaded quality factor and Q_0 is the unloaded quality factor of the cavity. For the designed cavity the unloaded quality factor is about 16000 and the effective shunt impedance is about 8 MΩ. If we consider the input power of the cavity to be 890 W peak which is equal to the output of the amplifier that is going to supply the input power of the cavity, the accelerating voltage and the bandwidth of the cavity are shown in Figure 3.4 as a function of the coupling constant.

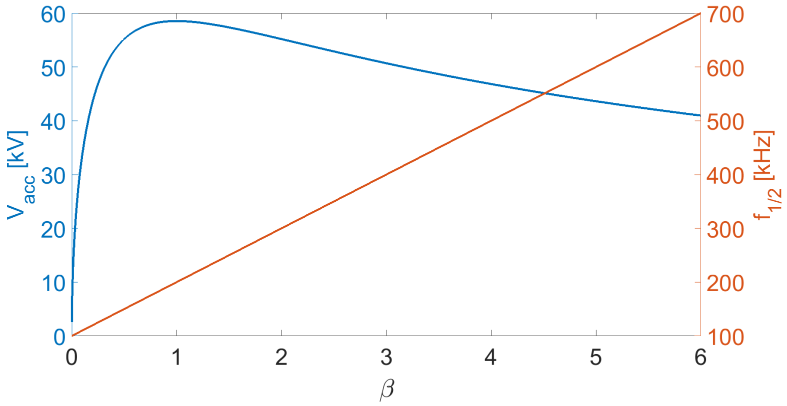

Figure 3.4: Influence of the coupling constant on the accelerating voltage and on the band width

As it can be seen in Figure 3.4 there is a trade-off between the accelerating voltage and the bandwidth of the cavity. From the accelerating voltage point of view the optimum value for coupling constant is the critical coupling where β is one and there is no power reflected from the cavity to the coupler. On the other hand to increase the bandwidth one should make β as large as possible. According to the desired values for the accelerating voltage and the bandwidth, adjusting the coupling constant to a value between 3.5 and 4.5 seems to be the best choice.
As it was declared in the previous section a side coupling is required for the cavity. Hence, it is necessary to use a 3D simulation program. CST Microwave Studio is used for this purpose [30]. In order to inject the desired power to the cavity via loop coupling a coaxial feedthrough is going to be used. An isometric and a cross sectional view of this feedthrough are shown in Figure 3.5. As it is displayed in this figure the two parts of the feedthrough are separated from each other by a ceramic material (the green colored part of the cross sectional view) while the inner and outer conductors are made from stainless steel.

This feedthrough should be installed on the body of one of the first cell of the cavity as shown in Figure 3.6. The input power is coupled to the cavity using a loop which actually excites a magnetic dipole inside the cavity [44]. The magnitude of this dipole is proportional to the area of the loop and also to the input power of the feedthrough and the amplitude of the mode that it excites is proportional to the scalar product between the magnetic dipole moment of the loop ($\vec{M}$) and the magnetic field of the corresponding mode inside the loop ($\vec{B}$) [45]:

$$|E| \propto \vec{M} \cdot \vec{B} \quad . \tag{3.8}$$

Based on the above equation one can vary the coupling constant by changing

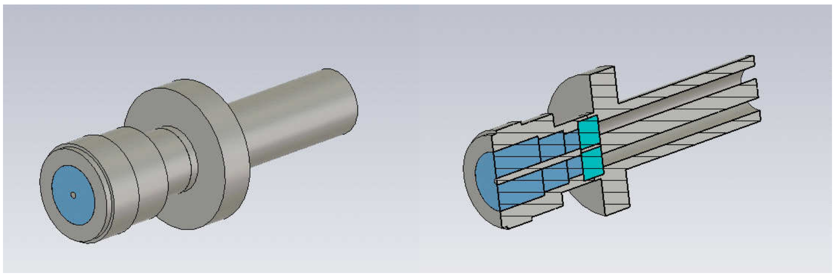

Figure 3.5: Isometric and cross sectional view of the feedthrough which is used to couple the input power

the loop orientation. This can be another advantage of using loop coupling instead of a waveguide coupler. Figure 3.6 shows the designed loop attached to the cavity. One can change the coupling constant between the coupler and the cavity by changing the area of the loop (changing $\vec{M}$), moving it up or down (changing $\vec{B}$) or even by changing its orientation (changing the angle between $\vec{M}$ and $\vec{B}$).

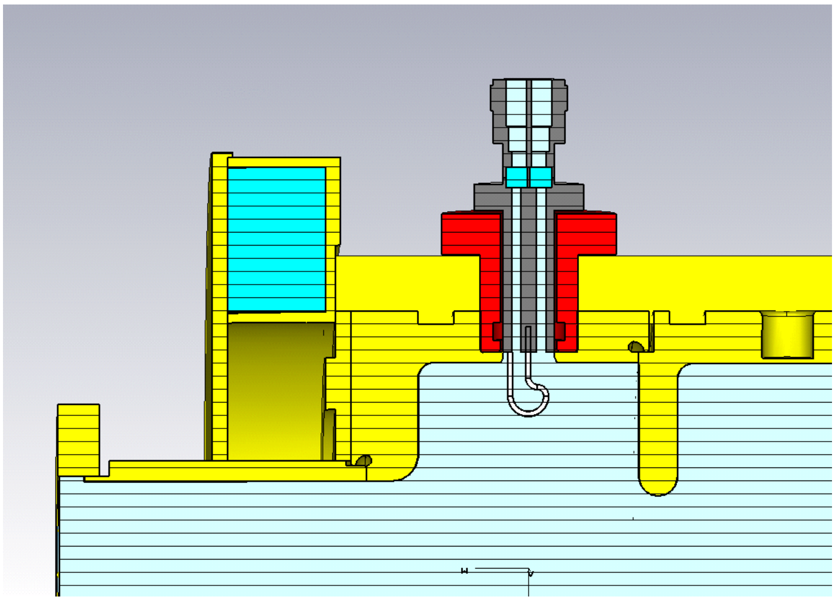

Figure 3.6: Cross sectional view of the input loop inside the cavity

Based on the simulation results it is difficult to achieve a high coupling constant (more than 3) with only one loop. For more explanation one should go deeper to what occurs during the excitation of a cavity. If there is a current density inside a cavity it will excite all the modes of the cavity. The modes of which the cut off frequency is lower than the excitation frequency can remain inside the cavity and the other modes will be evanescent modes which only store imaginary power in the space near the current density [36, 32]. According to the reciprocity theorem the amplitude of the excited field of each mode is proportional to the strength of the electric field of the mode in the place of the current. This excitation can be found as [32]:

$$e_n = -j\omega_n\mu_0 \frac{\int_V J(r)\cdot E(r)dV}{k_n^2 - k_0^2(1+\frac{1-j}{Q_n})} \quad , \tag{3.9}$$

where ω_n , k_n and Q_n are the angular frequency and wave number and the quality factor of the excited mode, respectively, k_0 is the wave number of the free space which is equal to $\sqrt{\varepsilon_0\mu_0}$. $J(r)$ is the current density which effect is going to be investigated and $E(r)$ is the electric field of the mode. The integration is taken over the volume of the current distribution. In our case the length of the loop is comparable with the wavelength of the input signal. Hence, it is not correct to assume a constant current for the loop. The best assumption for the loop current would be a sinusoidal distribution alike standing wave distribution [32]. Using this assumption and also the distribution of the electric field for the TM_{010} mode in a pillbox cavity one can calculate the amplitude of the excited field as a function of the loop radius and also its position inside the cavity. Afterwards it is possible to calculate the input impedance of the loop and consequently the coupling constant between the loop and the cavity. Figure 3.8 shows the calculation results for the coupling constant as a function of the loop depth and its length (parameters are defined in Figure 3.7). One can compare these results with the simulation results for the coupling constant in Figure 3.9. Both results illustrate the fact that it is not possible to increase the coupling constant above 3.

The solution to this problem is using two loops opposite to each other. This design would also be better because of the improved symmetry of the cavity, that means the more symmetric pattern of the electric and magnetic field inside the first cell. Figure 3.10 shows the input loops of the cavity. In this figure two other feedthroughs which are connected to smaller loops are also shown. These loops function as pick-up to measure the electric field inside the cavity.

The final design dimensions of the cavity parameters defined in Figures 2.4 and 2.14 are shown in Table 3.2.

3.2.3 Simulation results

The Eigenmode simulation is performed using CST Microwave Studio. Table3.3 summarizes the simulation results.

According to this table one can calculate the coupling constant:

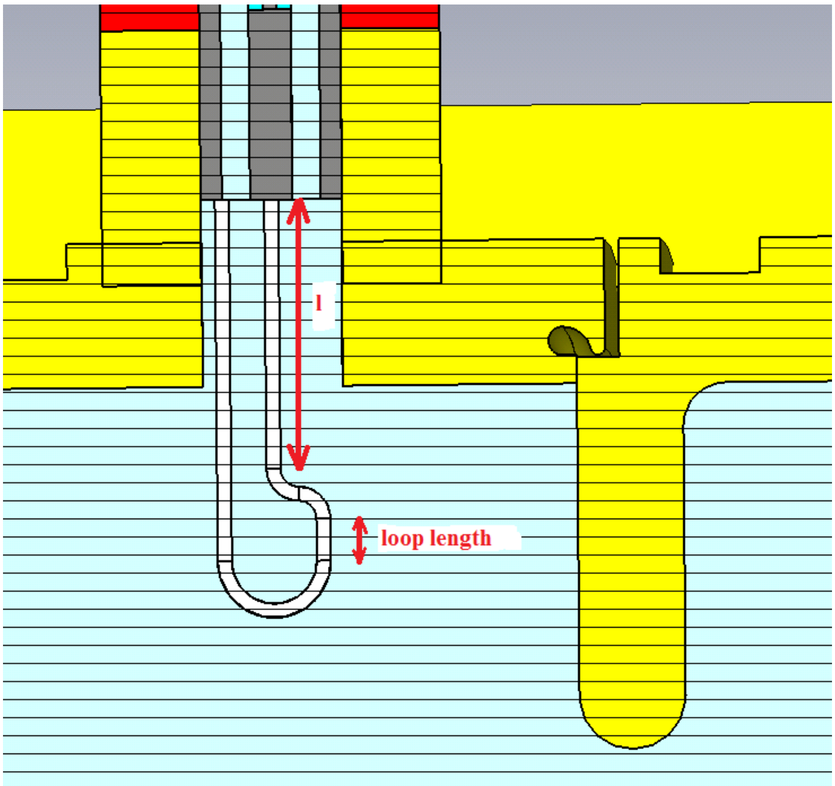

Figure 3.7: loop length and loop depth (l) definition

Table 3.2: Design values of the cavity parameters

Parameter	Design Value (mm)		Parameter	Design Value (mm)
rA	3.75		rB	3.75
rC	3.75		rD	5
rE	5		yA	14
yB	14		yC	14
yD	17		yE	17
hA	39.98		hB	39.82
hC	39.80		hD	40.04

$$\beta = \frac{Q_0}{Q_{ext}} \approx 4.1 \quad . \tag{3.10}$$

In order to calculate the accelerating voltage when the input power is 890 W, one can follow these steps:

The Eigenmode solver of CST Microwave studio always calculate the results assuming 1 Joule of the stored energy, considering the unloaded quality factor of

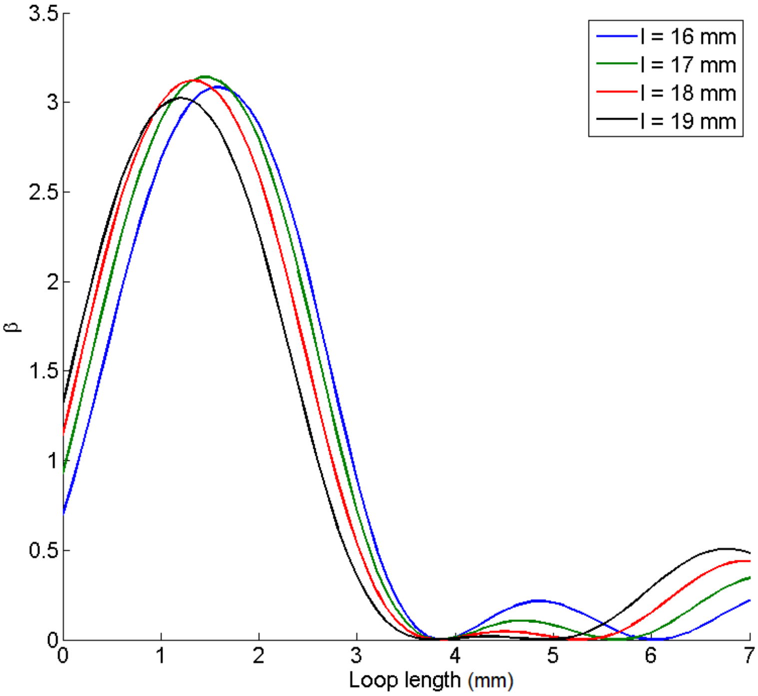

Figure 3.8: Calculation results for coupling constant as a function of loop length and its depth

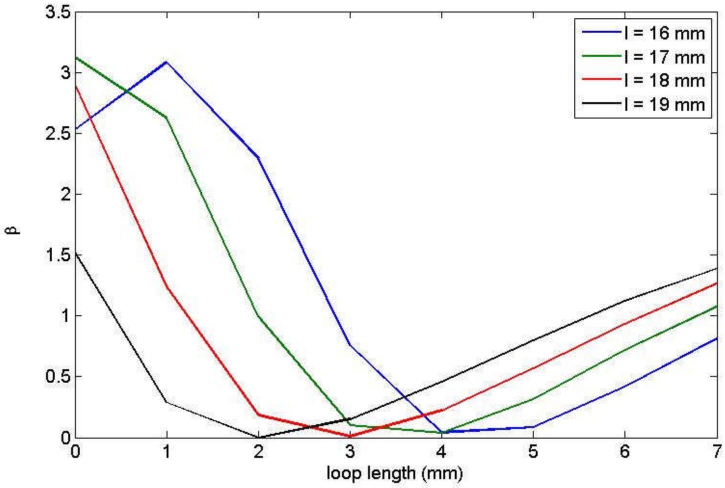

Figure 3.9: Simuilation results for coupling constant as a function of loop length and its depth

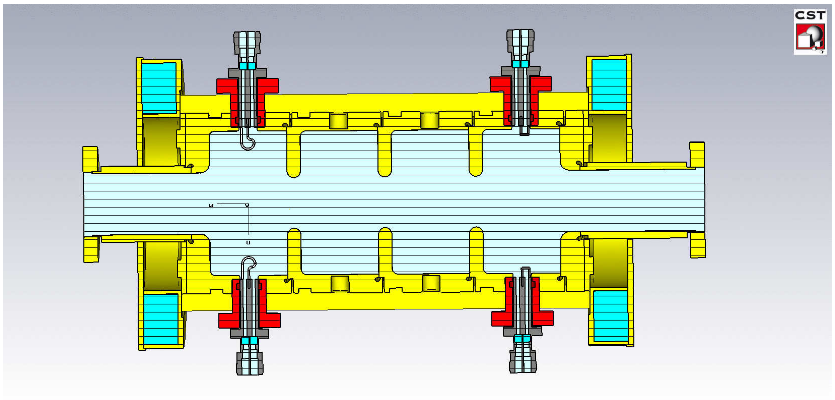

Figure 3.10: Cross sectional view of two input loops as well as two pick-up loops inside the cavity

Table 3.3: CST simulation results for the designed cavity

Parameter	**Simulation result value**
π-mode frequency	2998 MHz
$\frac{2\pi}{3}$-mode frequency	2989 MHz
$\frac{\pi}{3}$-mode frequency	2971 MHz
0-mode frequency	2954 MHz
unloaded quality factor Q_0	16000
external quality factor Q_{ext}	3900
loaded quality factor Q_L	3100
R/Q	500
shunt impedance r	7.7 MΩ
Accelerating Voltage (for 1 Joule stored energy)	3.03 MV

16000 the dissipated power in the cavity will be:

$$P_{cavity} = \frac{E_{stored}}{Q_0} \cdot \omega = \frac{1J}{16000} \cdot 2\pi \cdot 3 \cdot 10^9 s^{-1} = 1.18 \text{ MW} \quad . \tag{3.11}$$

and the reflected power from the cavity:

$$P_{ref} = \frac{\Gamma^2}{1-\Gamma^2} \cdot P_{cavity} \quad , \tag{3.12}$$

where Γ is the reflection coefficient which can be calculated from the coupling constant:

$$\Gamma = \frac{\beta - 1}{\beta + 1} \quad . \tag{3.13}$$

Substituting equation (3.13) into (3.12) results to:

$$P_{ref} = \frac{(\beta - 1)^2}{4\beta} \cdot P_{cavity} = 0.69 \text{ MW} \quad , \tag{3.14}$$

and the total power from the generator is:

$$P_{in} = P_{cavity} + P_{ref} = 1.87 \text{ MW} \quad . \tag{3.15}$$

For an average input power of 1.87 MW the accelerating voltage is 3.03 MV. Considering that the accelerating voltage is proportional to the square root of the input power, in the operating conditions when the average input power is 495 W (890 W peak to peak) the accelerating voltage will be:

$$V_{acc} = \sqrt{\frac{495}{1.87 \cdot 10^6}} \cdot 3.03 \cdot 10^6 = 49 \text{ kV} \quad , \tag{3.16}$$

and the half bandwidth of the designed cavity will be:

$$f_{1/2} = \frac{f_0}{2Q_L} = \frac{3 \cdot 10^9}{2 \cdot 3100} = 480 \text{ kHz} \quad , \tag{3.17}$$

which both satisfy the required values of table 3.1.
The electric field pattern on the axis of the cavity is also displayed in Figure 3.11 which shows a flat patters as we need for this cavity.

3.3 Wakefield simulation

As it is mentioned this cavity is designed to correct the arrival time of the bunches on the femtosecond level. Therefore it seems to be necessary to investigate the phenomena that can affect this precision. One of these phenomena is the wakefield. When a bunch of charged particles passes trough the cavity, it will excite the fundamental mode as well as the higher order modes of the cavity, so the bunch causes an electric field inside the cavity which is the sum of the different modes called wakefield [46]. The high frequency components of which the frequency is above the cutoff frequency of the beam pipe can propagate away along the beam pipe and do not remain localized [1]. But the low frequency modes, i.e. below the cutoff frequency of the pipe, remain localized and can affect the particles in the same bunch (short range wakefield) as well as the particles in the trailing bunch (long range wakefield).
To evaluate the wakefields, a parameter named loss factor is defined for each mode

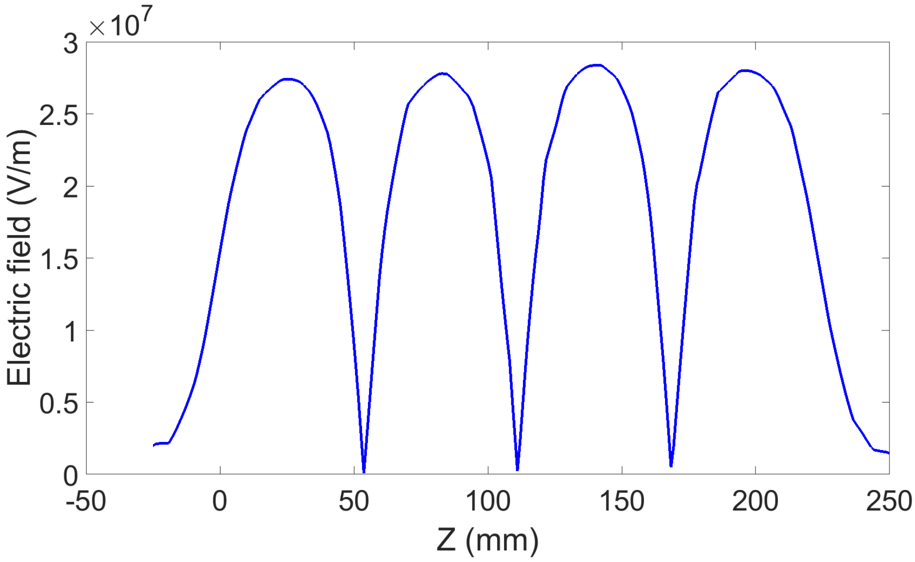

Figure 3.11: The electric field inside the cavity on the axis

of the cavity which determines the amplitude of the electric field that is excited by the beam [46]:

$$k_m = \frac{V_m^2}{4U_m} \quad , \tag{3.18}$$

where V_m is the voltage corresponding to mode m, and U_m is the stored energy in the electromagnetic field of this mode. The loss factor can be expressed as R/Q using [47]:

$$k_m = \frac{\omega_m}{4}\left(\frac{R}{Q}\right)_m \quad . \tag{3.19}$$

Each excited mode has a damping time given by the loaded quality factor of the mode. One can find the wakefield by summing the contribution of all individual modes. For example the longitudinal delta wake potential for distance s behind the bunch can be calculated from [48]:

$$W_{\parallel}^{\delta}(s) = \sum_m 2k_{\parallel_m}.cos\left(\omega_m \frac{s}{c}\right) \cdot exp\left(-\frac{\omega_m}{2Q_m}\frac{s}{c}\right) \quad , \tag{3.20}$$

where delta wake function means the wake potential caused by a charged particle with δ-function distribution. This delta function can be used as a Greens function to calculate the wake potential from any given charge distribution:

$$W_{\parallel}(s) = \int_0^{\infty} ds' \cdot \lambda(s-s') \cdot W_{\parallel}^{\delta}(s') \quad , \tag{3.21}$$

where $\lambda(s)$ is the charge distribution inside the bunch. It should be noted that in the above equation parameter s has a different meaning than in (3.20). In this equation one can select each arbitrary point as the origin of the coordinate system. By defining the coordinates of the charge distribution λ the wake potential will be automatically behind the bunch. The wake potential for a Gaussian bunch can be calculated as [47]:

$$W_{\|}(s) = \sum_{m} 2k_{\|_m} \cdot cos\left(\omega_m \frac{s}{c}\right) \cdot exp\left(-\frac{\omega_m}{2Q_m}\frac{s}{c}\right) \cdot exp\left(-\frac{1}{2}\left(\frac{\omega_m}{c}\right)^2 \sigma^2\right) \quad . \tag{3.22}$$

In this equation the index m indicates the modes with a longitudinal component of the electric field on the axis. For the modes with higher azimuthal order i.e. dipole, quadrupole etc. the loss factor depends on the offset of the exciting particle and they have no considerable longitudinal electric field component on the axis [32]. Hence the monopoles play a significant part in determination of the longitudinal wakefield. In the case of the cylindrical symmetry the voltage of the dipole modes depends linearly on the radial offset of the beam ($V_m \propto a$, where a is the radial offset). According to Equation (3.19), therefore the loss factor for these modes is proportional to the square of the bunch radial offset [46]. For the quadrupole modes the dependency of the loss factor on the radial offset is in the order of 4th power. It is worth to define the normalized transverse loss factor to calculate the normalized transverse wake potential [48]:

$$k_{\perp m}^{n} = \frac{V_m^2}{4U_m a^{2n}} \quad , \tag{3.23}$$

where superscript n determines the azimuthal order of the modes. (n=1, 2, 3, ... for dipole, quadrupole, sextuple etc.) It is obvious that $k_{\perp m}^{n}$ has the unit of V/cm^{2n}. The transverse delta wake potential of the modes with high azimuthal order normalized to the charge of the bunch can be expressed as:

$$W_{\perp}^{n\delta}(s) = \sum_{m} 2k_{\perp m}^{n} \cdot sin\left(\omega_m \frac{s}{c}\right) \cdot exp\left(-\frac{\omega_m}{2Q_m}\frac{s}{c}\right) \quad . \tag{3.24}$$

These wake potentials have the unit of $\frac{V}{C \cdot cm^{2n}}$ since they are normalized to the bunch charge and offset.

In order to evaluate the longitudinal and transverse wakefields for the designed cavity it is first necessary to determine the higher order modes, their frequency and their loss factors. Table 3.4 and 3.5 shows the CST Eigenmode solver results of the monopole and dipole HOMs for the designed cavity respectively. It should be noted again that monopole modes are the dominant modes in determining the longitudinal wakefield while the transverse wakefield is affected mostly by the

Table 3.4: Monopole modes of the designed cavity

freq. (MHz)	Q_L	**Loss factor**
2954	4016	9.0e7
2971	1570	1.5e8
2989	1226	5.6e9
2998	2950	2.3e12
4636	1022	1.2e5
4662	678	4.8e10
4670	358	4.6e11
5007	7781	6.9e9
5714	15081	2.8e5
5729	34333	2.9e4
5734	33380	1.1e4

dipole modes. Using Equation (3.22) one can calculate the longitudinal wakefield from the HOMs , shown in Figure 3.12.

On the other hand it is possible to simulate the longitudinal wakefield directly by CST Particle Studio [49]. Such simulation has been performed and the results are shown in Figure 3.13.

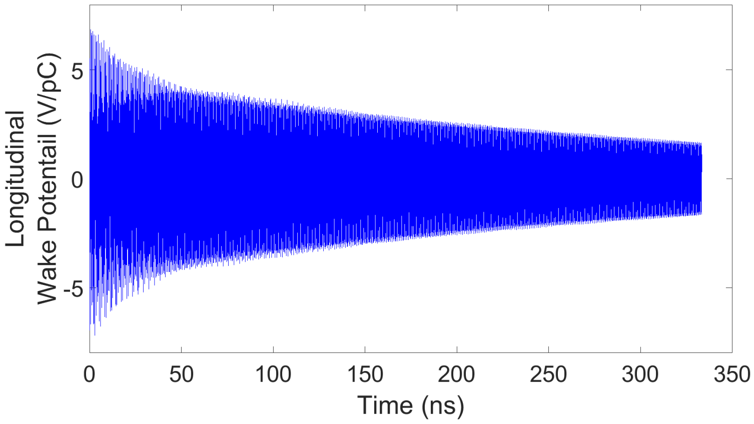

Figure 3.12: Longitudinal wakefield calculated from the HOMs

As it can be seen from these figures, the longitudinal wakefield inside the cavity is about 4 V/pC when 300 ns is elapsed after the first bunch, when the trailing bunch is arriving (with assumption of 3 MHz bunch frequency at FLASH). Therefore in a real assumption of the 1 nC charge of the bunch, the long range

Table 3.5: Dipole modes of the designed cavity

freq. (MHz)	Q_L	**Loss factor**		**freq. (MHz)**	Q_L	**Loss factor**
3734	424	2.6e5		5443	2524	5.1e5
3737	236	1.1e10		5445	13972	5.7e8
3777	15113	5.4e7		5549	1263	2.7e6
3794	196	2.4e4		5549	206	3.3e8
3861	16211	7.3e7		5626	8	4.0e8
3880	120	3.4e3		5627	251	6.8e5
3961	17870	7.3e8		5629	14613	1.8e8
3969	225	2.5e4		5692	7	2.3e5
4335	15078	4.4e8		5704	7030	3.4e5
4337	1928	1.4e3		5875	1609	1.4e4
4394	2031	2.1e5		5877	34563	1.3e4
4399	14950	2.6e8		6016	142	4.7e5
4470	995	1.5e5		6034	19333	2.7e7
4475	16923	2.7e9		6036	2600	1.9e5
4528	1802	6.1e4		6110	1719	1.5e6
4530	19146	2.9e9		6258	16811	2.4e5
4610	2852	1.6e4		6258	20106	3.6e5
5239	2719	1.0e6		6474	9170	4.5e5
5270	6955	8.8e5		6475	22471	3.8e7
5271	472	4.6e9		6670	423	4.7e9
5337	1530	6.4e5		6670	5788	3.4e6
5339	13124	3.6e9				

longitudinal wakefield will be 4 kV. This wakefield can change the arrival time of the bunch by 15 fs which is not acceptable considering the desired femtosecond resolution.

Figure 3.14 shows the Fourier transform of the simulated wakefield which is called wake impedance [46]. This spectrum shows the frequencies which are involved in the wakefield and their amplitude. One can find in fact the HOMs frequencies and their loss factors from the wake impedance [47]. What is important in this spectrum is that the contribution of the fundamental mode in the wakefield is by far more than the other modes. This contribution of the beam in exciting the operating mode is called beam loading effect [1]. So by subtracting the beam loading effect, which is practically possible by using beam loading compensation methods [50, 51], one can find that part of the wakefield which is origined from the modes other than the fundamental mode and in other words the part of the wake potential which cannot be compensated. Figures 3.15 and 3.16 show the

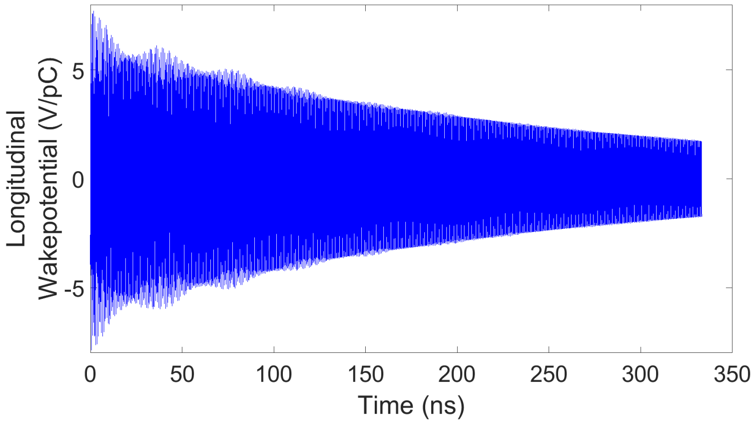

Figure 3.13: Longitudinal wakefield simulated with CST

mentioned wake potential calculated and simulated by CST respectively.

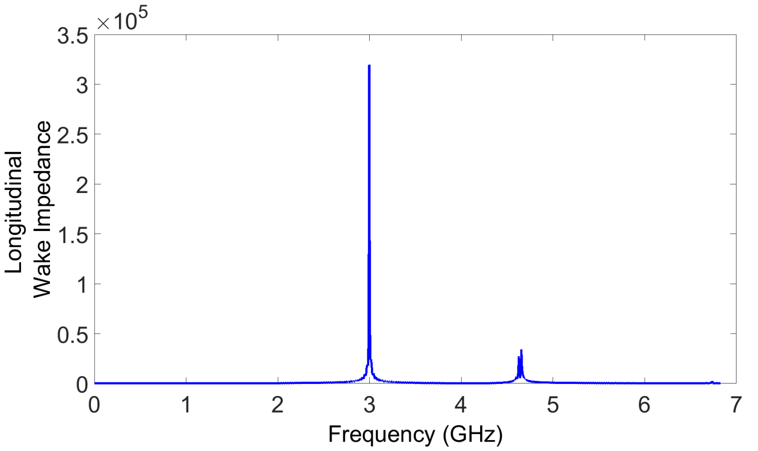

Figure 3.14: Wake impedance simulated with CST

As it can be seen from these figures the effect of the HOMs on the longitudinal wakefield of one bunch on the next bunch is less than 0.2 V/pC which means less than 1 fs error in arrival time of the bunch. Therefore it is sufficient to take into account the beam loading effect when the input power is going to be adjusted to the desired value.

The transverse wake potential calculated from the HOMs is also shown in Figure 3.17. The transverse wake potential of one bunch at the time that the next bunch enters the cavity (330 ns assuming 3 MHz, the maximum bunch repetition rate at FLASH) is 10^{-3} V/pC/mm^2. Considering the real values of 1 nC and 2 mm for the bunch charge and the radial offset, respectively the transverse wake potential

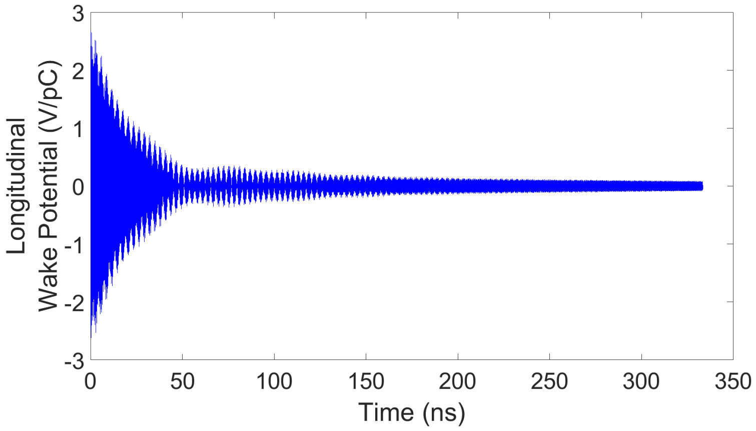

Figure 3.15: Longitudinal wakefield calculated from the HOMs when the fundamental mode is removed

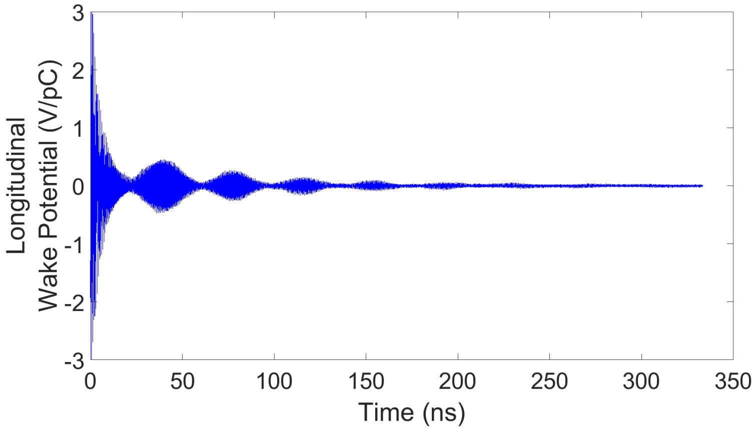

Figure 3.16: Longitudinal wakefield simulated with CST when the fundamental mode is removed

will be 4 V which is negligible [52].

3.4 Thermal simulation

One of the phenomena that might affect the precision of the cavity operation is increasing the temperature of different parts specially the coupler during the operation. Therefore in order to determine if it is feasible to use such feedthroughs to couple the power into the cavity, one should find the temperature distribution

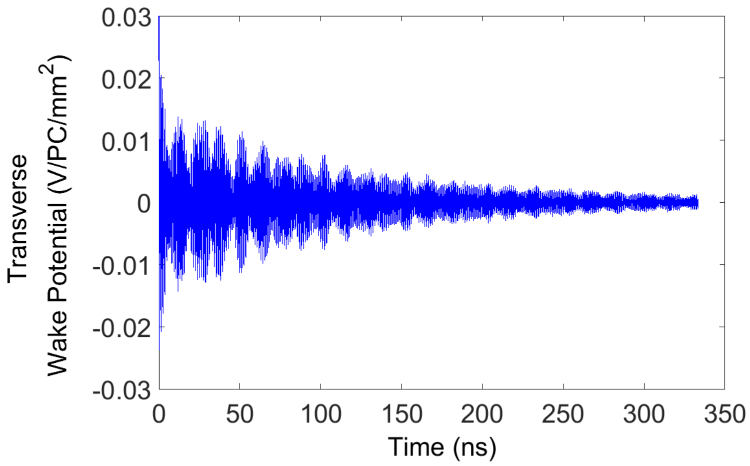

Figure 3.17: Transverse wakefield calculated from the HOMs

during the operation of the cavity. The electric and magnetic field inside the cavity and the thermal losses of different parts of the cavity and the coupler lead to a heat generation and consequently the temperature of different parts of the cavity increases. Thermal simulation can be operated using CST Mphysics Studio, the Thermal solver [53]. This solver uses the thermal losses which is calculated by CST Microwave Studio. Also one should define thermal surface properties of different parts i.e. their emissivities. Since the input power is pulsed with 890 W and 1% duty cycle, the power scaling factor should be adjusted to have a total power of 8.9 W. The cooling water is assumed as a perfect thermal conductor whose temperature is equal to the operation temperature. The simulated temperature of the different parts of the cavity is displayed in Figure 3.18 while Figure 3.19 shows the temperature of the feedthrough and the loop clearer. The operating temperature in this simulation is assumed to be 20°C. A higher operating temperature will not change the temperature distribution and just adds an offset to the temperature of all parts. As it can be observed the maximum temperature of the feedthrough is about 70°C which is completely tolerable for the feedthrough since according to its provider claims the upper limit for the operating temperature of this feedthrough is 300°C. One should note that the input power which is considered for this simulation is the maximum power that will be injected to the cavity in the worst case of the arrival time ±150 fs. Since in the real operation the arrival time jitter is not always the maximum, the input power and consequently the temperature of the feedthrough and its loop would be lower than the simulation value.

By increasing the temperature of the loop from 20 °C to 70 °C, because of thermal expansion the size of the loop will change slightly which changes the coupling constant from 4.13 at 20 °C to 4.11 at 70 °C. This leads to a change in accelerating voltage by maximum 50 V which is practically negligible.

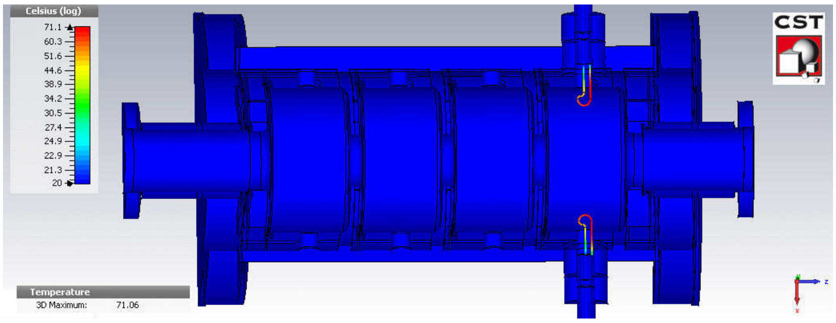

Figure 3.18: Temperature distribution of the cavity for 8.9 W average power.

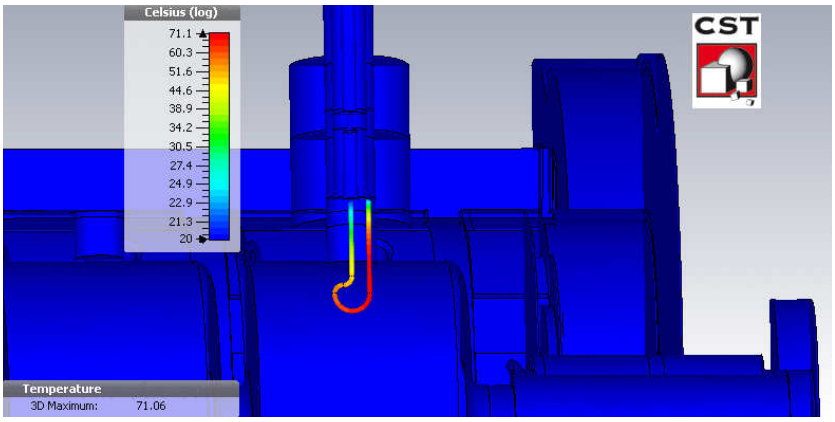

Figure 3.19: Temperature distribution of the loop and feedthrough

Figure 3.20 shows the temperature of the feedthrough and loop if only one loop is used to couple the input power to the cavity. In this situation the temperature of the loop may increase up to 200 °C which is not a secure value. Hence, thermal stability can be considered as another reason to use two loops instead of one input loop.

3.5 Multipacting simulation

When a cavity is filled by electromagnetic fields the electrons which are driven from the cavity walls can absorb energy from these fields which is called electron

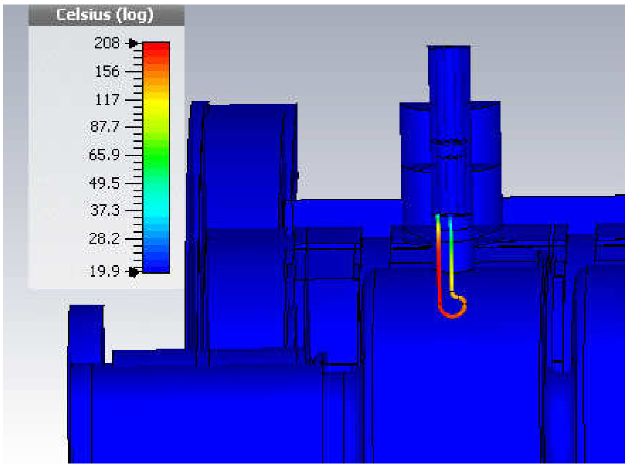

Figure 3.20: Temperature distribution of the loop and feedthrough when one loop is used

loading [1]. Electron loading causes some unwanted effects one of which is multipacting. Multipacting raises from the secondary electrons which are generated by the first electron when it collides with the cavity walls. If the average number of the secondary electrons is more than one and also if the direction of the electric field changes after the collision the secondary electrons will fly towards the opposite wall and will generate more electrons in turn. This process will continue until it is limited by the space charge of the electrons. This phenomenon is called multipacting [54]. Both kinematic and physical conditions are necessary to have multipacting. In other words the electric field direction should change when the first electron reaches one wall and also the number of the secondary electrons should be more than one. Generally multipacting occurs in lower electric fields. For example it is more likely to have multipacting during the filling of a cavity in comparison with the situation when steady state is reached [54]. For the designed cavity hence it is worth to evaluate the multipacting possibility since the electric fields are not too high inside the cavity. Such simulation can be performed using CST Particle Studio. For this purpose the metallic walls are introduced as the potential particle sources. Then the electric field distribution from the Eigenmode solver is defined as the electric field. A particle tracking solver simulates the trajectory of 10000 initial electrons inside the cavity. If the number of these electrons increases by time it shows that multipacting occurs.

The simulation has been performed for the designed cavity at different levels of the input power which result is shown in Figure 3.21. As it is shown in this figure, multipacting will not occur for the designed cavity in the operating power range. However, it is clear from this figure that for lower values of the input power the number of the electrons decreases slower than for the higher powers. Figure. 3.22

shows the trajectory of the simulated particles. This figure can be used to determine the regions of the cavity in which multipacting is more likely i.e. the regions with more electron concentration. So it is better to pay more attention in cleaning such areas.

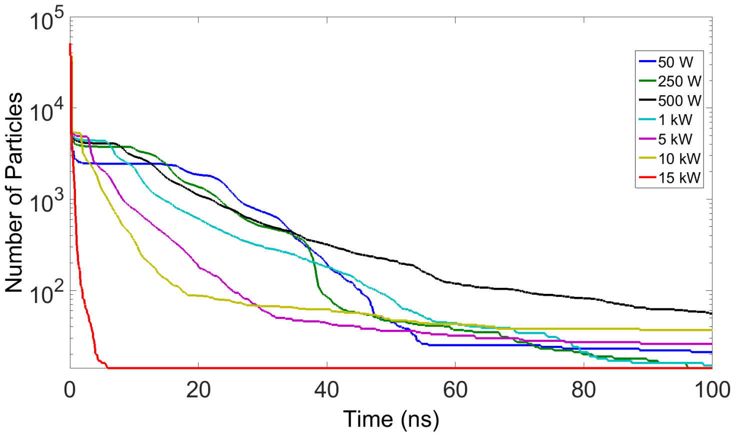

Figure 3.21: Number of the particles vs. time

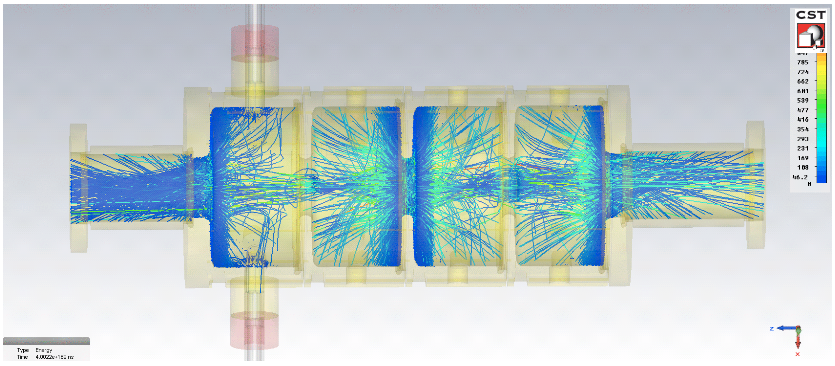

Figure 3.22: particles trajectory

3.6 Circuit models of the cavity

Generally, direct application of Maxwell's equation is a useful method to find the detailed information about the resonant frequency as well as the field distribution inside the cavity [32]. However, it is not simple to deal with these equation specially when it is required to take the generator and input couplers into account. As discussed in chapter 2 an easier way is to model the cavity, its generator and the coupling mechanism using an equivalent AC-circuit model. Since all the details of the system can be determined by solving Maxwell's equation which are all linear, it is possible to model it by a linear AC-circuit containing simple R, L and C elements.

In the first part of this section we focus on the coupling mechanism. Therefore, in this part the whole cavity is considered as a single resonator. As we will see the results help to find the optimum operation of the cavity. The second part is devoted to evaluate the coupling between the cells of the cavity in which each cell is modeled by a single resonance circuit in same way as the analysis that is proposed in the section 2.3 for the REGAE buncher. However the circuit is now more precise and its outstanding benefits in the tuning process of the cavity is introduced and verified by simulation.

3.6.1 Power Coupling Mechanism Modeling

Figure 3.23 shows the circuit model for the cavity, its input couplers and the generator. As it can be seen in this figure the generator is modeled by a current circuit with an input resistance of Z_0 which is connected to a coupling mechanism through a waveguide with characteristic impedance of Z_0. It is assumed that the generator is matched to the waveguide to set the reflected power from the waveguide to the generator to be zero. The input couplers are modeled by ideal transformers with turns ratio of 1:n_1 and 1:n_2 where n_i depend on the coupling between the cavity and the waveguide. The cavity itself is modeled by a RLC parallel circuit where $R = r_s/2$ is equal to half of its effective shunt impedance. It is more convenient to transform all the circuit elements to one side of the transformer according to ideal transformer rules as shown in Figure 3.24. The coupling constant β should be defined for the input couplers as a measure of the waveguide-to-cavity coupling strength. When the generator is switched on, a part of the stored energy inside the cavity will be radiated to the outside which will be dissipated in the output load that is actually the generator input impedance. We call this dissipated power P_{ext}. If the dissipated power inside the cavity (in the conducting walls) is P_{cav}, then the coupling constant β can be defined as [1]:

$$\beta \equiv \frac{P_{ext}}{P_{cav}} \quad . \tag{3.25}$$

According to the above definition and using the transformed circuit elements depicted in Figure 3.23, it is straightforward to show that the coupling constant can be written as $\beta_i = R/n_i^2 Z_0$.

Now we calculate the accelerating voltage of the cavity as a function of the input power and the coupling constants. We assume that the total input power is P_{in}

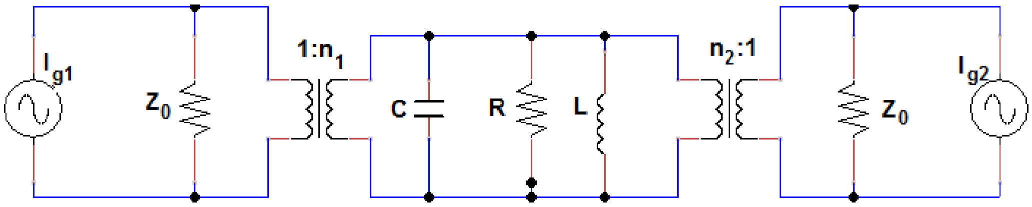

Figure 3.23: The equivalent circuit of the cavity and the coupling mechanism

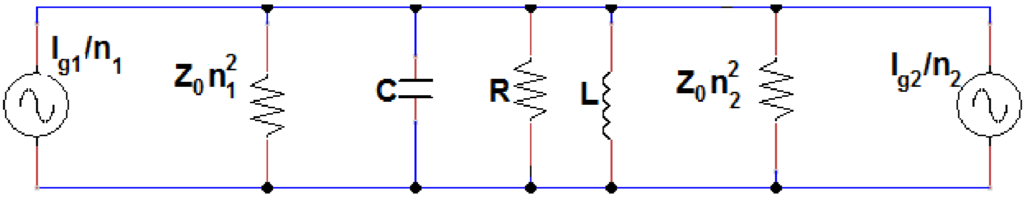

Figure 3.24: Equivalent circuit of the cavity transformed into the resonator circuit

which is divided to two parts P_1 and P_2 that are injected to the cavity via the first and second couplers respectively. It is more convenient to solve the circuit for each generator separately and then use superposition to find the total voltage of the cavity [55]. First we consider only the first generator, in this case the circuit can be shown as Figure 3.25. From the microwave theory we know that if a wave is emitted from the generator into the cavity the reflection coefficient caused by the cavity load impedance Z_L is [36]:

$$\Gamma = \frac{Z_L - Z_0}{Z_L + Z_0} \quad , \tag{3.26}$$

where Z_0 is the characteristic impedance of the waveguide between the cavity and the generator. In the situation displayed in Figure 3.25 the load impedance would be:

$$Z_L = R \| R/\beta_2 = \frac{R}{\beta_2 + 1} \quad , \tag{3.27}$$

and the reflection coefficient:

$$\Gamma = \frac{Z_L - Z_0 n_1^2}{Z_L + Z_0 n_1^2} = \frac{\frac{R}{\beta_2+1} - \frac{R}{\beta_1}}{\frac{R}{\beta_2+1} + \frac{R}{\beta_1}} = \frac{\beta_1 - \beta_2 - 1}{\beta_1 + \beta_2 + 1} \quad . \tag{3.28}$$

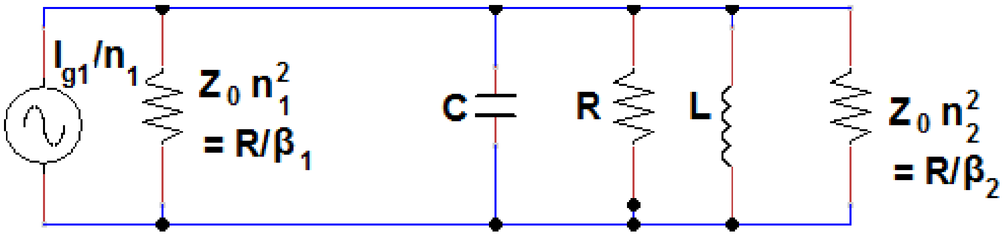

Figure 3.25: Equivalent circuit of the cavity transformed into the resonator circuit when only one generator is switched on

Hence, the transmitted power from the first generator inside the cavity will be:

$$P_T = P_1(1-\Gamma^2) = P_1\frac{4\beta_1(\beta_2+1)}{(\beta_1+\beta_2+1)^2} \quad . \tag{3.29}$$

A part of this power will be radiated from the cavity via the second coupler which value can be calculated using Equation (3.25). The power that will remain and dissipate inside the cavity can be calculated as:

$$P_{cav1} = \frac{P_T}{\beta_2+1} = P_1\frac{4\beta_1}{(\beta_1+\beta_2+1)^2} \quad , \tag{3.30}$$

and the voltage of the cavity:

$$V_1 = \sqrt{r_s P_{cav1}} = \sqrt{P_1 r_s}\frac{2\sqrt{\beta_1}}{\beta_1+\beta_2+1} \quad . \tag{3.31}$$

Therefore the total voltage of the cavity when both generators are considered can be calculated using superposition:

$$V = \sqrt{r_s}\frac{2\sqrt{P_1\beta_1}+2\sqrt{P_2\beta_2}}{\beta_1+\beta_2+1} \quad . \tag{3.32}$$

As it can be seen from Equation (3.32) the cavity voltage depends on the coupling constants of the input couplers. It can be shown that for a given input power of $P = P_1 + P_2$, the maximum cavity voltage is achievable when:

$$\frac{P_1}{P_2} = \frac{\beta_1}{\beta_2} \quad , \tag{3.33}$$

which is :

$$V_{max} = \sqrt{(P_1+P_2)\, r_s}\frac{2\sqrt{\beta_1+\beta_2}}{\beta_1+\beta_2+1} = \sqrt{P r_s}\frac{2\sqrt{\beta}}{\beta+1} \quad . \tag{3.34}$$

which is equal to the voltage when there is only one coupler with a coupling constant of β. The dependency of the cavity voltage on the coupling constants for a given input power is shown on Figure 3.26.

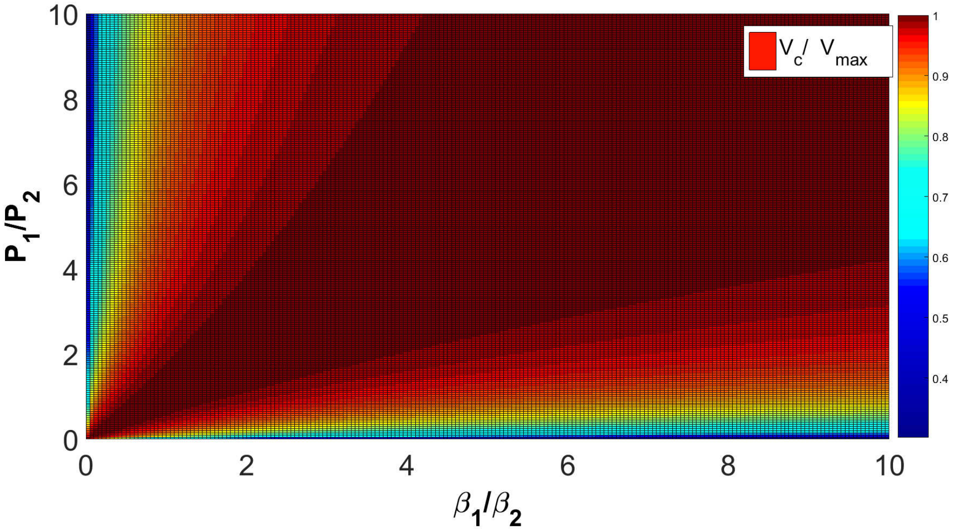

Figure 3.26: Ratio of the cavity voltage to the maximum achievable voltage for a given input power as a function of coupling constants and power division

3.6.2 cell to cell coupling modeling

In this section a circuit model for cell to cell coupling is investigated which can be used to understand the effects of the physical parameters of the cells and the irises on the coupling between the cells, mode separation etc. The proposed model is somehow similar to the model considered for the REGAE buncher with some modifications that make it more precise to be used. First such model is introduced and then the application of this model for tuning the cavity is studied.
The four cell normal conducting cavity is modeled by the circuit displayed if Figure 3.27. As it can be seen each cell is modeled by a parallel RLC resonator circuit and the coupling between the cells is modeled using a capacitor between the cells. The cell to cell coupling can also be modeled by using coupled inductances via their mutual inductance. Since the coupling between the cells is provided through the irises on the axis of the cavity where the electric field is maximum and the magnetic field is minimum, one expects to have electric coupling between the cells and therefore it is more realistic to consider capacitors as the coupler in the circuit model instead of inductors which introduce magnetic coupling [36, 1]. However if one uses mutual inductances to model the coupling between the cells

the final equations would be the same as the results of this model since the two considered circuits are dual [55].

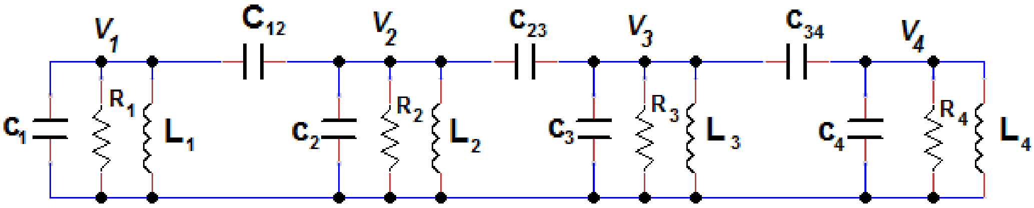

Figure 3.27: Circuit model of the cavity

To find the steady state solution of this circuit on can write four Kirchhoff's current law equations for each node:

$$\begin{aligned}
&V_1\left(\frac{1}{R_1}+\frac{1}{L_1 j\omega}+C_1 j\omega+C_{12} j\omega\right)-V_2 C_{12} j\omega=0,\\
&V_2\left(\frac{1}{R_2}+\frac{1}{L_2 j\omega}+C_2 j\omega+C_{12} j\omega+C_{23} j\omega\right)-V_1 C_{12} j\omega-V_3 C_{23} j\omega=0,\\
&V_3\left(\frac{1}{R_3}+\frac{1}{L_3 j\omega}+C_3 j\omega+C_{23} j\omega+C_{34} j\omega\right)-V_2 C_{23} j\omega-V_4 C_{34} j\omega=0,\\
&V_4\left(\frac{1}{R_4}+\frac{1}{L_4 j\omega}+C_4 j\omega+C_{34} j\omega\right)-V_3 C_{34} j\omega=0 \quad .
\end{aligned} \tag{3.35}$$

After some algebra the set of the equations given in (3.35) can be written as:

$$\begin{aligned}
&V_1\left(1-\frac{\omega_{01}^2}{\omega^2}-\frac{j\omega_{01}}{Q_1\omega}\right)-V_2 k_{12}=0,\\
&V_2\left(1-\frac{\omega_{02}^2}{\omega^2}-\frac{j\omega_{02}}{Q_2\omega}\right)-V_1 k_{21}-V_3 k_{23}=0,\\
&V_3\left(1-\frac{\omega_{03}^2}{\omega^2}-\frac{j\omega_{03}}{Q_3\omega}\right)-V_2 k_{32}-V_4 k_{34}=0,\\
&V_4\left(1-\frac{\omega_{04}^2}{\omega^2}-\frac{j\omega_{04}}{Q_4\omega}\right)-V_3 k_{43}=0,
\end{aligned} \tag{3.36}$$

where ω_{0n} and Q_n are the resonant frequencies and the quality factors of the individual resonators if they were uncoupled which are equal to $\frac{1}{\sqrt{L_n C_{neq}}}$ and $R_n C_{neq}\omega_{0n}$, respectively. Here C_{neq} means the equivalent capacitance of each cell when the other cells are assumed to be short circuit. C_{2eq} would be for instance $C_2+C_{12}+C_{23}$. Here ω is the assumed frequency of a steady-state oscillation (normal mode) and $k_{mn}=\frac{C_{mn}}{C_{meq}}$ are the coupling constants between the adjacent cells. It is more convenient to write the equation (3.36) as:

$$
\begin{aligned}
&V_1\left(\tfrac{1}{\omega_{01}^2}-\tfrac{1}{\omega^2}-\tfrac{j}{Q_1\omega\omega_{01}}\right)-V_2\tfrac{k_{12}}{\omega_{01}^2}=0,\\
&V_2\left(\tfrac{1}{\omega_{02}^2}-\tfrac{1}{\omega^2}-\tfrac{j}{Q_2\omega\omega_{02}}\right)-V_1\tfrac{k_{21}}{\omega_{02}^2}-V_3\tfrac{k_{23}}{\omega_{02}^2}=0,\\
&V_3\left(\tfrac{1}{\omega_{03}^2}-\tfrac{1}{\omega^2}-\tfrac{j}{Q_3\omega\omega_{03}}\right)-V_2\tfrac{k_{32}}{\omega_{03}^2}-V_4\tfrac{k_{34}}{\omega_{03}^2}=0,\\
&V_4\left(\tfrac{1}{\omega_{04}^2}-\tfrac{1}{\omega^2}-\tfrac{j}{Q_4\omega\omega_{04}}\right)-V_3\tfrac{k_{43}}{\omega_{04}^2}=0 \quad .
\end{aligned}
\tag{3.37}
$$

When some resonators are coupled to each other their coupling constants determine the mode separation of the whole system. The stronger the coupling between the cells the larger the difference between the adjacent modes. As an approximation when $k_{mn} \ll 1$, one can consider $\omega - \omega_{0n} \approx k_n\omega_{0n}$ where k_n is the average coupling constant between the $n-th$ cell with its neighbors. So the imaginary part of the above equation can be written for example in the first equation as:

$$
\frac{j}{Q_1\omega\omega_{01}} \approx \frac{j}{Q_1\omega_{01}^2(1+k_{12})} \approx \frac{j(1-k_{12})}{Q_1\omega_{01}^2} \quad . \tag{3.38}
$$

Hence, equations (3.37) can be approximated by:

$$
\begin{aligned}
&V_1\left(\tfrac{1}{\omega_{01}^2}-\tfrac{1}{\omega^2}-\tfrac{j(1-k_{12})}{Q_1\omega_{01}^2}\right)-V_2\tfrac{k_{12}}{\omega_{01}^2}=0,\\
&V_2\left(\tfrac{1}{\omega_{02}^2}-\tfrac{1}{\omega^2}-\tfrac{j(1-k_2)}{Q_2\omega_{02}^2}\right)-V_1\tfrac{k_{21}}{\omega_{02}^2}-V_3\tfrac{k_{23}}{\omega_{02}^2}=0,\\
&V_3\left(\tfrac{1}{\omega_{03}^2}-\tfrac{1}{\omega^2}-\tfrac{j(1-k_3)}{Q_3\omega_{03}^2}\right)-V_2\tfrac{k_{32}}{\omega_{03}^2}-V_4\tfrac{k_{34}}{\omega_{03}^2}=0,\\
&V_4\left(\tfrac{1}{\omega_{04}^2}-\tfrac{1}{\omega^2}-\tfrac{j(1-k_{43})}{Q_4\omega_{04}^2}\right)-V_3\tfrac{k_{43}}{\omega_{04}^2}=0,
\end{aligned}
\tag{3.39}
$$

where k_2 and k_3 are defined as $(k_{21}+k_{23})/2$ and $(k_{32}+k_{34})/2$, respectively. One can write equations (3.39) in the matrix form as:

$$
LV = \frac{1}{\omega^2}V \quad , \tag{3.40}
$$

where L is the circuit matrix:

$$
L = \begin{bmatrix}
\frac{1-j\frac{(1-k_{12})}{Q_1}}{\omega_{01}^2} & -\frac{k_{12}}{\omega_{01}^2} & 0 & 0 \\
-\frac{k_{21}}{\omega_{02}^2} & \frac{1-j\frac{(1-k_2)}{Q_2}}{\omega_{02}^2} & -\frac{k_{23}}{\omega_{02}^2} & 0 \\
0 & -\frac{k_{32}}{\omega_{03}^2} & \frac{1-j\frac{(1-k_3)}{Q_3}}{\omega_{03}^2} & -\frac{k_{34}}{\omega_{03}^2} \\
0 & 0 & -\frac{k_{43}}{\omega_{04}^2} & \frac{1-j\frac{(1-k_{43})}{Q_4}}{\omega_{04}^2}
\end{bmatrix} \quad , \tag{3.41}
$$

and V is the vector of the cell voltages:

$$V = \begin{bmatrix} V_1 \\ V_2 \\ V_3 \\ V_4 \end{bmatrix} \quad . \tag{3.42}$$

According to Equation (3.40) which is an eigenvalue equation, $\frac{1}{\omega^2}$ is the eigenvalue of matrix L. Since L is a 4×4 matrix, it has four eigenvalues which correspond to four normal modes of the cavity, i.e. 0-mode, $\pi/3$-mode, $2\pi/3$-mode, and π-mode. Hence, by calculating the four eigenvalues of the matrix L one can find the four TM_{010} normal mode frequencies of the cavity. In order to find the eigenvalues and consequently the resonant frequencies the following equation has to be solved:

$$det \begin{bmatrix} \frac{1-j\frac{(1-k_{12})}{Q_1}}{\omega_{01}^2} - \lambda & -\frac{k_{12}}{\omega_{01}^2} & 0 & 0 \\ -\frac{k_{21}}{\omega_{02}^2} & \frac{1-j\frac{(1-k_2)}{Q_2}}{\omega_{02}^2} - \lambda & -\frac{k_{23}}{\omega_{02}^2} & 0 \\ 0 & -\frac{k_{32}}{\omega_{03}^2} & \frac{1-j\frac{(1-k_3)}{Q_3}}{\omega_{03}^2} - \lambda & -\frac{k_{34}}{\omega_{03}^2} \\ 0 & 0 & -\frac{k_{43}}{\omega_{04}^2} & \frac{1-j\frac{(1-k_{43})}{Q_4}}{\omega_{04}^2} - \lambda \end{bmatrix} = 0. \tag{3.43}$$

with the resonant frequencies: $\omega = \frac{1}{\sqrt{\lambda}}$. Equation (3.43) can be solved numerically by MATLAB. Since L is a complex matrix its eigenvalues will be also complex and so one can write the angular frequency as $j\omega = \alpha + j\beta$ where β determines the resonant frequency as $f = 2\pi\beta$ while α represents the damping factor which rises from the ohmic losses to determine the quality factor of each mode [32]:

$$Q = \frac{\beta}{2\alpha} \quad . \tag{3.44}$$

By calculating the eigenvalues of the circuit matrix it is therefore possible to find the resonant frequencies as well as the quality factors of each mode. One of the most important parameters of the cavity, which should be considered for the application of the cavity and also during its tuning, is the electric field pattern inside the cells. The maximum electric field of the cells on their axis can be translated into the voltage of the cells in the circuit model which are actually the eigenvectors of the circuit matrix. It is therefore possible to calculate the ratio of the maxima of the electric field inside the cells based on the circuit model. By defining the ratio of the maxima of the electric fields in the cells as:

$$r_{21}=\frac{max|E_2|}{max|E_1|} \quad r_{31}=\frac{max|E_3|}{max|E_1|} \quad r_{41}=\frac{max|E_4|}{max|E_1|} \quad , \tag{3.45}$$

one can solve the following equations to find the above parameters:

$$\begin{bmatrix} \frac{1-j\frac{(1-k_{12})}{Q_1}}{\omega_{01}^2}-\frac{1}{\omega^2} & -\frac{k_{12}}{\omega_{01}^2} & 0 & 0 \\ -\frac{k_{21}}{\omega_{02}^2} & \frac{1-j\frac{(1-k_2)}{Q_2}}{\omega_{02}^2}-\frac{1}{\omega^2} & -\frac{k_{23}}{\omega_{02}^2} & 0 \\ 0 & -\frac{k_{32}}{\omega_{03}^2} & \frac{1-j\frac{(1-k_3)}{Q_3}}{\omega_{03}^2}-\frac{1}{\omega^2} & -\frac{k_{34}}{\omega_{03}^2} \\ 0 & 0 & -\frac{k_{43}}{\omega_{04}^2} & \frac{1-j\frac{(1-k_{43})}{Q_4}}{\omega_{04}^2}-\frac{1}{\omega^2} \end{bmatrix} \begin{bmatrix} 1 \\ r_{21} \\ r_{31} \\ r_{41} \end{bmatrix} = 0. \tag{3.46}$$

3.6.3 Using the circuit model for tuning of the cavity

One of the applications of the circuit model for the designed cavity is to predict its behavior after some small changes which occur during the tuning. To make it more clear, one should review the process of tuning such cavity. Since temperature variation causes the change in the normal mode frequencies of the cavity the aim of tuning is to adjust the π-mode frequency to its operating value which is 2998 MHz. First the cavity should be tuned in the laboratory at room temperature, in this situation the fundamental modes can be measured by a network analyzer. If the π-mode frequency is below or above the operating value the volume of the cavities should be increased or decreased respectively. Tuning is performed by making small changes in the shape of the lateral side of the cells by applying gentle strokes on the tuning knobs which are made on the outer side of the cavity. Such knobs are shown in Figure 3.28. But the main question is: “Which cell should be tuned?”. The answer to this question can be found by considering the electric fields inside the cells. As it is mentioned before the maximum amplitude of the electric field along the axis should be equal in the four cells. So in order to find the cell or the cells that should be tuned it is required to measure the electric field in the cells and then determine the target with the aim of making the electric field pattern as smooth as possible.

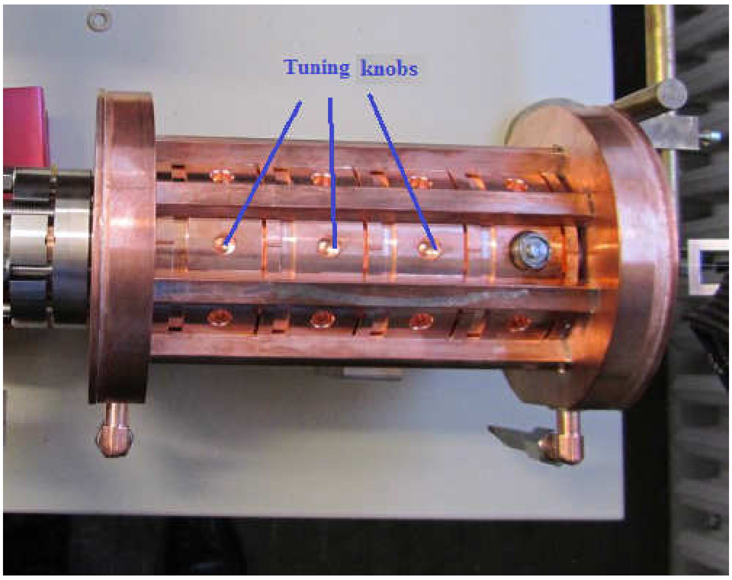

Figure 3.28: The tuning knobs of the REGAE buncher

At room temperature as long as the cavity is not connected to a vacuum system, it is possible to measure the electric field inside the cells by the bead pull method [56]. In the bead pull method a small bead connected to a string is moved along the axis of the cavity. The bead acts like a small perturbation and slightly changes the resonant frequency of the cavity proportional to the square of the local electric field [32]. However, this method is time consuming and tricky. Furthermore in the working regime the cavity will heat up by the RF power. If the temperature changes uniformly in all parts of the cavity the ratios of the electric fields will not vary. Of course such situation is not guaranteed and it is likely to have a non-homogeneous temperature distribution. In order to perform the tuning well, it is still required to know the electric field pattern inside the cavity to have a guideline for the tuning. In this situation there is no way to measure the electric field inside the cavity since it is connected to the beam pipe. So it will be useful if one can estimate the electric field pattern by means of the circuit model and its equations. Here the steps of tuning based on the circuit model estimations are explained:

First of all at room temperature one can measure the absolute values of the fundamental modes, their quality factor and also the ratio of the electric field inside the cells. From the mode frequencies and their quality factor one can find the complex angular frequency of each mode. As it is mentioned before, the angular frequencies and the ratios of the electric fields give us the eigenvalues and eigenvectors of the circuit matrix L, respectively. It is therefore possible to decompose the whole matrix L after these measurements. So the individual resonant frequencies of the resonators ω_{0n} and the coupling constants between them k_{mn} can be calculated from the elements of the circuit matrix considering equation (3.41). ω_{01} and k_{12} , and Q_1 for example can be calculated as follow:

$$\begin{aligned}
&k_{12} = \mathbf{Re}(\tfrac{L_{12}}{L_{11}}), \\
&Q_1 = \frac{1-k_{12}}{\mathbf{Im}(\frac{L_{12}}{L_{11}})k_{12}}, \\
&\omega_1 = \sqrt{\frac{k_{12}}{L_{12}}} \quad .
\end{aligned} \tag{3.47}$$

When the cavity is transferred from room temperature to the working regime or after tuning one or more cell, the circuit matrix will change. However if the nature of changes are considered deeply, it makes sense to assume variations only for the individual resonant frequencies. In fact we can consider that the coupling constant between the cavities and also the individual quality factors will not change by changing the temperature or by tuning one cell. So the new circuit matrix L' can be written as:

$$L' = \begin{bmatrix}
\frac{1-j\frac{(1-k_{12})}{Q_1}}{\omega_{01}'^2} & -\frac{k_{12}}{\omega_{01}'^2} & 0 & 0 \\
-\frac{k_{21}}{\omega_{02}'^2} & \frac{1-j\frac{(1-k_2)}{Q_2}}{\omega_{02}'^2} & -\frac{k_{23}}{\omega_{02}'^2} & 0 \\
0 & -\frac{k_{32}}{\omega_{03}'^2} & \frac{1-j\frac{(1-k_3)}{Q_3}}{\omega_{03}'^2} & -\frac{k_{34}}{\omega_{03}'^2} \\
0 & 0 & -\frac{k_{43}}{\omega_{04}'^2} & \frac{1-j\frac{(1-k_{43})}{Q_4}}{\omega_{04}'^2}
\end{bmatrix} , \tag{3.48}$$

where ω_{0n}' are the new values for the resonant frequencies of the cells. By defining α, β, γ and η as:

$$\alpha = \left(\frac{\omega_{01}}{\omega_{01}'}\right)^2 - 1, \quad \beta = \left(\frac{\omega_{02}}{\omega_{02}'}\right)^2 - 1, \quad \gamma = \left(\frac{\omega_{03}}{\omega_{03}'}\right)^2 - 1, \quad \eta = \left(\frac{\omega_{04}}{\omega_{04}'}\right)^2 - 1 \ , \tag{3.49}$$

one can rewrite equation (3.48) to:

$$L' = L + L^{(1)} \quad , \tag{3.50}$$

where:

$$L^{(1)} = \begin{bmatrix} \alpha\frac{1-j\frac{(1-k_{12})}{Q_1}}{\omega_{01}^2} & -\alpha\frac{k_{12}}{\omega_{01}^2} & 0 & 0 \\ -\beta\frac{k_{21}}{\omega_{02}^2} & \beta\frac{1-j\frac{(1-k_2)}{Q_2}}{\omega_{02}^2} & -\beta\frac{k_{23}}{\omega_{02}^2} & 0 \\ 0 & -\gamma\frac{k_{32}}{\omega_{03}^2} & \gamma\frac{1-j\frac{(1-k_3)}{Q_3}}{\omega_{03}^2} & -\gamma\frac{k_{34}}{\omega_{03}^2} \\ 0 & 0 & -\eta\frac{k_{43}}{\omega_{04}^2} & \eta\frac{1-j\frac{(1-k_{43})}{Q_4}}{\omega_{04}^2} \end{bmatrix} \quad . \tag{3.51}$$

So $L^{(1)}$ can be written as follow:

$$L^{(1)} = AL \quad , \tag{3.52}$$

where:

$$A = \begin{bmatrix} \alpha & 0 & 0 & 0 \\ 0 & \beta & 0 & 0 \\ 0 & 0 & \gamma & 0 \\ 0 & 0 & 0 & \eta \end{bmatrix} \quad . \tag{3.53}$$

According to (3.49) the diagonal elements of the matrix A are expected to be very small, $L^{(1)}$ is therefore a very small matrix compared to L and can be considered as a perturbation term in estimating the new eigenvalues. The eigenvalues of L' can be calculated in the first order perturbation theory. According to the perturbation theory if a perturbation term A^1 is added to a symmetric and positive definite matrix A the eigenvalues of the new matrix $A' = A + A^1$ can be estimated as [57]:

$$\lambda' = \lambda + V^T A^1 V \quad , \tag{3.54}$$

where V is the eigenvector of the unperturbed matrix. In our situation the circuit matrix L is not symmetric but we can consider it as sum of one symmetric (LS) and one asymmetric matrix (LAS) as:

$$L = LS + LAS \quad , \tag{3.55}$$

where:

$$LS = \begin{bmatrix} \frac{1-j\frac{(1-k_{12})}{Q_1}}{\omega_{01}^2} & -\frac{k_{12}}{2\omega_{01}^2} - \frac{k_{21}}{2\omega_{02}^2} & 0 & 0 \\ -\frac{k_{21}}{2\omega_{02}^2} - \frac{k_{12}}{\omega_{01}^2} & \frac{1-j\frac{(1-k_2)}{Q_2}}{\omega_{02}^2} & -\frac{k_{23}}{2\omega_{02}^2} - \frac{k_{32}}{2\omega_{03}^2} & 0 \\ 0 & -\frac{k_{32}}{2\omega_{03}^2} - \frac{k_{23}}{2\omega_{02}^2} & \frac{1-j\frac{(1-k_3)}{Q_3}}{\omega_{03}^2} & -\frac{k_{34}}{2\omega_{03}^2} - \frac{k_{43}}{2\omega_{04}^2} \\ 0 & 0 & -\frac{k_{43}}{2\omega_{04}^2} - \frac{k_{34}}{2\omega_{03}^2} & \frac{1-j\frac{(1-k_{43})}{Q_4}}{\omega_{04}^2} \end{bmatrix} , \tag{3.56}$$

and:

$$LAS = \begin{bmatrix} 0 & -\frac{k_{12}}{2\omega_{01}^2}+\frac{k_{21}}{2\omega_{02}^2} & 0 & 0 \\ -\frac{k_{21}}{2\omega_{02}^2}+\frac{k_{12}}{\omega_{01}^2} & 0 & -\frac{k_{23}}{2\omega_{02}^2}+\frac{k_{32}}{2\omega_{03}^2} & 0 \\ 0 & -\frac{k_{32}}{2\omega_{03}^2}+\frac{k_{23}}{2\omega_{02}^2} & 0 & -\frac{k_{34}}{2\omega_{03}^2}+\frac{k_{43}}{2\omega_{04}^2} \\ 0 & 0 & -\frac{k_{43}}{2\omega_{04}^2}+\frac{k_{34}}{2\omega_{03}^2} & 0 \end{bmatrix} \quad . \tag{3.57}$$

Since the coupling parameters are much smaller than the resonant frequencies the asymmetric matrix is a very small matrix and can be considered as a perturbation which is added to the symmetric matrix. The new network matrix after tuning therefore can be written as:

$$L' = L + L^{(1)} = LS + LAS + L^{(1)} = LS + LAS + A \cdot L \quad . \tag{3.58}$$

The eigenvalues of the new matrix using first order perturbation theory would be:

$$\begin{aligned} \lambda' &= \lambda S + VS^T \cdot (LAS + A \cdot L) \cdot VS \\ &= \lambda S + VS^T \cdot (LAS + A \cdot LS + A \cdot LAS) \cdot VS \\ &\approx \lambda S + VS^T \cdot (LAS + A \cdot LS) \cdot VS \\ &= \lambda S + Vs^T \cdot LAS \cdot VS + VS^T \cdot A \cdot LS \cdot VS \\ &= \lambda + \lambda S(VS^T \cdot A \cdot VS) \quad . \end{aligned} \tag{3.59}$$

where λS and VS are the eigenvalues and eigenvectors of the symmetric part of the network matrix. Considering the elements of VS one can write the final equation of equations (3.59) as follow:

$$\begin{aligned} \lambda_0' &= \lambda_0 + \lambda S_0 \left(V_{1_0}^2 \cdot \alpha + V_{2_0}^2 \cdot \beta + V_{3_0}^2 \cdot \gamma + V_{4_0}^2 \cdot \eta \right), \\ \lambda_{\frac{\pi}{3}}' &= \lambda_{\frac{\pi}{3}} + \lambda S_{\frac{\pi}{3}} \left(V_{1_{\frac{\pi}{3}}}^2 \cdot \alpha + V_{2_{\frac{\pi}{3}}}^2 \cdot \beta + V_{3_{\frac{\pi}{3}}}^2 \cdot \gamma + V_{4_{\frac{\pi}{3}}}^2 \cdot \eta \right), \\ \lambda_{\frac{2\pi}{3}}' &= \lambda_{\frac{2\pi}{3}} + \lambda S_{\frac{2\pi}{3}} \left(V_{1_{\frac{2\pi}{3}}}^2 \cdot \alpha + V_{2_{\frac{2\pi}{3}}}^2 \cdot \beta + V_{3_{\frac{2\pi}{3}}}^2 \cdot \gamma + V_{4_{\frac{2\pi}{3}}}^2 \cdot \eta \right), \\ \lambda_{\pi}' &= \lambda_{\pi} + \lambda S_{\pi} \left(V_{1_\pi}^2 \cdot \alpha + V_{2_\pi}^2 \cdot \beta + V_{3_\pi}^2 \cdot \gamma + V_{4_\pi}^2 \cdot \eta \right), \end{aligned} \tag{3.60}$$

which can be written as:

$$
\begin{aligned}
&\frac{\lambda_0'-\lambda_0}{\lambda S_0} = V_{1_0}^2 \cdot \alpha + V_{2_0}^2 . \beta + V_{3_0}^2 \cdot \gamma + V_{4_0}^2 \cdot \eta,\\
&\frac{\lambda_{\frac{\pi}{3}}'-\lambda_{\frac{\pi}{3}}}{\lambda S_{\frac{\pi}{3}}} = V_{1_{\frac{\pi}{3}}}^2 \cdot \alpha + V_{2_{\frac{\pi}{3}}}^2 \cdot \beta + V_{3_{\frac{\pi}{3}}}^2 \cdot \gamma + V_{4_{\frac{\pi}{3}}}^2 \cdot \eta,\\
&\frac{\lambda_{\frac{2\pi}{3}}'-\lambda_{\frac{2\pi}{3}}}{\lambda S_{\frac{2\pi}{3}}} = V_{1_{\frac{2\pi}{3}}}^2 \cdot \alpha + V_{2_{\frac{2\pi}{3}}}^2 \cdot \beta + V_{3_{\frac{2\pi}{3}}}^2 \cdot \gamma + V_{4_{\frac{2\pi}{3}}}^2 \cdot \eta,\\
&\frac{\lambda_\pi'-\lambda_\pi}{\lambda S_\pi} = V_{1_\pi}^2 \cdot \alpha + V_{2_\pi}^2 \cdot \beta + V_{3_\pi}^2 \cdot \gamma + V_{4_\pi}^2 \cdot \eta,
\end{aligned}
\tag{3.61}
$$

$$
\Rightarrow \begin{bmatrix} V_{1_0}^2 & V_{2_0}^2 & V_{3_0}^2 & V_{4_0}^2 \\ V_{1_{\frac{\pi}{3}}}^2 & V_{2_{\frac{\pi}{3}}}^2 & V_{3_{\frac{\pi}{3}}}^2 & V_{4_{\frac{\pi}{3}}}^2 \\ V_{1_{\frac{2\pi}{3}}}^2 & V_{2_{\frac{2\pi}{3}}}^2 & V_{3_{\frac{2\pi}{3}}}^2 & V_{4_{\frac{2\pi}{3}}}^2 \\ V_{1_\pi}^2 & V_{2_\pi}^2 & V_{3_\pi}^2 & V_{4_\pi}^2 \end{bmatrix} \begin{bmatrix} \alpha \\ \beta \\ \gamma \\ \eta \end{bmatrix} = \begin{bmatrix} \frac{\lambda_0'-\lambda_0}{\lambda S_0} \\ \frac{\lambda_{\frac{\pi}{3}}'-\lambda_{\frac{\pi}{3}}}{\lambda S_{\frac{\pi}{3}}} \\ \frac{\lambda_{\frac{2\pi}{3}}'-\lambda_{\frac{2\pi}{3}}}{\lambda S_{\frac{2\pi}{3}}} \\ \frac{\lambda_\pi'-\lambda_\pi}{\lambda S_\pi} \end{bmatrix} . \tag{3.62}
$$

Equation (3.62) can be easily solved to find the unknown parameters α, β, γ and η . After calculating these parameters all the elements of the new circuit matrix L' are determined and so the new ratios of the electric field in the cells can be calculated by solving the Equations (3.46). Hence, by determining the ratios of the electric field inside the cavities one can find the cell that should be tuned. After each tuning such calculation can be performed in order to find the new values. In fact the new results in each step should be considered as the old values for the next step. In each step it is required to measure just the four fundamental modes frequencies and their quality factors. By following the proposed algorithm then it is possible to calculate the ratios of the electric field inside the cells and consequently the cells that should be tuned can be determined.

3.6.4 Validation of the proposed method

In the previous section we introduced an algorithm to tune the cavity by employing the circuit model. In this section we try to investigate the usefulness of the proposed algorithm for tuning the cavity. For this purpose we can use CST Microwave Studio to simulate two tuning processes, one using the proposed method and the other without that. If the cavity is manufactured with the exact designed values its resonant frequency will be the design frequency. Of course because of manufacturing errors there will be some deviations from the designed value. because of such errors and also due to the simulation inaccuracy that might exist, the

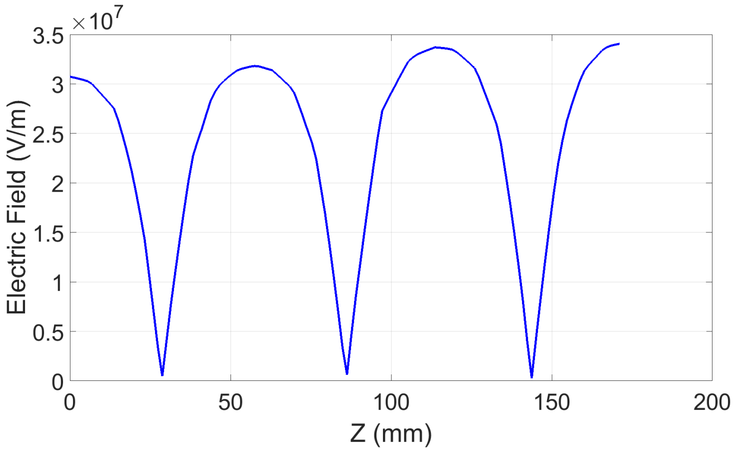

Figure 3.29: The electric field pattern inside the cavity after the modeled manufacturing and before tuning the cavity

resonant frequency of the designed cavity will be different from what we expect. It is therefore necessary to tune the cavity. We can generate random errors by considering the manufacturing tolerances which is 10 μm for the cells diameter. By adding the errors to the designed cavity one can model a manufactured cavity. The simulation results for this cavity shows a resonant frequency of 2995.6 MHz and electric field pattern of Figure 3.29.

Then we modeled the tuning process by CST. In the first tuning we used the proposed model to find the cell or the cells that should be tuned while in the second method we assumed that there is no information about the electric field pattern and hence we tune all the cells in each step. Furthermore the strikes on the cavity body is assumed to decrease the diameter of the cells which value is somehow a random amount in a reasonable range. Comparison of the electric field pattern inside the cells for the two tuned cavities is shown in Figure 3.30. The range of the vertical axis is adjusted in this figure so the difference between the two curves can be distinguished more easily. It is clear from this figure that by using the circuit model the tuning process can be fulfilled much more efficiently. As it can be seen, if we don't use the circuit model the electric field inside the cells would have a difference of more than 10% while by using the proposed model this difference will be less than 2%. Based on the discussion in section 3.1, 10% difference leads to abou 0.4 fs error while 2% causes an error of just 0.015 fs.

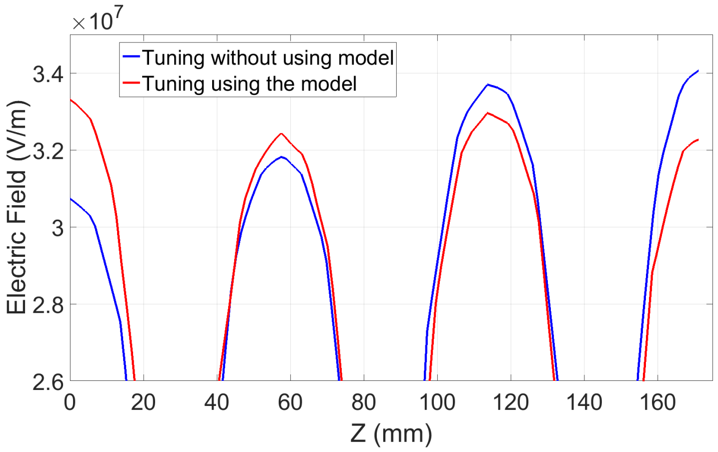

Figure 3.30: The electric field pattern inside the cavity after tuning with two methods

3.7 Summary and conclusion

A normal conducting cavity has been designed to correct the arrival time jitter of ± 150 fs at FLASH. This cavity acts as a fast actuator in a feed forward loop. In order to correct the mentioned jitter the designed cavity has to be able to provide an accelerating voltage of 37.5 kV and the half bandwidth between 400 and 500 kHz. A mode separation of 9 MHz between the operating mode and its adjacent mode was also needed. A solid-state amplifier provides the input power of the cavity which will be injected via a loop coupling mechanism that has been designed. Using loop coupling makes it possible to adjust the bandwidth of the cavity even after manufacturing and installing it. The simulation results show that the designed cavity fulfills all the required conditions. Furthermore wakefield, thermal and multipacting simulations have been perform to evaluate the operation efficiency of the designed cavity which show stable operation without negative effects of the longitudinal and transverse wakefields, thermal expansions and multipacting phenomenon. The input coupling mechanism as well as the cell to cell coupling have been modeled by electric circuits. Based on the proposed model a novel algorithm is introduced to be used to find the optimum operation of the cavity and also provide a guideline for the tuning process.

Chapter 4

Design of ultra-fast electron guns for AXSIS

4.1 Introduction

The advances in ultra-fast technologies in the past decades, led to the production of strong short pulse radiation which can reach the single-cycle duration with very strong peak fields. One can use such pulses in order to accelerate the particles engaging the advantages in terms of higher thresholds for material breakdown due to the short pulse duration and consequently introduce a promising path towards increasing the acceleration gradients. It is the general belief that the increase in the acceleration gradient augments the aptitude of the acceleration device in providing high quality bunches. The conventional accelerator technology is always based on either continuous wave or long pulse operation, where resonant or guiding structures are usually employed. In this chapter, we introduce novel structures for electron acceleration which operate based on single-cycle pulses named as ultra-fast guns. Inspired by the recent progresses in generating high power single cycle THz pulses, we consider the design of ultra-fast guns in the THz regime. The introduced guns are going to be used as the injector in the AXSIS project (Attosecond X-ray Science: Imaging and Spectroscopy). In this project a fully coherent attosecond X-ray will be provided and used for X-ray crystallography. Such crystallography provides 3D images of the structure of molecules ranging from small inorganic clusters to large protein complexes in atomic resolution [58]. Conventional particle accelerators consist of cascaded metallic or superconducting cavities or traveling wave tubes driven by high power electromagnetic fields in the microwave regime [1]. The electrical breakdown of metals puts a strong threshold for the accelerating fields which are typically 50-100 MV/m [59]. This fact is the major factor determining the maximum achievable level of the acceleration gradients in all the accelerator facilities like SLAC, CERN's compact linear collider (CLIC) and the design of the next linear collider (NLC) [60]. Moreover, it is the main problem hampering the development of compact devices based on relativistic particles. The small acceleration gradient dictates long accelerator lengths thereby calling the need for large research facilities to achieve high energy monochromatic electron beams. Consequently, the acceleration efficiency, both in terms of energy and cost, often suffers from the need for high energy levels to fill the cavities. Therefore, the desire to realize compact accelerators has spurred much research into the use of alternative acceleration schemes. As a result, advanced acceleration concepts, such as dielectric laser acceleration (DLA) [25], laser-driven plasma accelerators (LPA) [61], laser wake-field acceleration (LWFA), and THz acceleration are proposed and tested [62].

The empirical studies had initially shown that the electron field emission imposes a principal limit on the device operation. The electron field emission can be scaled as $f^{1/2}/\tau^{1/4}$ with f the operation frequency, and τ the pulse duration of the accelerating field, [59, 60, 63]. The above approximate scaling behavior justified the tendency towards higher frequency and ultra-fast schemes to achieve small accelerators. However, the recent study on largely gathered data from the breakdown threshold of various accelerators demonstrated that the dominant factor limiting the acceleration gradients is the pulse heating of the accelerator walls [64, 65]. This conclusion confirmed the lower operational gradients in the existing facilities compared with the predictions from the previously existing scaling laws. According to their conclusion, the pulse duration of the accelerating field plays the major role in the breakdown event. Therefore, focusing the efforts on efficient acceleration using short pulses opens new potentials to shrink down the size of such facilities.

During the past decades, the technologies for the generation of microwave and millimeter-waves, as used in conventional accelerators, have been very well developed for the production of continuous wave (CW) radiation. Therefore, the operating accelerators are mostly narrow-band devices functioning for a single frequency excitation. Examples are the widely used cascaded cavities which operate based on a resonance behavior and traveling wave accelerators in which fields of a guided mode are employed for acceleration. There is however a conceptual gap between the standard accelerator technology and the ultra-fast laser science. Hence, direct usage of a standard accelerator geometry excited by a short pulse laser incurs wasting a large portion of the input energy. Many of the efforts to achieve compact, or the so-called on-chip, accelerators will benefit considerably from new concepts to efficiently accelerate particles using ultra-short pulse lasers.

Although the optical acceleration of electrons seems very promising in terms of potentials for high acceleration gradients, the acceleration schemes based on optical pulses suffer from the difficulties caused by the short optical wavelengths.

As a rule of thumb, in order to prevent emittance growth and increased energy spread, the electron bunch length should correspond to no longer than 5 degrees of full optical cycle. This length at an IR wavelength of 2 mm corresponds to only 28 nm, which introduces strong limitations on the amount of charge per bunch accelerated by the optical excitation. If we consider for example a 0.4 nC bunch with the length of 30 μm (which are typical numbers for FLASH), one can scale down the charge of the bunch with the length of 28 nm which would be about 0.4 pC. Moreover, the necessary timing synchronization becomes more challenging with optical acceleration. The timing synchronization is usually done with optical laser pulses. Hence, the synchronization accuracy is limited to a fraction $(1/3-1/5)$ of an optical cycle, i.e. 0.5 fs - 1 fs. However, to achieve a proper synchronization for a 28 nm bunch size, one needs synchronization in the attosecond precisions. Recently, research efforts devoted to THz pulse generation have realized single-cycle pulse generation in the THz regime using optical rectification [66]. The achieved performance in this process has reached 1 % optical to THz conversion efficiency [67]. Considering that this source type uses a picosecond laser which functions more efficiently than a femtosecond laser by orders of magnitude, the overall efficiency of the THz acceleration with such short pulses becomes comparable to the optical acceleration. The benefit is then a longer wavelength and relaxed limitations in the amount of charge per bunch. Nonetheless, this scheme similarly demands ultra-fast accelerators.

The structures for accelerating particles using single-cycle THz pulses are discussed in this chapter. The designs can be scaled for cases with single-cycle (or even sub-cycle) optical pulses. In this concern, suitable materials which provide similar properties at the optical wavelengths, should be found and replaced. The considered temporal profile of the excitation is shown in Figure 4.1, which is common in all the cases. It is namely a single-cycle pulse described by:

$$f(t) = A_0 e^{-2ln2\frac{(t-t_0)^2}{\tau^2}} cos(\omega(t-t_0)+\phi_0) \quad , \tag{4.1}$$

where $A_0(x)$, $t_0 = x/c$, and $\phi_0 = \pm kx$ stand for the field amplitude, the time offset from the reference time, and the carrier envelope phase of the signal, respectively. All of these parameters are dependent on the spatial coordinate of the point where the field is probed. $\omega = 2\pi f_0$ denotes the angular frequency of the signal and $\tau = 1/f_0$ is the pulse duration of the single-cycle pulse.

4.2 High energy ultra-fast guns

One of the main limitations of the conventional normal conducting cavities is the field emission effect. Some recent experiments on cavities had measured values

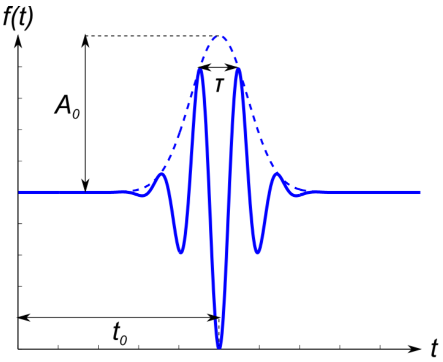

Figure 4.1: Temporal signature of a single cycle pulse considered as the excitation

of about 0.5 GV/m as the dark current threshold on some copper alloys [25]. This means that increasing the energy of the input THz beam to achieve higher acceleration rates is not a realistic method. Moreover, the today's THz generation technology has realized higher energy levels in the THz beams with constant improvement in both the generation efficiency and THz power. Consequently, a question is raised; how can one do an efficient acceleration using high energy short radiation pulses without surpassing the field emission threshold? Here, we try to answer this question by introducing structures which operate based on single-cycle THz beams with around 2 mJ energy at 300 GHz central frequency. First, suppose that this considered beam is focused down to one wavelength spot size. The direct calculation of the electric field in the Gaussian beam leads to 0.58 GV/m maximum field strength at the center of the pulse. An electron within this field can merely move 0.14 mm during the accelerating cycle, which is one-tenth of the operation wavelength. As a consequence, the electron very easily falls into the decelerating cycle and an inefficient acceleration will take place. This calculation demonstrates the necessity of developing a scheme in which the electron is influenced by the beam over a long path.

For the purpose of electron acceleration using high energy beams, two important points need to be looked at. First, the electron may gain relativistic energy, which intensifies the effect of the transverse magnetic field in the accelerating beam on the electron motion. This effect causes the electrons to leave the straight trajectory for acceleration. In other words, the electron travel path is deflected. Therefore, the designed gun should consider a setup in which the bunch is not deflected away from the aimed acceleration trajectory. Second, a high-energy THz beam should not be focused to small spot-sizes. Otherwise, the field emission threshold destroys the gun performance. Therefore, the operational spot size of the beam will be much larger than the distance an electron can travel in one half-

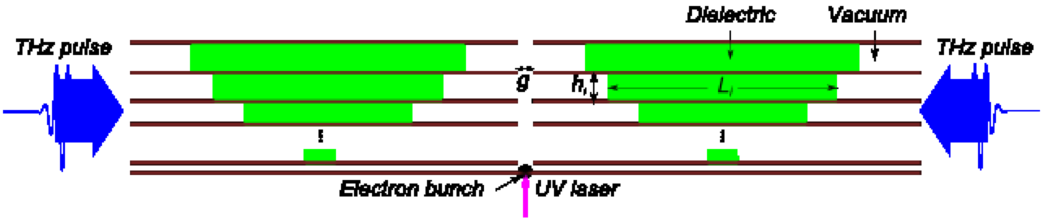

Figure 4.2: Not scaled schematic illustration of the multilayer gun operating based on high energy single cycle pulses

cycle. As a consequence, to achieve an efficient acceleration, matching the phase front of the THz beam with the electron trajectory is essential.

The configuration illustrated in Figure 4.2 is a 2D presentation of the concept devised to solve the above two problems. First, two linearly polarized THz beams are symmetrically coupled into the multilayer structure in order to cancel out the effect of the magnetic field. Second, the phase front of the THz beam is divided into several portions, which are out-coupled from each other using thin metallic surfaces. In each layer, dielectric inclusions are added to delay the arrival time of the pulse to the acceleration region. By properly designing the filling factor of dielectrics and the thickness of each layer, continuous acceleration of electrons from rest throughout the whole phase front can be achieved. The dielectric material in the structure of Figure 4.2 is assumed to be quartz ($\varepsilon_r = 4.41$) due to its low loss characteristics in the THz regime.

Based on the introduced concept of the acceleration using high energy single cycle pulses, we proceed with developing a 3D scheme with real single cycle THz pulse excitations. Focusing of the THz beams in the transverse plane (H-plane), can potentially increase the field at the acceleration point and thereby the acceleration efficiency. Therefore, we attempt to focus the incoming excitations in the transverse plane. Furthermore, the thin metallic films which are suspended in vacuum (Figure 4.2) must be avoided in a real device. The main purpose of considering vacuum and quartz in the structure is to realize a dielectric contrast to delay the different parts of the beam phase front. However, this goal can be achieved with any pair of materials with various refractive indices. Hence, we consider quartz ($\varepsilon_r = 4.41$) and teflon ($\varepsilon_r = 2.13$) for the realistic design.

The structure shown in Figure 4.3 is the ultra-fast THz gun designed for the operation based on two single-cycle THz Gaussian beams with 1.1 mJ energy and central frequency 300 GHz. The beam profile is flat top along the acceleration axis and Gaussian in the transverse plane with 2 mm spot size. The assumption for flat top wave front is motivated mainly by the THz generation process based on high power lasers. The high power lasers usually operate in the saturation regime which leads to a flat top wave front. However, this is not a limiting assumption.

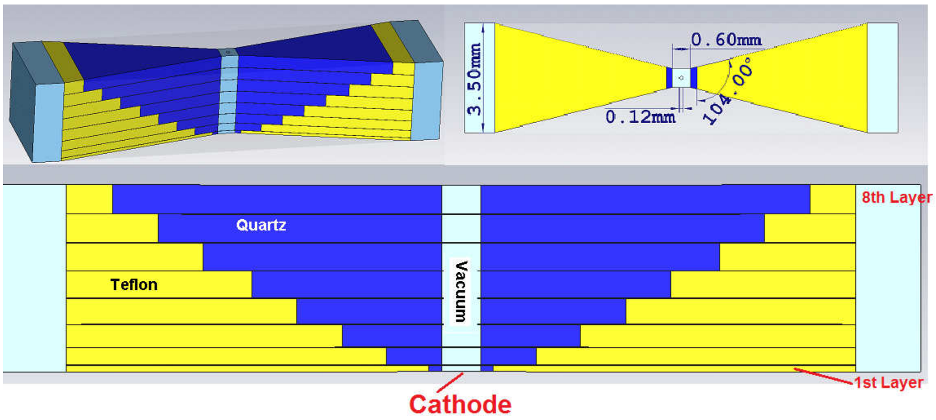

Figure 4.3: Schematic illustration of the ultra-fast electron gun designed for two 1.1 mJ THz beams from the two sides.

Table 4.1: length (L_i) and thickness (Z_i) of the quartz layers, The index i starts counting at the electron source

Parameter	Z_1	Z_2	Z_3	Z_4	Z_5	Z_6	Z_7	Z_8
Value (mm)	0.100	0.270	0.350	0.400	0.420	0.430	0.440	0.450

Parameter	L_1	L_2	L_3	L_4	L_5	L_6	L_7	L_8
Value (mm)	0.200	0.865	1.550	2.250	2.950	3.700	4.400	5.100

For a completely Gaussian beam individual couplers can be designed to couple the beam energy into the gun input. The detailed dimensions of the designed device are shown in Table 4.1.

The propagation of the electromagnetic field in this structure has been simulated by CST microwave Studio. Some snapshots of the electromagnetic field propagation inside the layers are sown in Figure 4.4. It can be seen in this figure that the electromagnetic wave needs different times to travel in each layer. However, the waves from opposite layers arrive simultaneously to the middle of the gun. Since the electric fields of these waves are in the same direction they will be added in spite of the magnetic fields that cancel out because of their opposite directions. Figure 4.5 shows the required time dependency of the electric field at the middle of the eight layers as well as the port signal for 1 W input power. As it is shown in this figure, the electric field in each layer crosses zero from negative values when the electric field in the previous layer crosses zero from positive values. To fulfill such conditions one should select the proper value for the length of the quartz layer to make the desirable delay between the electric field in the adjacent layers.

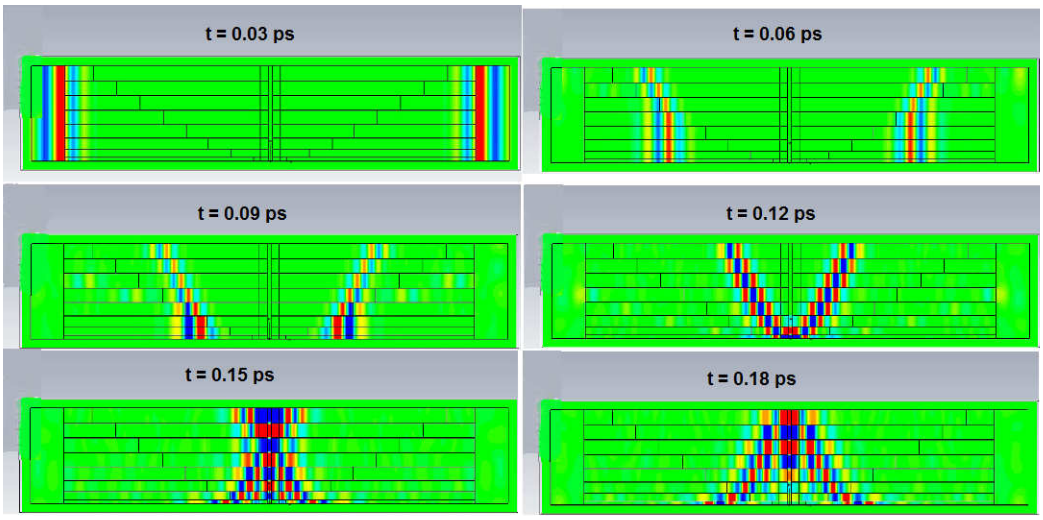

Figure 4.4: snapshots of the wave propagating along the gun in 30 fs intervals

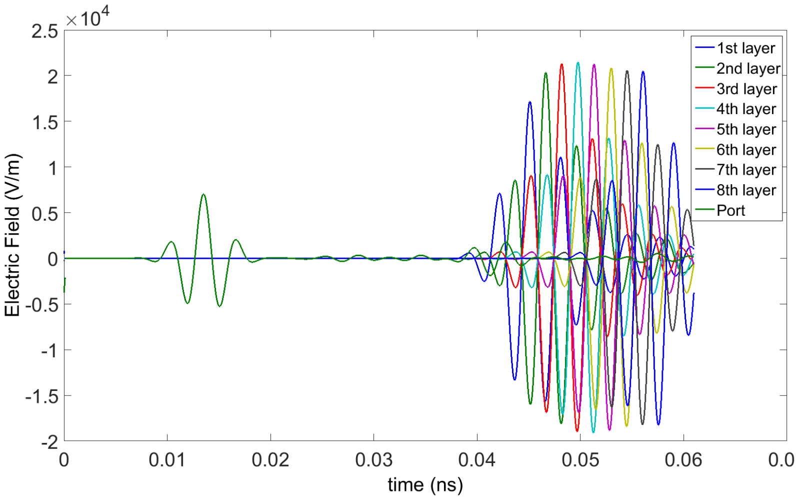

Figure 4.5: The required electric field distribution in the middle of the layers (for 1 W input power)

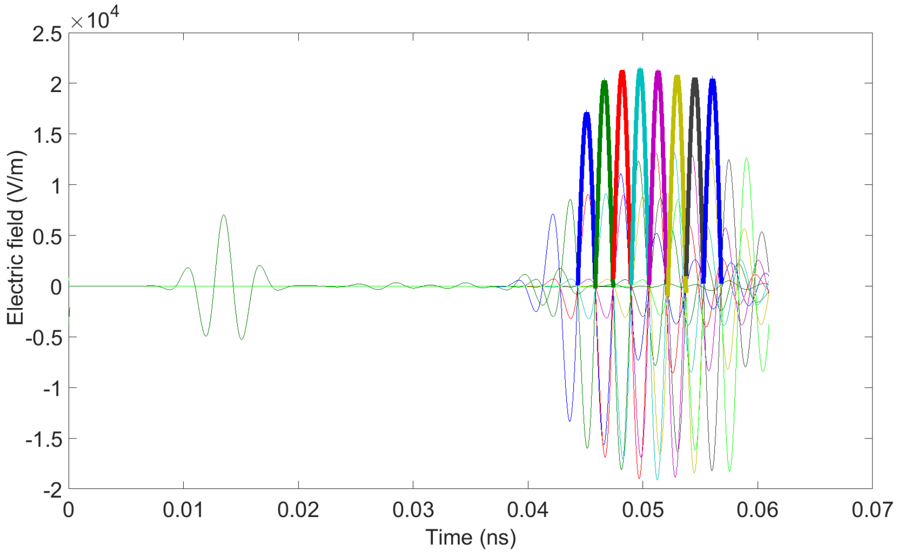

Figure 4.6: The electric field that we expect the electrons see while passing through the gun

As mentioned the thickness of the layers should also be designed so the electrons enter each layer when its electric field crosses zero level and starts to increase and leave the layers before the electric field sign changes. Hence the electric field that we expect that the electrons experience can be shown as in Figure 4.6.

In order to fulfill this condition an iterative method has been employed. From the analytical estimation one can select the initial values for the thickness of the layers. Then a time domain simulation with CST determines the electric field pattern inside the layers. As the next step one has to simulate the electrons acceleration although it is not possible to simulate it directly with CST. For this purpose, the electric field on the axis of the gun is sampled in 2 fs time intervals by CST and then the velocity, energy and position of an electron is calculated using a MATLAB code. From the acceleration results in a iterative way one can select the optimum values for the thickness of the layers. The results of the electron acceleration study for the optimized structure are depicted in Figure 4.7. One can easily distinguish the times in which the electron is in the transitions between two layers from the energy curve. It is also clear that the final energy of the electron would be about 2.1 MeV. It should be noted that from the simulation one can also optimize the time at which the electron should be released from the cathode.

The acceleration of an electron bunch has also been simulated. Since it is not possible to do this study by a standard software such as CST, a home made DGTD (Discontinuous Galerkin Time Domain) solver has been used. By generating a photoemission bunch at the instant with E_z =-200 MV/m and performing PIC cal-

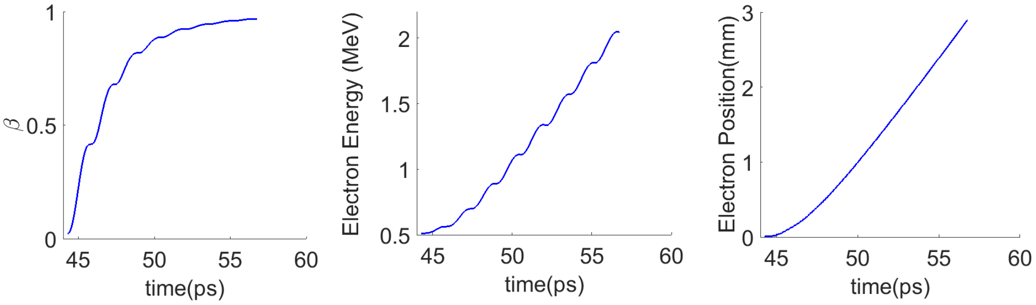

Figure 4.7: The velocity (left) , energy (middle) and position (right) of the electrons while passing from the cathode along the axis of the accelerating structure.

culations with point-to-point space charge, the acceleration of an electron bunch in the proposed gun is simulated. We assume that a 20 fs UV laser pulse generates 1 pC charge over a 60 μm spot size. The bunch is modeled using 20'000 macroparticles. The simulation results are shown in Figure 4.8. The results demonstrate acceleration of 40% of the bunch to 2.1 MeV with 1.5% energy spread. The main reason for the particle loss is the deflection of the electron trajectories out of the considered vertical path and collision with the metallic layers.

4.2.1 Sensitivity analysis of the designed cavity

A sensitivity analysis for the designed guns is very useful when real applications are aimed. The results of such analysis can be used to determine the manufacturing tolerances as well as the precision requirements of the input signal. Generally the most critical parameters of the gun are the thickness and length of the quartz layers which include 16 values. In this analysis, each value has been swept in a reasonable range while the other parameters are kept constant and equal to the design value to find the sensitivity of the gun to the target value for the parameter. After each change we calculated the equation of motion to determine the electrons final energy. Such analysis has also been performed for the input central frequency as well as the injection time of the electrons. The results of the analysis are shown in Figure 4.9, which shows a low sensitivity of the gun performance to the desired dimensions and also the excitation frequency. This can be another advantage of the single cycle gun in comparison with the resonant cavities which are extremely sensitive to their dimensions and the excitation frequency. We know that for instance by changing the diameter of one cell of the cascaded cavities their important parameters such as resonant frequency, distribution of the field inside the cells and also external quality factor will change. These changes can have a huge effect on the operation of the cavity specially the ones considered to perform

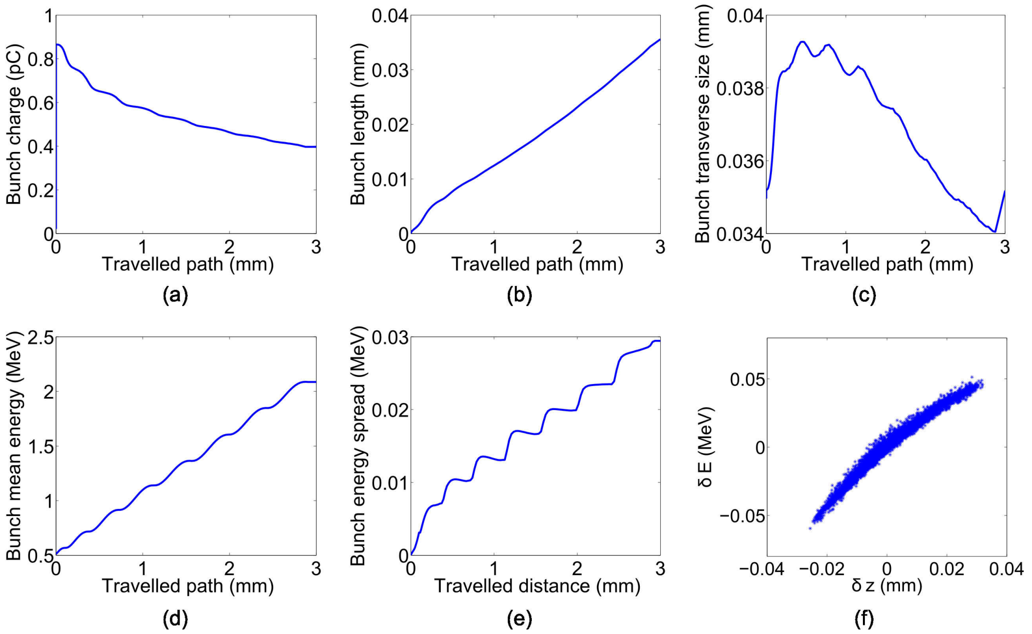

Figure 4.8: Acceleration of about 0.9 pC photoemitted bunch in the high energy THz gun: (a) bunch charge, (b) length (rms), (c) transverse size (rms), (d) mean energy, (e) energy spread (rms) are depicted in terms of the traveled distance. The phase-space of the output bunch is also shown in (f).

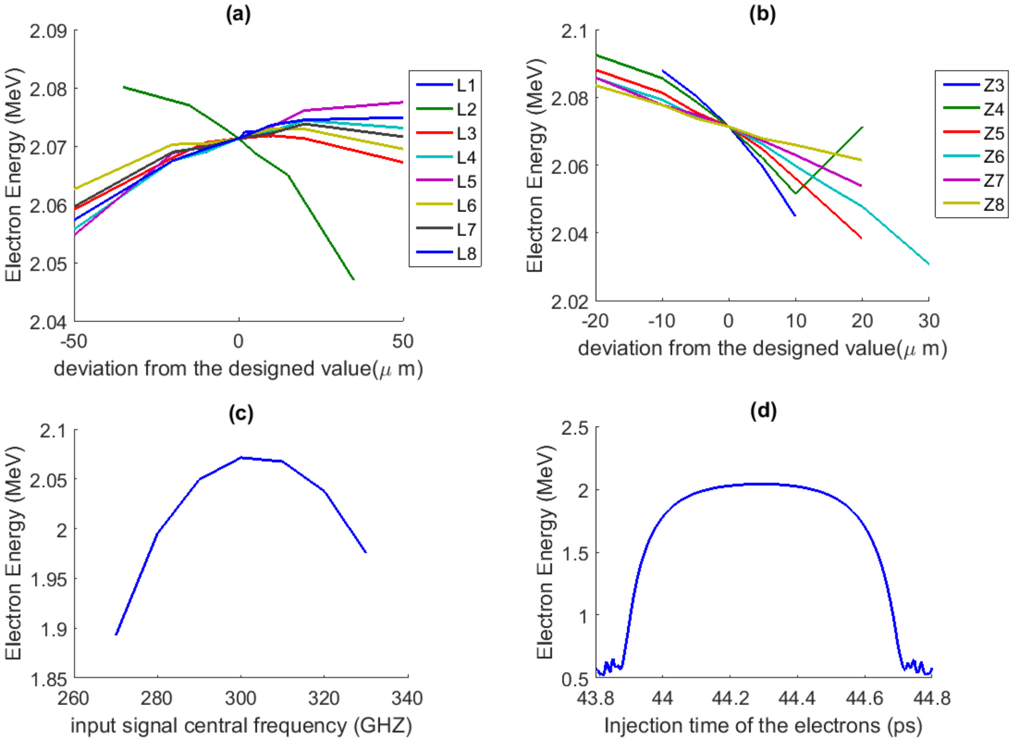

Figure 4.9: sensitivity analysis for (a) thickness of the layers, (b) length of the quartz layers, (c) input central frequency, and (d) electron injection time

as guns.

4.3 100 GHz single cycle gun

As a result of the considered THz generation scheme in the AXSIS project, it may become inevitable to use a single cycle signal with the central frequency of 100 GHz. In this respect, another gun has been designed to be able to accelerate the electrons up to the same energies as in the 300 GHz gun (about 2.1 MeV). Here we make some simple calculations to have an insight into the dimensions of the new gun and generate a scaling algorithm for other possible frequencies.

We assume that the 100 GHz gun uses the total input energy equal to the 300 GHz and accelerates the electrons up to 2.1 MeV like the previous one. We show the total thickness (height), length, and width of the gun by H, L, and W, respectively (Figure 4.10), and these parameters for the gun to be designed by H', L' , and W'. Let us assume that the height of the 100 GHz gun is α times larger

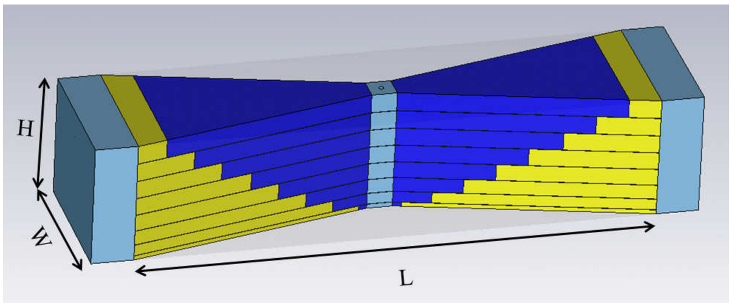

Figure 4.10: definition of the gun dimensions

than the height of the 300 GHz gun: $H' = \alpha \cdot H$. If the peak of the electric field in the middle of the gun is called ξ, one can write the rough energy gain of the electrons as $\Delta E = \xi \cdot H$, so applying the equal energy gain condition yields to:

$$\xi' \cdot H' = \xi \cdot H \Rightarrow \xi' = \frac{1}{\alpha} \cdot \xi \quad . \tag{4.2}$$

To apply the equal input energy one can use the Poynting vector. We know that the power flow from a cross section is equal to the integration of the Poynting vector over the area. Since the amplitude of the Poynting vector is proportional to the square of the electric field and considering that the total duration of the 100 GHz signal is 3 times larger than the 300 GHz signal the equal input energy condition can be written as:

$$\begin{aligned} &\xi'^2 \cdot H' \cdot W' \times 3 = \xi^2 \cdot H \cdot W \\ \Rightarrow &(\frac{1}{\alpha^2} \cdot \xi^2) \cdot (\alpha \cdot H) \cdot W' \times 3 = \xi^2 \cdot H \cdot W \end{aligned}$$

$$\Rightarrow W' = \frac{\alpha}{3} \cdot W \quad . \tag{4.3}$$

As mentioned before we make the gun in a horn shape to focus the input signal and enhance the field at the middle of the gun where it interacts with the electrons. However, making this cross section smaller than the value that leads to a cut-off frequency larger than the operating frequency should be avoided. Hence, the width of the gun is determined by the frequency with a linear relationship and for the 100 GHz gun it would be three times larger than for the 300 GHz design, $W' = 3W$. Applying this result with equation (4.3) leads to $\alpha = 9$ for the ratio of the electric field in the two designs. So the height of the 100 GHz gun would be 9 times larger than the 300 GHz gun. Now, we investigate the effect of the number of the layers. At the first layer, since the electrons are not yet relativistic one can use classical equations of motion according to which the distance that the particle passes in a certain time with a constant acceleration is proportional to its acceleration and square of the time. As a comparison between the two guns and since the electron acceleration a is proportional to the electric field and since the time depends on the frequency one can say $a' = \frac{a}{9}$ and $t' = 3t$. The distance that the electron passes during one cycle is therefore equal in the two cases which means the thickness of the first layers would be similar in the two gun designs. On the other hand, for the above layers the electron is relativistic and travels almost the same distance in each cycle which is equal to the half of the signal wavelength, so the thickness of the above layers is three times larger than the thickness of these layers for 300 GHz gun. Considering the discussed issue and the fact that the total height of the new gun should be 9 times larger than the old one we expect that number of the layers in 100 GHz gun would be more than three times larger than for the 300 GHz gun. The exact number of the layers would be determined by the simulations during the design. The length of the gun is also strongly dependent on the number of the layers. As it is explained in each layer we have teflon and quartz. Since the quartz layers are responsible to make a delay between the arrival time of the signal in each layer, the length of the quartz inclusion should be larger by certain value than the previous layer. This value causes a delay of the duration of the signal. In the 100 GHz gun the duration of the signal is three times larger and on the other hand the number of the layer would increase more than three times which leads to an increase the length of the gun more than 9 times. As a summary one can write the following relation between the dimensions of the two guns:

$$H' > 9H; \quad W' = 3W; \quad L' > 9L; \quad n'_{Layers} > 3n_{Layers} \quad , \tag{4.4}$$

where n_{Layers} is number of the layers. One can easily follow the mentioned method to find the general relation of scaling the size of the gun with respect to the frequency as:

$$H' > (\frac{f}{f'})^2 H; \quad W' = \frac{f}{f'} W; \quad L' > (\frac{f}{f'})^2 L; \quad n'_{Layers} > \frac{f}{f'} n_{Layers} \quad . \tag{4.5}$$

It is worth to mention that if we want to keep the power constant and not the energy it would be sufficient just to scale the dimensions of the gun. That means just by scaling the designed gun for 300 GHz with a scaling factor of 3 it would work with the same power as a single cycle signal leading to 3 times more energy. We can write a general relation equivalent to equation (4.5) for the case of constant power:

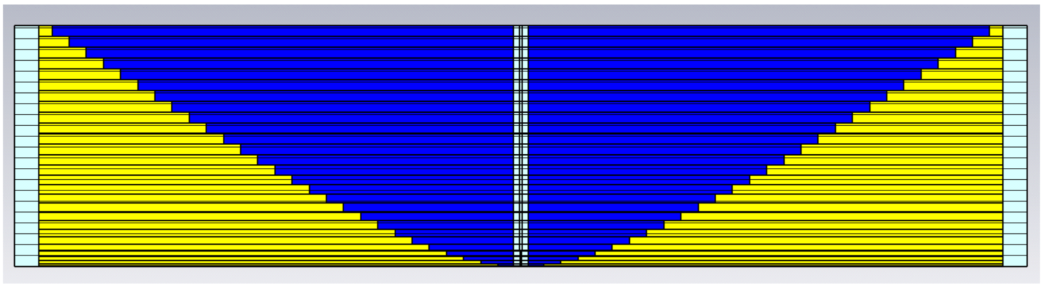

Figure 4.11: Cross sectional view of the 100 GHz gun

$$H' = \frac{f}{f'}H; \quad W' = \frac{f}{f'}W; \quad L' = \frac{f}{f'}L; \quad n'_{Layers} = n_{Layers}$$
$$and \quad E' = \frac{f}{f'}E \quad , \tag{4.6}$$

where E and E' are the required energies.
Since the gun for 100 GHz has a rather large number of layers it is a too time consuming design process and it would be better to design the layers separately. For this purpose, each layer is designed by simulating the layer itself and the layers above and below it. After designing the layers separately, final simulations of the whole structure has been performed to confirm the expected gun operation. The designed gun has 28 layers which corresponds to the aforementioned predictions. The other dimensions of the two guns are summarized in Table 4.2.

Table 4.2: Dimensions of the designed guns for 300 GHz and 100 GHz

	W	**L**	**H**
Value (mm) for 300 GHz gun	3.5	14	2.9
Value (mm) for 100 GHz gun	10.5	130	29.5

A cross sectional view of the designed gun is shown in Figure 4.11. Figure 4.12 also shows the designed gun besides the one for 300 GHz to have a better understanding about the sizes.

Same as for the 300 GHz gun the acceleration of the electrons has been calculated from the electric field sampled on the axis of the gun. The results are shown in Figure 4.13. Again in the energy curve one can distinguish 28 different layers which represent the 28 layers. However it is more difficult to recognize the layers in comparison to the acceleration curve for the 300 GHz gun (Figure 4.7). The final energy of the electrons is about 2.1 MeV i.e. the same as for the 300 GHz gun.

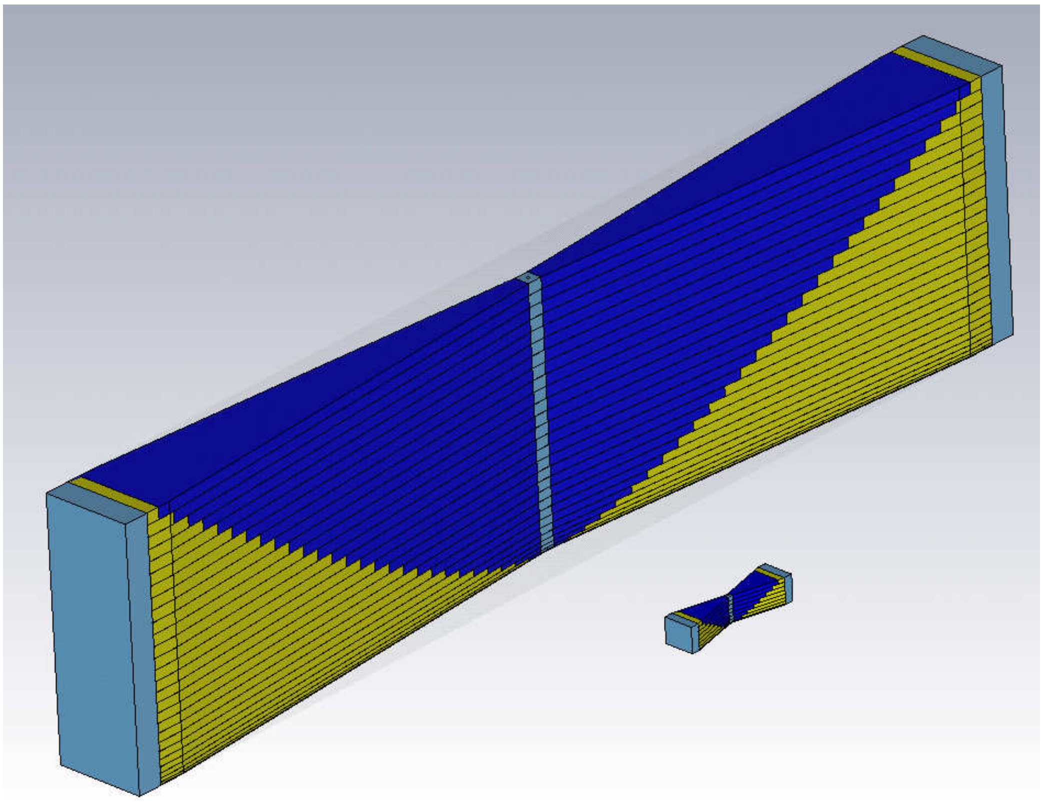

Figure 4.12: Size comparision of the two guns

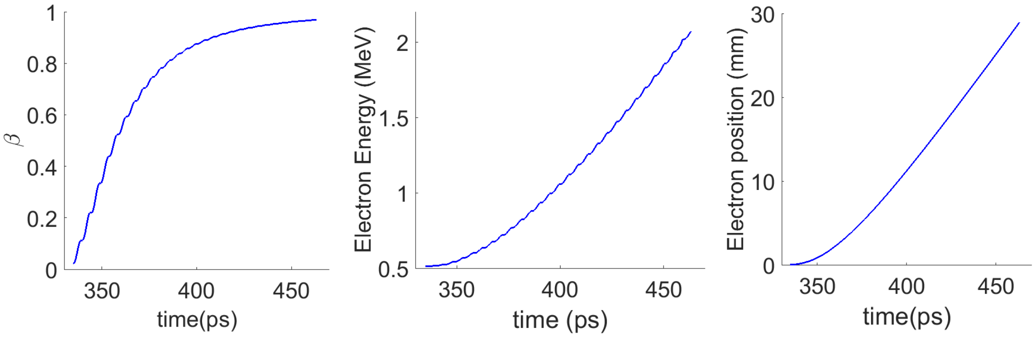

Figure 4.13: Acceleration results for the 100 GHz designed cavity

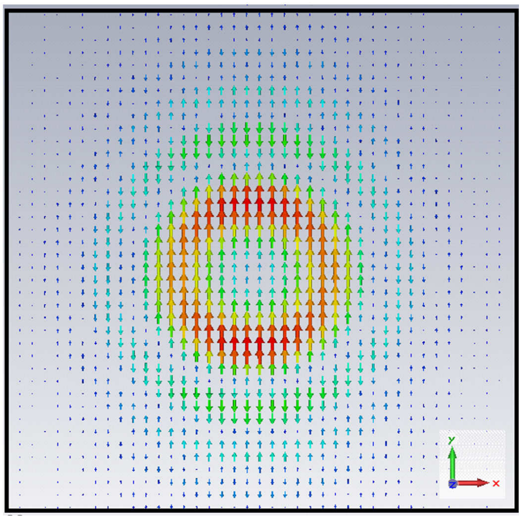

Figure 4.14: The transverse electric field pattern in a Gaussian beam, this beam propagates in z direction

4.4 Coupler design

The THz generator provides a single cycle Gaussian beam which means the spatial distribution of the field as well as it temporal distribution is Gaussian. Such Gaussian beam is shown in Figure 4.14. The electric field of such Gaussian beam should be coupled to a rectangular waveguide in which the electric field in the operating mode (TE_{01}) is shown in Figure 4.15. It is constant in y direction while its x dependence is a sinusoidal function. Therefore, a coupler should be designed to transform the Gaussian distribution of the field to the shape of a waveguide mode and to a flat-top transverse profile. The coupler has to be well designed so the maximum amount of the beam is transferred into the gun.

The idea is to use metallic layers to split the Gaussian beam into eight parts and then inject them into the layers. On the other hand, the shape of the coupler is designed to be a horn. While the Gaussian beam passes the coupler it will be focused because of the properties of the Gaussian beams. The horn taper is designed to focus the beam to the rectangular dimension. Figure 4.16 shows a cross section of the designed coupler with its dimensions. The metallic layers that are used to split the beam are shown in this figure. The focus point of the beam is assumed to be at the end of the coupler which is actually the beginning of the gun. The metallic layers will start in a distance equal to the Rayleigh length of the beam from the gun. At the end of the gun, this layer will be connected to the metallic layers of the gun, so the space between them is the same as the thicknesses of the layers. But in the beginning of the coupler one has to design the distances

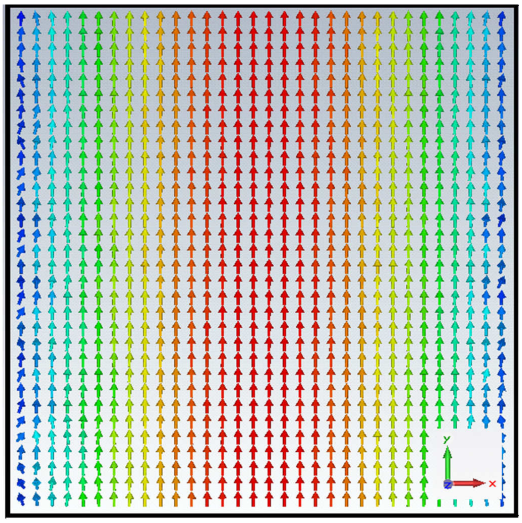

Figure 4.15: The transverse electric field pattern of TE_{01} mode in a rectangular waveguide, this wave propagates in z direction

between the layers in a manner that the Gaussian beam is split in correct slices. Since the amplitudes of the electric field in the gun layers have to be equal, the ratios of the power of the signal inside the layers are proportional to the thickness of the layers and one can easily calculate the distances of the metallic layers of the gun by considering the integration of the Gaussian beam. Such idea is depicted in Figure 4.17. It should be noted that these layers are perpendicular to the electric field and will not disturb the Gaussian beam.

Simulations show that 95% of the power of the Gaussian beam will couple to the gun using this coupler. Figure 4.18 shows some snapshots of the electric field distribution inside the coupler. The overall schematic of the gun with its coupler is displayed in Figure 4.19. The acceleration simulation was carried out for the overall structure whose results are shown in Figure 4.20. It can be seen that with the same energy of 2mJ the electrons are accelerated up to 2 MeV.

4.5 Investigation of using cavities as Gun for AXSIS

After introducing the ultra-fast guns, it is worth to investigate the possibility of using conventional cavities to accelerate the electrons. Based on our THz generator limitations the maximum number of the THz pulses that can be provided to fill the cavity is 50. It is therefore necessary to design a cavity with a quality factor of about 50 that can reach a steady state mode within 50 pulses. To achieve this goal, one should decrease both unloaded and loaded quality factor that means increas-

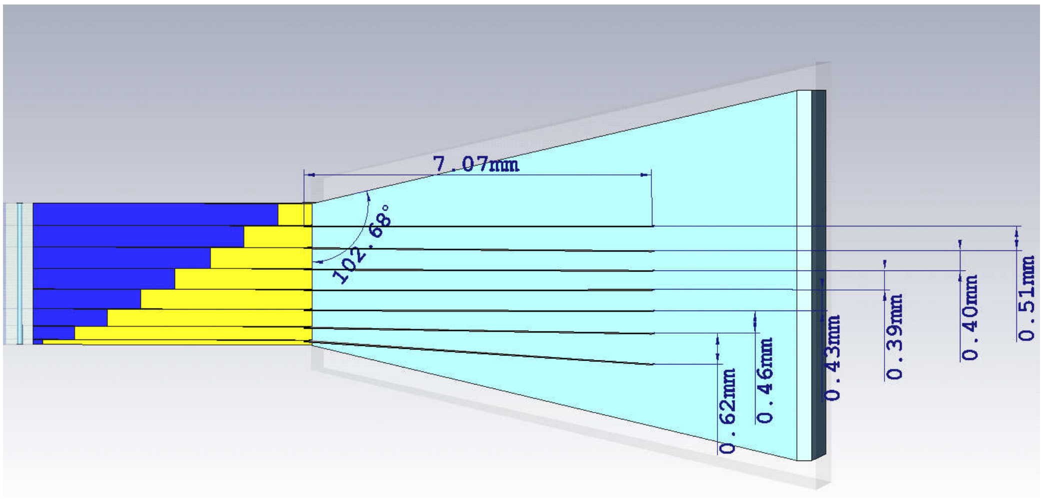

Figure 4.16: Cross sectional view of the Gaussian beam coupler

ing the power dissipation in the cavity walls as well as increasing the reflected power from the cavity to its coupler. The first cavity that has been designed based on the discussed issues is shown in Figure 4.21. It is a four cell normal conducting cavity with a resonant frequency of 100 GHz for the π - mode. As it can be seen, the THz signal is emitted from both sides through silicon wafers. By changing the doping level of these wafers one can adjust the quality factor of the cavity.

In order to find out if the designed cavity can operate as a gun, the time domain simulation has been performed by CST microwave studio. The electric field on the axis of the cavity in the middle of the cells is shown in Figure 4.22.

There are some points in this figure that should be considered. First, one sees that it takes much more time for the two middle cells to be filled with the electromagnetic field rather than the first and last cell. The reason is that the field is emitted from the first and last cells after firstly filling these cells. Afterwards, the fields will be coupled from these cells to their neighbors. The other issue is that even after reaching the steady state for all the cells the envelope of the electric field is not flat that means there is a fluctuation in the amplitude of the field inside the cavity. The reason of these fluctuations is the same as the phenomenon that we discussed in chapter 2 for the REGAE buncher. Here, again the adjacent mode is excited in addition to the operating mode. This problem is even more severe here because of the high bandwidth of the modes as a result of their low quality factor. In fact, the mode separation in the designed cavity is smaller than the bandwidth of the modes which leads to an overlap of the resonant curves for the π - mode and $2\pi/3$ - mode. So the electric field inside the cavity would be a superposition of these two modes. Another consequence of this phenomenon is that the phase

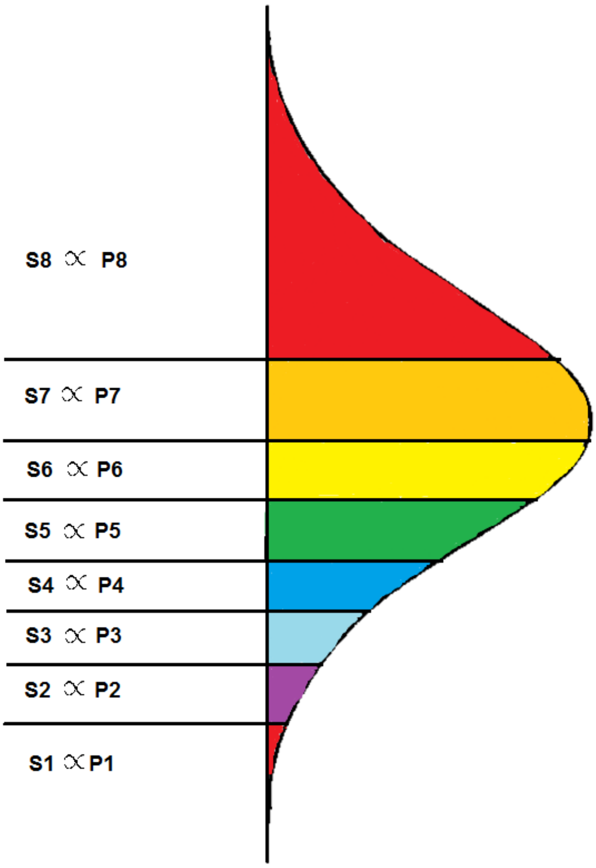

Figure 4.17: Schematic explanation of the idea of designing the coupler, the eight areas (Si) are proportional to the power (Pi) in the eight layers

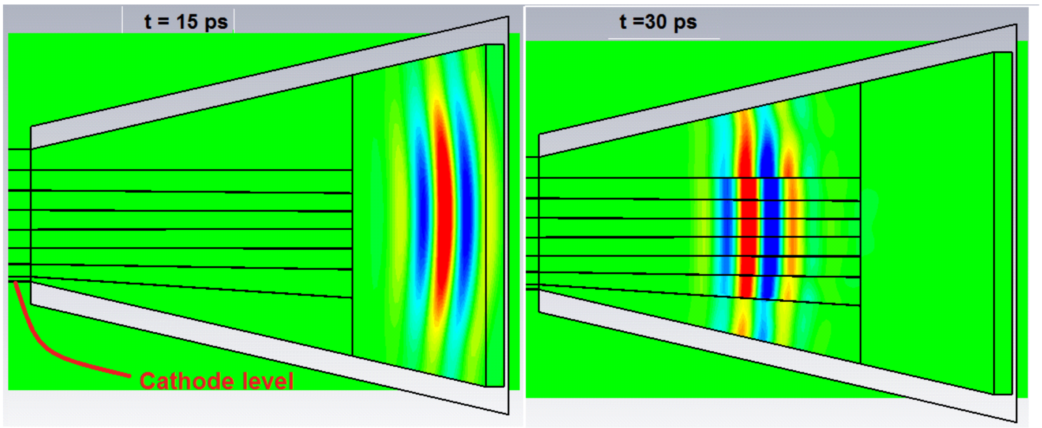

Figure 4.18: Side view snapshots of field inside the coupler

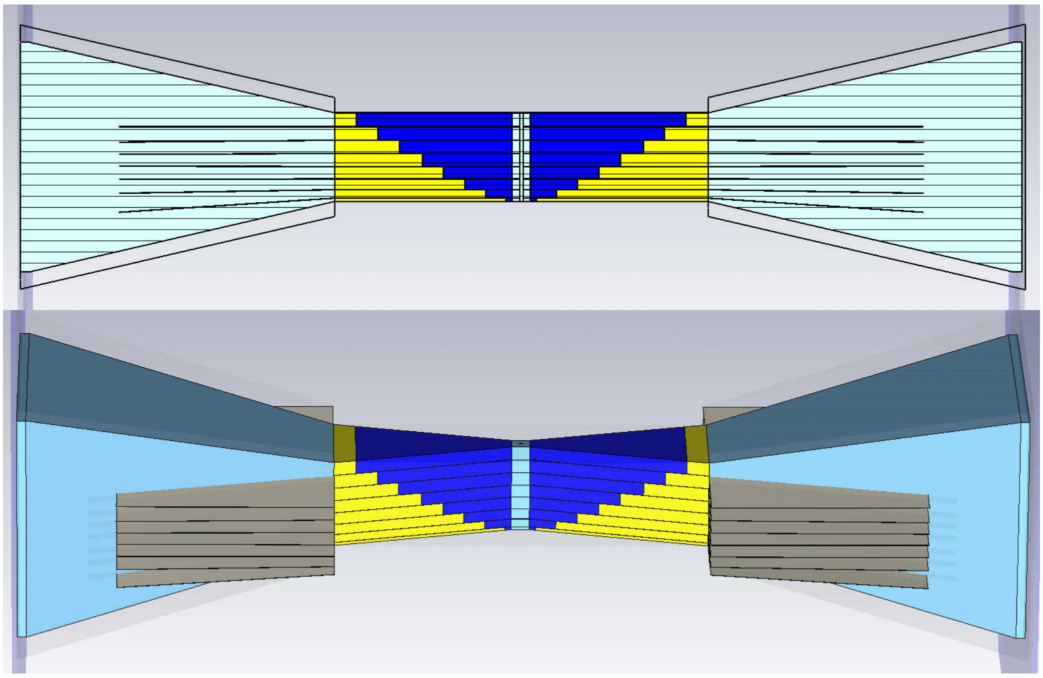

Figure 4.19: cross sectional and isometric view of the gun with its coupler

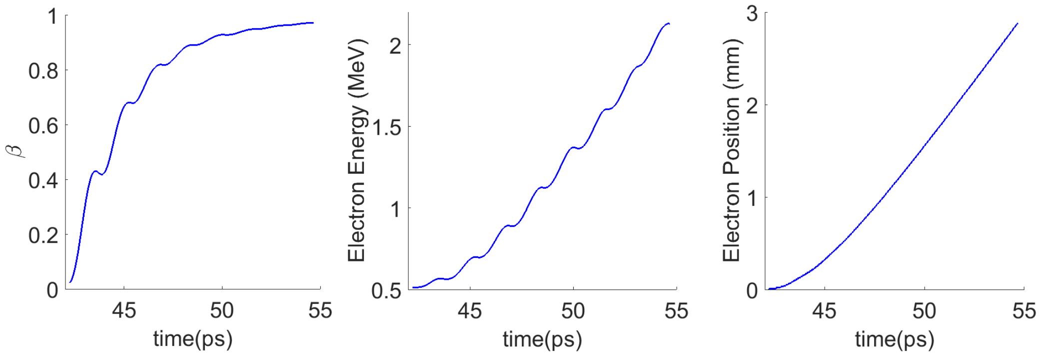

Figure 4.20: Acceleration calculation results for the compelete structure

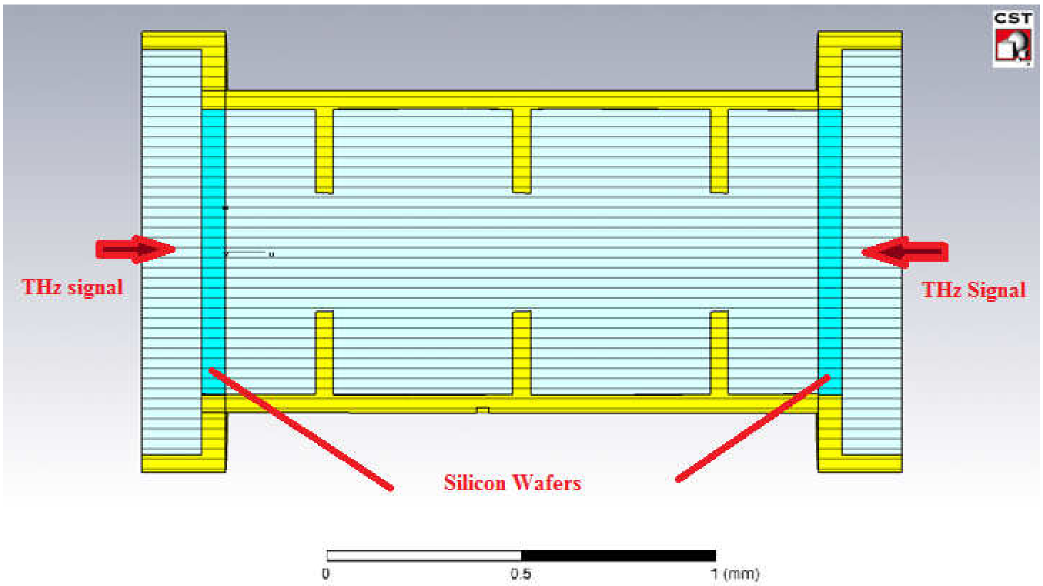

Figure 4.21: The designed four-cell normal conducting cavity

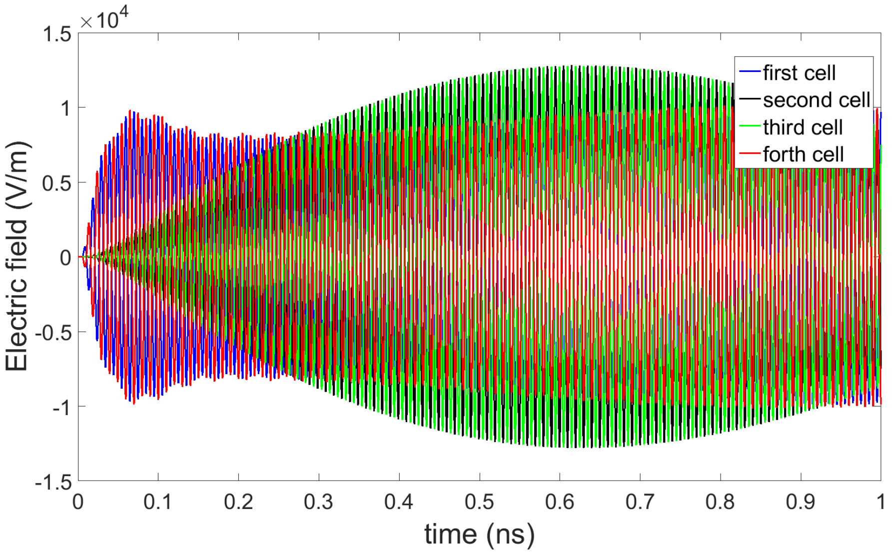

Figure 4.22: The filling process of the designed four cell cavity

difference from one cell to the next cell varies with time and is not always 180°. This effect is shown in Figure 4.23.

Some of the mentioned problems can be solved if we use a two-cell cavity. If the THz signal enters the coupled cavities from both sides the cells will be filled simultaneously within a small number of pulses. Furthermore for a two cell cavity there will be only two TM_{010} modes (0-mode and π -mode) with mode separation frequency larger than the difference between the π -mode and $2\pi/3$-mode in a four cell cavity. The phase difference between the cells in this case is also a superposition of zero and π which is always π. The cross sectional view of the designed cavity as well as the time domain simulation results are displayed in Figures 4.24 and 4.25. It can be seen from this figure that it is possible to fill this cavity within about 10 cycles. Hence, it seems to be more appropriate for the AXSIS project than the four cell cavity. The important parameter of the designed cavities is the amount of energy required for the electron acceleration. In order to simplify the comparison between the cavities and the multilayer guns we calculated the required energy to accelerate the electrons up to 2 MeV, the same energy that we can reach by the multilayer guns. From the CST time domain solver one can find the electric field amplitude for a given input power. The results shown in Figures 4.22 and 4.25 are obtained by 1 W input power assumption. From these results, by scaling the electric field that is roughly needed to accelerate the electrons one can find an approximate estimation for the required energy which would be 110 mJ and 320 mJ for the two cell and four cell cavities, respectively. These values of the required energy is much more than that we need for the multilayer guns (2

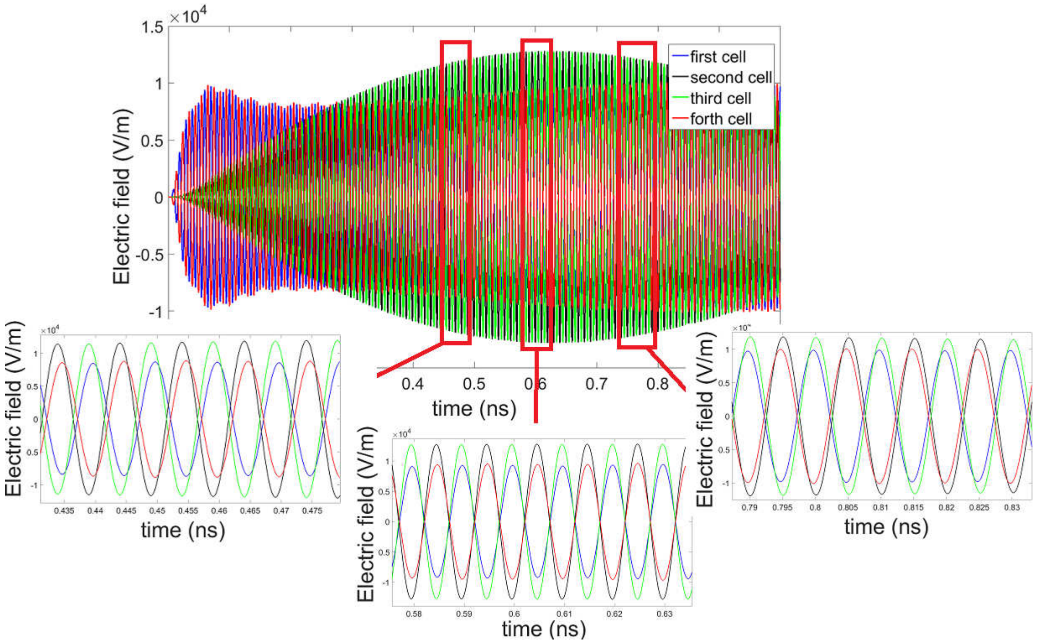

Figure 4.23: Cell to cell phase difference changes by time

mJ).

One may wonder "what is the reason for the big difference between the required energy in these two mechanisms?" To find the answer to this question one can calculate the required energy from another method. By running the Eigenmode solver of CST, one can find the electric field distribution inside the cavity. It is even possible to calculate the field distribution of a pillbox cavity in TM_{010} mode [36, 32]. In CST Eigenmode solver the amount of the stored energy is always assumed to be 1 Joule. The electric field on the axis of the two cell cavity is shown in Figure 4.26. For accelerating the electrons up to 2 MeV, we need a 5 times smaller electric field that means a 25 smaller stored energy (40 mJ). On the other hand, from the definition of the quality factor one can easily find the required power:

$$Q = \frac{\omega U}{P} \Rightarrow P = \frac{\omega U}{Q} \quad , \tag{4.7}$$

where U , the stored energy would be 40 mJ here and the angular frequency ω of $2\pi \times 10^{11}$ rad/s. By substituting these values in the above equation, we need about 10^9 W power that leads to 0.1 J energy by considering the time of 10 cycles. This calculation verifies the results from the time domain solver. Additionally, one can find the reason of high energy need. From the equation 4.7, one sees that the amount of the required power is reversely proportional to the cavity quality factor.

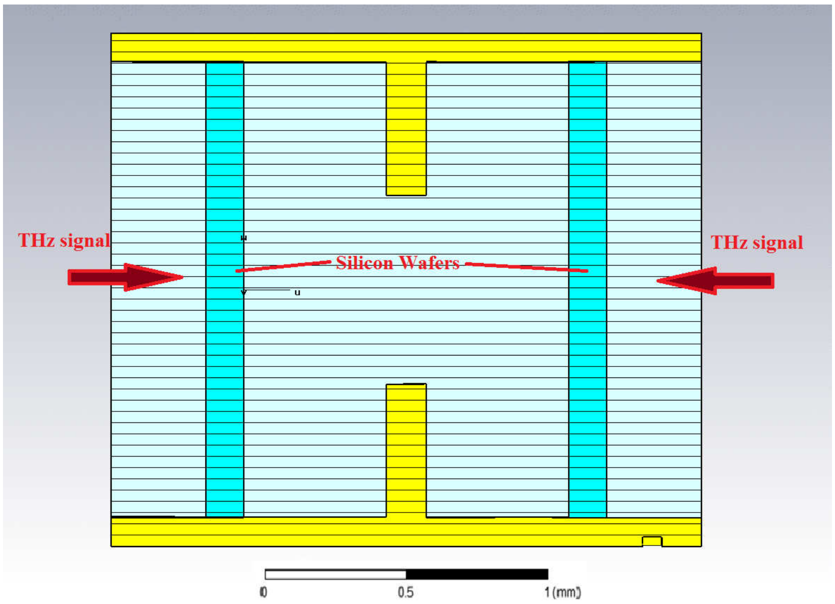

Figure 4.24: The two cell designed gun

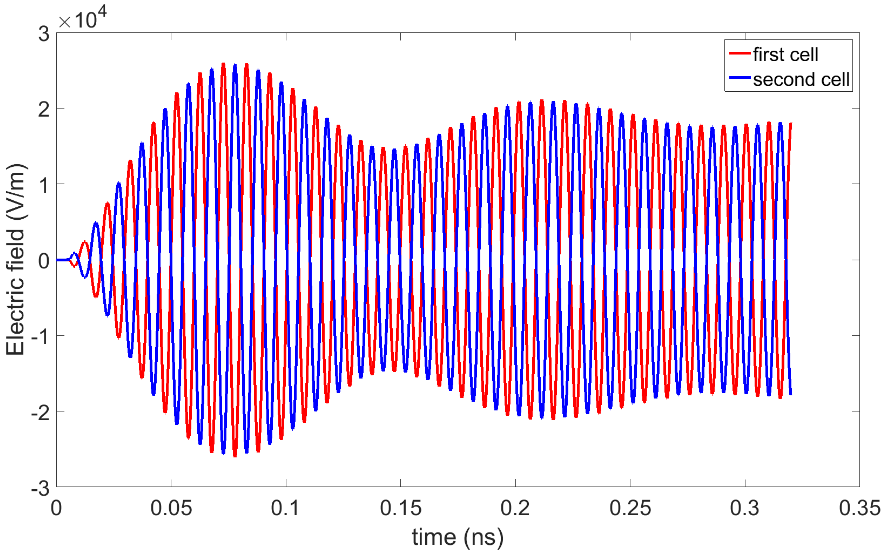

Figure 4.25: Filling process of the designed two cell cavity

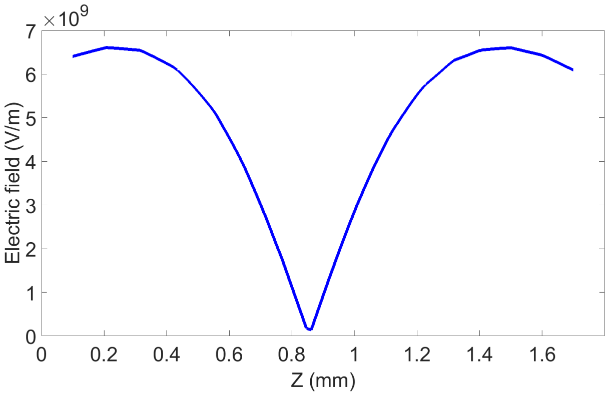

Figure 4.26: The electric field inside the cells on the axis of the two-cell cavity as calculated with the CST Eigenmode solver

The smaller quality factor, the larger the required power. In fact, one can conclude that filling a cavity by a few cycles and using it to accelerate the electrons would not be a good idea since due to the low quality factor of the cavity a lot of power is required. In such a case, a better method is to add the power of the cycles to make a single cycle pulse and accelerate the electrons by this one cycle. This is actually the same method that we used in ultra-fast guns that have been introduced in the first part of this chapter. It should be noted however, that using the cavities as gun has some advantages in comparison with the introduced multilayer structures. Because of their symmetric structure cavities can provide higher quality beams with probably more charge. Besides they would be more stable than a single cycle structure. In fact there is a trade-off between the required energy and the beam quality and its stability. Some recent progresses show that it may be possible to have about 300 THz cycles. With this number of the THz cycles it may be possible to benefit from the resonance properties of the cavities to accelerate the electrons consuming less energy. However, it would be necessary to study some other aspects of these cavities such as thermal issues, metallic breakdown and multipacting.

4.6 Summary and conclusion

The attempt to achieve high acceleration gradients for developing compact accelerators is strongly hampered by the breakdown threshold of the materials used in the accelerating devices. The pre-existing scaling laws together with the recent findings confirm the strong relaxation of break down limits with the reduction of pulse duration. On the other hand, the remarkable progress in ultra-fast technologies has enabled the generation of very short pulses from the optical to the RF regime. Therefore, the development of broadband devices for the efficient acceleration of particles using ultra-short pulses is an important contribution towards the realization of compact accelerators. Novel structures to accelerate the electrons from their rest energy to relativistic velocity have been introduced in this chapter. We use a multilayer ultra-fast gun which works with a single cycle THz signal. The simulations show that it is possible to accelerate the electrons up to 2.1 MeV using the proposed structure fed by 2 mJ input energy. Two different guns are designed to operate at 100 GHz and 300 GHz central frequencies. A mechanism to couple the Gaussian beam to these guns has also been introduced. It transmits 95 % of the input signal to the gun. It is also investigated if it makes sense to use normal conducting cavities to accelerate the electrons. The simulations show that if we want to use a few THz cycles, we would need at least 100 mJ energy to achieve the same acceleration as for the multilayer structures that means 50 times more energy as a result of the low quality factor of the cavities. However it is worth to study cavities that can be filled with 300 cycles, the number of THz cycles that seems to be feasible to be provided. Using such cavities, one may be able to generate higher quality and more stable bunches. Thermal issues, metallic breakdown and multipacting are some of the problems that have to be investigated for the cavities.

Chapter 5

Summary and Outlook

RF cavities in advanced accelerators are not only responsible for increasing the particle energy, but they are also widely used to improve the beam quality and additionally for beam diagnostics. In the first two parts of this work we described such applications. First a new buncher cavity has been designed for the REGAE facility. In the existing buncher cavity at REGAE the difference between the π-mode which is the operating mode and other TM_{010} normal modes (specially $2\pi/3$-mode) is small in terms of resonant frequency which causes some unwanted effects on the machine operation. The main goal of the new design was therefore improving the mode separation. Physical parameters of the cavity such as thickness of the disks between the cavity cells, iris radii and diameter of the cells have been adjusted to achieve this goal. In the newly designed cavity the differences between the π-mode and the $2\pi/3$-mode, $\pi/3$-mode and 0-mode have been increased from 2, 7 and 12 MHz in the existing cavity to 9.5, 35 and 59 MHz.
The design of a normal conducting cavity to stabilize the arrival time of the electrons at FLASH is discussed in the second part. In order to correct an arrival time jitter of ± 150 fs, the designed cavity has to be able to provide an accelerating voltage of 37.5 kV and the half bandwidth between 400 and 500 kHz. A mode separation of 9 MHz between the operating mode and its adjacent mode was also needed. A solid-state amplifier provides the input power of the cavity which will be injected via a loop coupling mechanism that has been designed. Using loop coupling makes it also possible to adjust the bandwidth of the cavity even after manufacturing and installing it. The simulation results show that the designed cavity fulfills all the required conditions. Furthermore, wakefield, thermal and multipacting simulations have been performed to evaluate the operation efficiency of the designed cavity which show stable operation without negative effects of the longitudinal and transverse wakefields, thermal expansions and multipacting phenomenon. Both cavities described in chapter 2 and 3 are modeled with electric

circuits. Dealing with electric circuits is easier rather than the Maxwell's equation that makes it easy to understand the mechanism of the operation of the cavities. The input coupling mechanism as well as the cell to cell coupling have been modeled by electric circuits. Based on the proposed model a novel algorithm is also introduced to be used to find the optimum operation of the cavity that provides a guideline for the tuning process. After manufacturing the cavity, the next step would be preparing it to the laboratory tests to measure its resonant frequency, quality factor and tuning it in the room temperature. Then one should clean it carefully to make it ready to be installed in the FLASH main line.

To achieve higher energies of the particles in the accelerators, one solution is to decrease the wavelength of the electromagnetic field by increasing the operating frequency. However, the electrical breakdown of metals put an upper limit to the accelerating gradient which can be provided by the metal cavities. It is therefore of high importance to engage novel accelerating methods and structures that need less size and expenses which can accelerate the particles in higher frequency fields. In the fourth chapter a novel structure to transfer the energy from a THz signal to the electrons is introduced. This structure is going to be used as an ultra-fast gun in the AXSIS project(Attosecond X-ray Science: Imaging and Spectroscopy). We use a multilayer ultra-fast gun which works with a single cycle THz signal. The simulations show that it is possible to accelerate the electrons up to 2.1 MeV using the proposed structure fed by 2 mJ input energy. Two different guns are designed to operate at 100 GHz and 300 GHz central frequencies. A mechanism to couple the Gaussian beam to these guns has also been introduced which transmits 95 % of the input signal to the gun. The possibility of using the metallic cavities to inject the electrons in this frequency range has been also investigated briefly. The simulations show that if we want to use a few THz cycles, we would need at least 100 mJ energy to achieve the same acceleration as for the multilayer structures that means 50 times more energy as a result of the low quality factor of the cavities. However it is worth to study cavities that can be filled with 300 cycles. This number of THz cycles seems to be feasible to be provided based on the new technologies. Using such cavities, one may be able to generate higher quality and more stable bunches. Thermal issues, metallic breakdown and multipacting are some of the subjects that have to be investigated for the cavities.

References

[1] Thomas Wangler. *RF linear Accelerator*. John Wiley & Sons, 1998.

[2] Edmund Wilson. *An introduction to particle accelerators*. Oxford, 2001.

[3] David Griffiths. *Introduction to elementary particles*. Wiley-VCH, 2008.

[4] Povh, Rith, Scholz, and Zetsche. *Particles and nuclei, an introduction to the physical concepts*. Springer, 2008.

[5] Conseil Européen pour la Recherche Nucléaire. CERN, LHC, 2015. http://home.cern/topics/large-hadron-collider.

[6] Brookhaven national laboratory. RHIC, 2015. https://www.bnl.gov/rhic/default.asp.

[7] Deutsches Elektronen-Synchrotron. DESY, PETRA III, 2015. http://photon-science.desy.de/facilities/petraiii/facility information/index eng.html.

[8] Deutsches Elektronen-Synchrotron. DESY, HERA, 2015. http://www.desy.de/research/facilities projects/hera/index eng.html.

[9] Deutsches Elektronen-Synchrotron. DESY, DORIS, 2015. http://doris.desy.de/history/index eng.html.

[10] Schmueser, Dohlus, and Rossbach. *Ultraviolet and soft X-ray Free Electron Lasers*. Springer, 2008.

[11] Saldin, Schneidmiller, and Yurkov. *The physics of free electron lasers*. Springer, 2000.

[12] Deutsches Elektronen-Synchrotron. DESY, FLASH, 2015. http://flash.desy.de/accelerator/.

[13] Deutsches Elektronen-Synchrotron. DESY, XFEL, 2015. http://xfel.desy.de/.

[14] Robert W Hamm. *Industrial Accelerators and Their Applications*. World scientific, 2012.

[15] O. Jaekel. State of the art in hadron therapy. In *A/P conference vol. 985*, 2007.

[16] SJ. Mason, WH. Bostick, W. Roth, and LC. Maier Jr. Modern electronic techniques applied to physics and engineering. *Research Laboratory of Electronics (RLE) at the Massachusetts Institute of Technology (MIT)*, 1946.

[17] T. Weiland. Computer modelling of two- and three-dimensional cavities. *IEEE Transactions on Nuclear Science*, NS-32(5):2738–2742, 1985.

[18] Frank L. Krawczyk. Advanced electromagnetic design of cavities for high current accelerators. *Particle Accelerator Conference*, 4:2361–2363, 1995.

[19] Vivek Sharma. Rf cavity and rfq design and simulation. In *Physics Division Argonne National Laboratory*, 2006.

[20] D. Proch. The tesla cavity: design considerations and rf properties. *Proceedings of the Sixth Workshop on RF Superconductivity, CEBAF*, Virginia, 1994.

[21] G. Burt. Transverse deflecting cavities. *CERN Yellow Report*, CERN-2011-007:395–405, 2012.

[22] S. Ahmed, G. A. Krafft, K. Deitrick, S. U. De Silva, J. R. Delayen, M. Spata, M. Tiefenback, A. Hofler, , and K. Beard. Beam dynamics studies for transverse electromagnetic mode-type rf deflectors. *Phys. Rev. ST Accel. Beams*, 15, 2012.

[23] V. Veshcherevich and S. Belomestnykh. Buncher cavity for ERL. *Particle Accelerator Conference*, 2:1198–1200, 2003.

[24] S. Döbert. Gradient limitations for high-frequency accelerators. *SLAC-PUB-10690*, 2004.

[25] R. Joel England et al. Dielectric laser accelerators. *Rev. Mod. Phys.*, 86(1337):1198–1200, 2014.

[26] Deutsches Elektronen-Synchrotron. DESY, REGAE Homepage, 2010. http://regae.desy.de/.

[27] Deutsches Elektronen-Synchrotron. REGAE-Wiki, October 2013. https://regae-wiki.desy.de/index.php/Main_Page.

[28] Maurizio Vretenar. Linear accelerators. In *CERN International Accelerator Physics Course*, 2011.

[29] Frank Mayet. Simulation and characterization of the rf system and global stability analysis at the regae linear electron accelerator. Master's thesis, Hamburg University, October 2012.

[30] CST. *Microwave Studio*. Computer Simulation Technology AG, 2014.

[31] Lloyd M. Young James H. Billen. *Poisson Superfish*. Los Alamos National Laboratory, January 2006.

[32] Robert E. Collin. *Foundations for microwave engineering*. Wiley, 2nd Edition, 2001.

[33] A. W. Chao, K. H. Mess, M. Tigner, and F. Zimmermann. *Handbook of Accelerator Physics and Engineerin*. World scientific, 2013.

[34] K. Dunkel, B. Griep, C. Piel, H. Vogel, and P. vom Stein. Series fabrication technologies for normalconducting linac and storage ring cavities. *Proceedings of EPAC 2004*, pages 968–969.

[35] K. Dunkel, C. Piel, H. Vogel, and P. vom Stein. Production of s-band accelerating structures. *Proceedings of LINAC 2004*, pages 666–668.

[36] David M. Pozar. *Microwave Engineering*. John Wiley & Sons, Fourth Edition, 2012.

[37] MATLAB. *version 8.0.0.783 (R2012b)*. The MathWorks Inc., Natick, Massachusetts, United States, 2012.

[38] Klaus Floettmann. *ASTRA: A Space Charge Tracking Algorithm*. DESY, ASTRA user manual, October 2011.

[39] R. Brinkmann. The european xfel sc linac project. *Proceedings of LINAC08*, 2008.

[40] P. Emma et al. First lasing and operation of an ångstrom-wavelength free-electron laser. *Nature photonics*, 4:641–647, 2010.

[41] F. Loehl et al. Measurement and stabilization of the bunch arrival time at flash. *Proceedings of EPAC08*, 2008.

[42] S. Pfeiffer, C. Schmidt, M. K. Bock, H. Schlarb, W. Jalmuzna, G. Lichtenberg, and H. Werner. Fast feedback strategies for longitudinal beam stabilization. In *IPAC 2012*, 2012.

[43] SF. Gerigk. Cavity types. In *CERN Accelerator School CAS 2010: RF for accelerators*, 2011.

[44] H. Zhang, B.-Q. Zeng, L. Ao, and Z. Zhang. A novel dual-loop coupler for one-port cylindrical cavity permittivity measurement. *Progress In Electromagnetics Research, PIER*, 127:537–552, 2012.

[45] D. Alesini. Power coupling. In *CERN Accelerator School CAS 2010: RF for accelerators*, 2011.

[46] Alexander Wu Chao. *Physics of Collective Beam Instabilities in High Energy Accelerators*. Wiley, 1993.

[47] T. Weiland and R. Wanzenberg. Wakefields and impedances. *Joint US-CERN particle accelerator school*, 1992.

[48] R. Wanzenberg. Monopole, dipole and quadrupole passbands of the tesla 9-cell cavity. *DESY-TESLA-2001-33*, 2001.

[49] CST. *Particle Studio*. Computer Simulation Technology AG, 2014.

[50] C. Adolphsen, T. Lavine, C. Nantista, R. Ruth, J. WAng, and D. Yeremian. Beam loading compensation in the nlcta. *Particle Accelerator Conference*, 2, 1997.

[51] S. Liu, M. Fukuda, S. Araki, N. Terunuma, J. Urakawa, K. Hirano, and N. Sasao. Beam loading compensation for acceleration of multi-bunch electron beam train. *Nuclear Instruments and Methods in Physics Research Section A: Accelerators, Spectrometers, Detectors and Associated Equipment*, 584(1), 2008.

[52] F. Zhou. Wakefield induced correlated energy spread and emittance growth at ttf fel. *DESY, TESLA FEL-Report 1999-05.*

[53] CST. *MPhysics Studio*. Computer Simulation Technology AG, 2014.

[54] Albert J. Hatch and H. Bartel Williams. Multipacting modes of high-frequency gaseous breakdown. *Physical Review*, 12(681), 1958.

[55] Charles A. Desoer and Ernest S. Kuh. *Basic circuit theory*. McGraw-Hill, 17th edition, 2009.

[56] Maier Slater. Field strength measurements in resonant cavities. *Journal of Applied Physics*, 23(1):68–77, 1952.

[57] Lloyd N Trefethen. *Numerical Linear Algebra.* SIAM (Philadelphia, PA), 1997.

[58] Helmholtz Association. http://www.helmholtz.de/en/. In *AXSIS*, 2015.

[59] G. A. Loew and J Wang. Rf breakdown studies in room temperature electron linac structures. *Joint US-CERN particle accelerator school*, 1988.

[60] G. A. Loew and J Wang. Measurements of ultimate accelerating gradients in the slac disk-loaded structure. *Stanford Linear Accelerator Center*, 1985.

[61] E. Esarey, C. Schroeder, and W. Leemans. Physics of laser-driven plasma-based electron accelerators. *Reviews of Modern Physics*, 81(1229), 2009.

[62] L.J. Wong, A. Fallahi, and F. X. Kaertner. Compact electron acceleration and bunch compression in thz waveguides. *Optics express*, 21:9792–9806, 2013.

[63] W. Kilpatrick. Criterion for vacuum sparking designed to include both rf and dc. *Review of Scientific Instruments*, 28:824–826, 1957.

[64] L. Laurent et al. Experimental study of rf pulsed heating. *Physical review special topics-accelerators and beams*, 14(041001), 2011.

[65] V. Dolgashev, S. Tantawi, Y. Higashi, and B. Spataro. Geometric dependence of radio-frequency breakdown in normal conducting accelerating structures. *Applied Physics Letters*, 97(171501), 2010.

[66] J.A. Fueloep, L. Palfalvi, M. C. Hoffmann, and J. Hebling. Towards generation of mj-level ultrashort thz pulses by optical rectification. *Optics express*, 19:15090–15097, 2011.

[67] S. W. Huang et al. High conversion efficiency, high energy terahertz pulses by optical rectification in cryogenically cooled lithium niobate. *Optics letters*, 38:796–798, 2013.